REPORT DOCUMENTATION PAGE

Form Approved
OMB No. 0704-0188

Public reporting burden for this collection of information is estimated to average 1 hour per response, including the time for reviewing instructions, searching data sources, gathering and maintaining the data needed, and completing and reviewing the collection of information. Send comments regarding this burden estimate or any other aspect of this collection of information, including suggestions for reducing this burden to Washington Headquarters Service, Directorate for Information Operations and Reports, 1215 Jefferson Davis Highway, Suite 1204, Arlington, VA 22202-4302, and to the Office of Management and Budget, Paperwork Reduction Project (0704-0188) Washington, DC 20503.
PLEASE DO NOT RETURN YOUR FORM TO THE ABOVE ADDRESS.

1. REPORT DATE (DD-MM-YYYY)	2. REPORT TYPE Final Technical Report	3. DATES COVERED (From – To) 1 April 2003 – 30 September 2006

4. TITLE AND SUBTITLE
Residual Stress and Fracture of PECVD Thick Oxide Films for Power MEMS Structures and Devices

5a. CONTRACT NUMBER

5b. GRANT NUMBER
F49620-03-1-0078

5c. PROGRAM ELEMENT NUMBER

6. AUTHOR(S)
Professor Xin Zhang

5d. PROJECT NUMBER

5e. TASK NUMBER

5f. WORK UNIT NUMBER

7. PERFORMING ORGANIZATION NAME(S) AND ADDRESS(ES)
Department of Manufacturing Engineering
Boston University
15 Saint Mary's Street
Brookiline MA 02446-8200

8. PERFORMING ORGANIZATION REPORT NUMBER

9. SPONSORING/MONITORING AGENCY NAME(S) AND ADDRESS(ES)
USAF/AFRL
AFOSR
875 North Randolph Street
Arlington VA 22203
Dr Buunp Upleee/NA

10. SPONSOR/MONITOR'S ACRONYM(S)

AFRL-SR-AR-TR-07-0261

12. DISTRIBUTION AVAILABILITY STATEMENT

Distribution Statement A: Approved for public release. Distribution is unlimited.

13. SUPPLEMENTARY NOTES

14. ABSTRACT

Plasma enhanced chemical vapor deposited (PECVD) silicon oxide (SiOx) is the most commonly used interlayer dielectric (ILD) in MEMS devices and structures. In this project, PECVD SiOx is chosen as an example for the systematic study of mechanical behavior and underlying casual mechanisms of amorphous thin films for MEMS applications, which are generally less well understood because of the complex interplay among the deformation mechanisms.

15. SUBJECT TERMS

16. SECURITY CLASSIFICATION OF:			17. LIMITATION OF ABSTRACT	18. NUMBER OF PAGES	19a. NAME OF RESPONSIBLE PERSON
a. REPORT Unclassified	b. ABSTRACT Unclassified	c. THIS PAGE Unclassified	Unclassified	163	19b. TELEPONE NUMBER (Include area code) (703)

Standard Form 298 (Rev. 8-98)
Prescribed by ANSI-Std Z39-18

RESIDUAL STRESS AND FRACTURE OF PECVD THICK OXIDE FILMS FOR POWER MEMS STRUCTURES AND DEVICES

(AWARD #: F49620-03-1-0078)

FINAL REPORT TO THE AIR FORCE OFFICE OF SCIENTIFIC RESEARCH

Dr. Les Lee, Program Manager for Mechanics of Materials & Devices (Tel: 703-696-8483; Fax: 703-696-8451; E-mail: les.lee@afosr.af.mil)

Submitted on 06/30/2007

PRINCIPAL INVESTIGATOR AND TECHNICAL CONTACT:

XIN ZHANG, PH.D.
ASSOCIATE PROFESSOR
DEPARTMENT OF MANUFACTURING ENGINEERING AND
DEPARTMENT OF AEROSPACE AND MECHANICAL ENGINEERING
COLLEGE OF ENGINEERING, BOSTON UNIVERSITY
15 SAINT MARY'S STREET, BROOKLINE, MASSACHUSETTS 02446-8200
TEL: 617-358-2702; FAX: 617-353-5548; E-MAIL: XINZ@BU.EDU

Final Performance Report:

RESIDUAL STRESS AND FRACTURE OF PECVD THICK OXIDE FILMS FOR POWER MEMS STRUCTURES AND DEVICES

Principal Investigator: Dr. Xin Zhang, Associate Professor, Department of Manufacturing Engineering, Boston University, 15 Saint Mary's Street, Boston, MA 02215, USA; Tel: (617) 358-2702, Fax: (617) 353-5548, E-mail: xinz@bu.edu

Program Manager: Dr. B. L. ("Les") Lee, Mechanics of Multifunctional Materials & Microsystems, AFOSR, 875 N. Randolph Street, AFOSR/NA, Suite 325, Room 3112, Arlington, VA 22203, USA; Tel: (703) 696 8483, Fax: (703) 696 8451, E-mail: ByungLip.Lee@afosr.af.mil

Major Personnel:
- Faculty: Prof. Xin Zhang
- Graduate Student: Zhiqiang "Jay" Cao*

(* Zhiqiang "Jay" Cao graduated with a PhD degree in May 2007. He has been worked on this grant during his entire Ph.D. thesis work. *His Ph.D. thesis, entitled Mechanical Behaviors of PECVD Dielectric Films for MEMS Applications, is available at Boston University Library. If you are interested in getting a copy of the thesis, please contact Prof. Xin Zhang at the address given above.*)

Abstract

Plasma enhanced chemical vapor deposited (PECVD) silicon oxide (SiOx) is the most commonly used interlayer dielectric (ILD) in MEMS devices and structures. In this project, PECVD SiO_x is chosen as an example for the systematic study of mechanical behavior and underlying causal mechanisms of amorphous thin films for MEMS applications, which are generally less well understood because of the complex interplay among the deformation mechanisms.

Mechanical behaviors of the PECVD SiO_x thin films are probed at 1) different size scales (from wafer level down to micro/nano-scale, and different length-scale within each realm); 2) different temperatures (from room temperature up to 1100 °C); and 3) with a combination of different experimental techniques (such as substrate curvature measurements, nanoindentation tests, and a novel "microbridge testing" technique, etc.). A broad range of mechanical analysis is covered, including film stress and related material properties changes, elastic properties, plastic properties (both time-independent and time-dependent), deformation mechanisms (both at room temperature and elevated temperatures). Wherever applicable, materials analysis techniques such as SEM, AFM, FTIR, XRD, and SIMS were employed to strengthen the discussions on the structure-properties relationship and the causal mechanisms of the mechanical responses of the PECVD SiO_x. These experiments reveal various interesting and distinctive characteristics of the mechanical responses of the PECVD SiO_x thin films, and the microstructural causal mechanisms for each of them are analyzed in depth.

The outcome of this work will provide a comprehensive characterization of the mechanical responses of the PECVD SiO_x thin films under different thermal conditions, stress levels, size scales, and in both elastic and plastic regions. In addition, both new experimental methodologies and theoretical models for data

analysis are resulted, which can be readily applied to a wide variety of thin film materials for various different applications. Last but not least, the physical causal mechanisms for the experimental results are elucidated, which is a significant contribution to the scientific understanding of this type of amorphous thin film materials. These theoretical interpretations will also provide valuable insights to the understanding of similar responses of many other similar amorphous thin film materials for MEMS applications.

Major Publications

Under the support of this AFOSR grant and the direct management of Program Manager Dr. Les Lee at AFOSR, <u>we have published 6 journal papers, 6 conference proceeding papers, and given 16 presentations at national and international conferences. One graduate student Mr. Zhiqiang Cao also finished his Ph.D. thesis in January 2007.</u> All of journal and conference proceeding papers (in PDF format) are available at http://people.bu.edu/xinz. Dr. Zhiqiang Cao's Ph.D. thesis is available at Boston University Library. Should you need any hard copies of these publications, please feel free to contact Prof. Xin Zhang at the address given in the beginning of the report.

<u>Journal Articles</u>

[J.1] Cao Z and Zhang X, "Nanoindentation Stress-Strain Curves of PECVD Silicon Oxide Thin Films for MEMS Applications", in press, *Thin Solid Films*.

[J.2] Cao Z and Zhang X (2006), "Size-dependent Creep Behavior of Plastic Deformation in Plasma-Enhanced Chemical Vapor Deposited Silicon Oxide Films", *Journal of Physics D: Applied Physics* **39**, 5054-5063.

[J.3] Cao Z and Zhang X (2007), "Nanoindentation Creep of Plasma-Enhanced Chemical Vapor Deposited Silicon Oxide films", *Scripta Materialia* **56** (3), 249-252.

[J.4] Cao Z and Zhang X (2006), "Experiments and Theory of Thermally-induced Stress Relaxation in Amorphous Dielectric Films for MEMS and IC Applications," *Sensors and Actuators A: Physical* **127**, 221-227.

[J.5] Cao Z, Zhang TY, and Zhang X (2005), "Microbridge Testing of Plasma-Enhanced Chemical Vapor Deposited Silicon Oxide Films on Silicon Wafers," *Journal of Applied Physics* **97** (10), 104909 (1-9) (2005).
Also selected for *Virtual Journal of Nanoscale Science and Technology*, Subject Area: MEMS/NEMS, **11** (19).

[J.6] Cao Z and Zhang X (2004), "Density Change and Viscous Flow during Structural Relaxation of Plasma-Enhanced Chemical Vapor Deposited Silicon Oxide Films," *Journal of Applied Physics*, **96** (8), 4273-4280.

Referred Conference Proceeding Publications (Full Paper)

[P.1] Z. Cao and X. Zhang, "Measurement of Stress-strain Curves of PECVD Silicon Oxide Thin Films by Means of Nanoindentation," Processing-Structure-Mechanical Property Relations in Composite Materials, Materials Research Society Symposium Proceedings, in press.

[P.2] Cao Z and Zhang X (2006), "Influence of size effect on strain rate sensitivity and creep in plasma-enhanced chemical vapor deposited silicon oxide films,"

Mechanisms of Mechanical Deformation in Brittle Materials, *Materials Research Society Symposium Proceedings*, 904E, 0904-BB04-21.

[P.3] Cao Z, Zhang TY, and Zhang X (2005), "A Nanoindentation-based Microbridge Testing Method for Mechanical Characterization of Thin Films for MEMS Applications," *Proceeding of the 2005 ASME International Mechanical Engineering Congress and Exposition (ASME '05)*, Orlando, FL, USA, November 5-11, 2005, IMECE2005-80288.

[P.4] Cao Z and Zhang X (2005), "Mechanism of Temperature-Induced Plastic Deformation of Amorphous Dielectric Films for MEMS Applications," *Proceeding of the 18th IEEE International Conference on Micro Electro Mechanical Systems (MEMS '05)*, Miami Beach, FL, USA, January 30 - February 3, 2005, pp. 471-474.

[P.5] Cao Z, Zhang TY, and Zhang X (2004), "Microbridge Nanoindentation Testing of Plasma-Enhanced Chemical Vapor Deposited Silicon Oxide Films," Fundamentals of Nanoindentation and Nanotribology III, *Materials Research Society Symposium Proceedings*, 841, R12.4.1-6.

[P.6] Cao Z and Zhang X (2004), "Thickness-dependent Structural Relaxation of Plasma-Enhanced Chemical Vapor Deposited Silicon Oxide Films during Thermal Processing," Stability of Thin Films and Nanostructures, *Materials Research Society Symposium Proceedings*, 854, U8.1.1-6.

Conference Presentations

[C.1] Z. Cao and X. Zhang, "Measurement of Stress-strain Curves of PECVD Silicon Oxide Thin Films by Means of Nanoindentation," Processing-Structure-Mechanical Property Relations in Composite Materials, *Presented at 2007*

Materials Research Society Fall Meeting, Boston, MA, USA, November 27 - December 1, 2006.

[C.2] Z. Cao and X. Zhang, "Size Effects in Nanoindentation Creep of Plasma-enhanced Chemical Vapor Deposited Silicon Oxide Films," Size Effects in the Deformation of Materials -- Experiments and Modeling, *Presented at 2007 Materials Research Society Fall Meeting*, MA, USA, November 27 - December 1, 2006.

[C.3] X. Zhang, "Residual Stress and Fracture of Power MEMS Structures and Devices," Mechanics of Materials & Devices and Structural Mechanics, *Presented at the AFOSR Contractors' Meeting (AFOSR '06)*, Seattle, WA, USA, August 28-30, 2006.

[C.4] Z. Cao and X. Zhang, "Size-Effects in Nanoindentation Creep of Plasma-Enhanced Chemical Vapor Deposited Solicon Oxide Films," Thin Film & Small Scale Mechanical Behavior, *Presented at the Gordon Research Conference*, Waterville, ME, USA, July 30 - August 4, 2006.

[C.5] Z. Cao and X. Zhang, "Length-scale Effect on Nanoindentation Creep in Plasma-Enhanced Chemical Vapor Deposited Silicon Oxide Films," *Presented at the IEEE Solid-State Sensor and Actuator Workshop (Hilton Head '06)*, Hilton Head Island, SC, USA, June 4-8, 2006.

[C.6] Z. Cao, T-Y Zhang, and X. Zhang, "Influence of Size Effect on Strain Rate Sensitivity and Creep in Plasma-Enhanced Chemical Vapor Deposited Silicon Oxide Films," Mechanisms of Mechanical Deformation in Brittle Materials, *Presented at the 2005 Materials Research Society Fall Meeting*, Boston, MA, USA, November 28 - December 2, 2005.

[C.7] Z. Cao, T-Y Zhang, and X. Zhang, "A Nanoindentation-based Microbridge Testing Method for Mechanical Characterization of Thin Films for MEMS Applications," *Presented at the 2005 ASME International Mechanical Engineering Congress and Exposition (ASME '05)*, Orlando, FL, USA, November 5-11, 2005.

[C.8] Z. Cao, T-Y Zhang, and X. Zhang, "Microbridge Testing of Plasma Enhanced Chemical Vapor Deposited Silicon Oxide Films on Silicon Wafers," *Presented at the 52nd International Symposium & Exhibition of the American Vacuum Society, Boston (AVS '05)*, MA, USA, October 30 - November 4, 2005.

[C.9] X. Zhang, "Residual Stress and Fracture of Thick Plasma-Enhanced CVD Oxide Films for Power MEMS Structures and Devices," Mechanics of Materials & Devices and Structural Mechanics, *Presented at the AFOSR Contractors' Meeting (AFOSR '05)*, Santa Fe, NM, USA, August 29 - September 1, 2005.

[C.10] Z. Cao and X. Zhang, "Mechanism of Temperature-Induced Plastic Deformation of Amorphous Dielectric Films for MEMS Applications," *Presented at the 18th IEEE International Conference on Micro Electro Mechanical Systems (MEMS '05)*, Miami Beach, FL, USA, January 30 - February 3, 2005.

[C.11] Z. Cao, T-Y Zhang, and X. Zhang, "Microbridge Nanoindentation Testing of Plasma-Enhanced Chemical Vapor Deposited Silicon Oxide Films," Fundamentals of Nanoindentation and Nanotribology III, *Presented at the 2004 Materials Research Society Fall Meeting*, Boston, MA, USA, November 29 - December 3, 2004.

[C.12] Z. Cao and X. Zhang, "Thickness-dependent Structural Relaxation of Plasma-Enhanced Chemical Vapor Deposited Silicon Oxide Films during

Thermal Processing," Stability of Thin Films and Nanostructures, *Presented at the 2004 Materials Research Society Fall Meeting*, Boston, MA, USA, November 29 - December 3, 2004.

[C.13] X. Zhang, "Residual Stress and Fracture of Thick Plasma-Enhanced CVD Oxide Films for Power MEMS Structures and Devices," Mechanics of Materials & Devices and Structural Mechanics, *Presented at the AFOSR Contractors' Meeting (AFOSR '04)*, Wintergreen, VA, USA, August 18-20, 2004.

[C.14] Z. Cao and X. Zhang, "Residual Stress and Fracture of Power MEMS Structures and Devices," Thin Film & Small Scale Mechanical Behavior, *Presented at the Gordon Research Conference*, Waterville, ME, USA, July 18-23, 2004.

[C.15] Z. Cao and X. Zhang, "Investigation of Thermo-Mechanical Behavior of Multi-Layer Thin-Film Structures for MOEMS and Power MEMS Applications," Thin Films-Stresses and Mechanical Properties X, *Presented at the 2003 Materials Research Society Fall Meeting*, Boston, MA, USA, December 1-5, 2003.

[C.16] X. Zhang, "Residual Stress and Fracture of Thick Plasma-Enhanced CVD Oxide Films for Power MEMS Structures and Devices," Mechanics of Materials & Devices and Structural Mechanics, *Presented at the AFOSR Contractors' Meeting (AFOSR '03)*, Santa Fe, NM, USA, September 8-11, 2003.

1. INTRODUCTION

1.1. Project Summary

The objective of this research is to contribute to the scientific understanding of the full mechanical responses and related physical processes of amorphous MEMS thin film materials under different processing conditions and at different length scales.

MEMS (microelectromechanical systems) devices and structures have found wide applications in aerospace, automotive, communications, optics, biotechnology, and so on.

In MEMS, many of the most important failure mechanisms such as fracture, buckling and delamination are mechanical in nature. Successful design and fabrication of MEMS requires a fundamental understanding of the mechanics and physics of thin films. Amorphous thin film materials are more and more routinely adopted in the emerging applications of MEMS. However, their mechanical behavior is still not yet well understood compared with their crystalline counterparts. Particularly, amorphous plasma-enhanced chemical vapor deposited (PECVD) silicon oxide (SiO_x) is the most commonly used interlayer dielectric (ILD) in MEMS devices and structures, and often causes severe stress-related reliability problems under different processing conditions. Further, the mechanical responses are influenced by the length-scale it is probed. In this project, PECVD SiO_x is chosen as an example for the *systematic* study of the mechanical behaviors and underlying causal mechanisms of amorphous thin films for MEMS applications. Specifically, six major topics will be covered:

1) Microscale residual stress and Young's modulus measurement, by means of "microbridge testing".

2) Complete micro/nano scale elastic-plastic properties characterization, by means of "nanoindentation stress-strain curves".

3) Time-dependent plasticity (creep) and length-scale effects, by means of "nanoindentation load relaxation" experiments.

4) Room temperature plastic deformation mechanisms, including physical origin of transformation units, character of plastic flow, and cause of rate-sensitivity and size-effect.

5) Experimental investigation of structural relaxation phenomena at elevated temperatures, including intrinsic stress evolution, materials properties changes etc., by mean of *in-situ* and *ex-situ* wafer curvature measurements.

6) Deformation mechanism at elevated temperatures, and its link to the microstructural changes of the material.

In summary, the mechanical behaviors of the PECVD SiO_x thin films are probed at 1) *different size scales* (from wafer level down to micro/nano-scale, and different length-scale within each realm); 2) *different temperatures* (from room temperature up to 1100 °C); and 3) *with a combination of different experimental techniques* (such as substrate curvature measurements, nanoindentation tests, and a novel "microbridge testing" technique, etc.). These experiments reveal various interesting and distinctive characteristics of the mechanical responses of the PECVD SiO_x thin films, and the *microstructural causal mechanisms* for each of them are analyzed in depth.

The outcome of this work will provide a comprehensive characterization of the mechanical responses of the PECVD SiO_x thin films under different thermal conditions, stress levels, size scales, and in both elastic and plastic regions. In addition, both new theoretical models and experimental methodologies are resulted. The physical causal mechanisms for the experimental results are

elucidated, which is a significant contribution to the scientific understanding of this type of amorphous thin film materials.

The theoretical interpretations in this project will also provide valuable insights to the understanding of similar responses of other CVD materials (such as SiN_x and fluorosilicateglass) commonly used in the Microelectronics and MEMS industries, as well as physical vapor deposited (PVD) materials (such as AlO_x), spin-on glass materials and low-k silsesquioxane-based materials. The experimental methods developed in this research can be also readily applied to a wide variety of thin film materials for various different applications.

1.2. Background and Significance

1.2.1. Thin film materials: A mechanical perspective

Thin film materials have been widely used in microelectronic devices and packages; Microelectromechanical Systems or MEMS (Gad-el-Hak 2002; Madou 2002), and surface coatings with thermal, mechanical, tribological, environmental, optical, electrical, magnetic, or biological functionalities (Ohring 1992; Freund and Suresh 2004).

This project is primarily motivated by thin film applications in MEMS devices and structures, which as sensors and actuators have found numerous applications in aerospace, automotive, communications, optics, biotechnology, and so on (Gad-el-Hak 2002; Madou 2002).

Thin films in MEMS must satisfy a large set of rigorous chemical, structural, mechanical, and electrical requirements. Excellent adhesion, low residual stress, low pinhole density, good mechanical strength, and chemical resistance may be required simultaneously. It is well known that as manufacturing operations approach micron scale, or even submicron/nanoscale, material properties of thin film materials generally differ from their bulk counterparts (Ohring 1992; Freund and Suresh 2004). It is thus crucial to

12

understand the unique properties of the MEMS thin film materials, in order to better design, characterize, and manufacture successful MEMS devices and structures for the next generation.

Of particular interests are the *mechanical responses* of the thin film materials, which will be the focus of this research. This is first because, as the acronym suggests, MEMS typically integrate *mechanical* components with the electronics required for control. In other words, it usually contains a movable part of some sort, which creates a special need for the understanding of the *micromechanics* of the device. Secondly, many deleterious effects during MEMS fabrication and integration, such as excessive wafer bowing, film cracking, delamination, and defects formation etc., are related to the residual stress in the films and are *mechanical* in nature. Last but not least, the long-term reliability of MEMS relies on the time-dependent *mechanical* properties of the thin films, such as creep and fatigue, etc. This is especially important for those MEMS devices and structures working in "harsh environments", i.e. high temperature, high stress level, and/or high strain rates etc. Examples include pressure sensors for aerospace applications, micro heat engines and related components, etc (Epstein and Senturia1997; Frechette et al 2000, 2005; Spadaccini et al 2002, 2003; Wong et al 2004; Zhang X et al 2003; Jan Peirs et al 2004; Miki et al 2003).

Mechanical properties of interest generally fall into three categories: elastic, plastic, and strength (Gad-el-Hak 2002). The designer of a microdevice needs to know the elastic properties in order to predict the amount of deflection/deformation from an applied force, or vice versa. If the material is ductile and deformed structure does not need to return to its initial state, then the knowledge of plastic behavior of the material under the specific processing condition is necessary. The strength of the material (related to plastic yielding for inelastic materials) must be known so that the allowable operating limits can be set. As an ambitious attempt, in this project, we aim to perform experiments that

13

probe the *full* mechanical responses covering all three categories, providing a complete mechanical characterization of the material.

For most MEMS thin films, the material properties depend strongly on the deposition process and post-deposition thermal processing, which includes both thermal cycling and annealing. For this reason, in this project, the relation between thermal processing conditions and mechanical properties changes is given special attention. Additionally, the thermally induced structural relaxation phenomena, which are driving the material properties changes, are studied systematically.

1.2.2. Amorphous thin films for MEMS applications

Due to the reasons outlined in Sec. 1.2.1, mechanical characterization of MEMS thin film materials has been an active area of research. Yet the bulk of the previous research is focusing on crystalline/polycrystalline materials such as metal films. In comparison, both the theoretical and experimental investigations of amorphous thin film materials are not nearly as well developed. The reasons are twofold: first, crystalline and polycrystalline materials, such as metals, poly silicon etc, have had much more applications in the MEMS/semiconductor industry; and second, crystalline/polycrystalline materials are easier to relatively model and characterize due to their relative microstructural simplicity. However, with the rapid development of the microelectronics and MEMS industries, more and more amorphous "unconventional" materials, such as the spin-on polymer glasses (Cook and Liniger 1999) and low-*k* silsesquioxane-based dielectric films etc (Stadtmüeller et al 1992; Baney et al 1995; Hollahan 1979), are being adopted to meet the challenges of the ever-increasingly demanding applications. On the other hand, many "conventional" amorphous semiconductor materials, such as PECVD SiO_x and PECVD SiN_x films etc., have found new applications in which they serve as a mechanical element. Thus it has become more and more imperative that the mechanical responses and related physical processes of the

amorphous thin film materials need to be investigated more systematically and thoroughly.

It is our expectation that the outcome of this work will significantly contribute to the scientific understanding of the mechanical behavior and associated causal mechanisms of amorphous thin film materials for MEMS applications. Consequently, novel engineering approaches for device fabrication and process integration of MEMS/microelectronics may be inspired by the newly gained scientific insights from this research.

1.2.3. PECVD SiO$_x$ and example of applications

Plasma enhanced chemical vapor deposition (PECVD) is a special chemical vapor deposition (CVD) process that is facilitated by RF plasma. A schematic of the PECVD process is illustrated in Fig. 1.1. It enables dielectric films such as oxides, nitrides, and oxynitrides to be deposited at relatively low temperatures (300~400°C) (Madou 2002). Because of its fast deposition rate, normally ~1μm/min, as-deposited PECVD films are typically amorphous in microstructure. It is also the only practical technique to deposit dielectric films with a thickness greater than a few microns.

PECVD SiO$_x$ is the most commonly used interlayer dielectric (ILD) in MEMS devices and structures. In addition to providing electrical and *mechanical* stability, they also serve as etch-stops and chemical-*mechanical* polish stops during device processing (Thurn et al 2004). The *mechanical* properties of the PECVD SiO$_x$ is thus of paramount importance in determining structural integrity of the MEMS devices and structures. For these reasons, in this project, PECVD SiO$_x$ thin film material is chosen as a case-study material, and its residual stresses, elastic and plastic properties are studied in depth.

A specific example of application in MEMS for PECVD SiO$_x$, which showcases the importance of the above characterizations, is given next. Fig. 1.2 shows a die-level picture of a stator for the micromotor compressor used in

Power MEMS (Epstein and Senturia1997; Frechette et al 2000, 2005; Spadaccini et al 2002, 2003; Wong et al 2004; Zhang X et al 2003; Jan Peirs et al 2004; Miki et al 2003). The micromotor compressor must have high power density and operate at high efficiency. This, in turn, places several requirements on the electrical stator. *First*, it must operate at high voltages (~300V) without electrical breakdown. *Second*, the electrodes and interconnects must be well insulated from the substrate to minimize capacitive loading. *Finally*, the process must lead to a planar, unbowed surface to permit wafer bonding, and to ensure a few micron of air gap between the rotor and the stator. To meet these requirements, the stator electrical elements must be fabricated on top of a thick, high quality oxide film, as thick as can be fabricated. To achieve this, two goals in film fabrication had to be met. *First*, sufficient thickness (typically, greater than 10 μm) is required in order to reduce capacitive loading. *Second*, the breakdown strength of the insulating film had to be able to withstand the high applied electrical loads.

In order to achieve the first goal, PECVD SiO$_x$ was chosen (Fig. 1.3) for a high deposition rate (~1 μm/min) (Madou 2002). After deposition, the oxide films were subjected to a high temperature (typically 1100°C) densification to achieve better breakdown strength. Unfortunately, thick oxide (10-40 μm) is difficult to work with because of residual stress. *The deleterious effects of residual stress that tend to increase with thickness are a prime limitation to the deposition of very thick films.* Depositing oxide films with the required thickness is not difficult, however, after densification, the wafer exhibited excessive distortion and cracks were found in the film if the film thickness exceeded a critical thickness (Zhang X et al 2001, 2002, 2003; Chen et al 2003). Residual stress leads to large overall wafer bow, which makes further processing difficult. For example some microfabrication machines, such as chemical mechanical polishing, even cannot pick up the wafer. The compressive film on one side of the wafer applies a bending torque on the substrate, curving the wafer; PECVD SiO$_x$ films are

typically compressive, bowing the wafer with the film on the convex surface. If very severe, wafer bow can also prohibit wafer bonding. Wafer bonding of excessively bowed wafers with thick oxide films was found to be extremely challenging (Nagle 2000; Frechette 2000; Ayon et al 2003). Furthermore, as the film is made thicker and thicker, the wafer simply cannot bow enough to relieve the stress, and the films crack. A device integration failure caused by excessive residual stresses is shown in Fig. 1.4.

1.3. Scope of the Work

The author would like to emphasize that the scope of this wprk is not at all limited by Power MEMS, which is only one specific application that could benefit from this research. Although motivated by thin film applications in MEMS, this project primarily focuses on the fundamental scientific understanding of the mechanical behaviors of the case-study material: PECVD SiO_x. Specifically, a broad range of mechanical analysis is covered, including film stress and related material properties changes, elastic properties, plastic properties (both time-independent and time-dependent), and deformation mechanisms (both at room temperature and elevated temperatures). The thin film materials were systematically studied both experimentally and theoretically at different stress levels, different temperatures, and different length-scale. Wherever applicable, materials analysis techniques such as SEM, AFM, FTIR, XRD, and SIMS were employed to strengthen the discussions on the structure-properties relationship and the causal mechanisms of the mechanical responses of the PECVD SiO_x.

New mechanical characterization techniques were developed as needed, such as the microbridge testing method. "Conventional" experimental methods, such as the nanoindentation, were re-invented to measure "non-conventional" properties like the stress-strain curves and the stress-exponents. The wafer-curvature measurements were exploited theoretically to yield more information

17

about materials properties changes, such as density and viscosity. Based on these experimental results, we have derived various theoretical models to account for the observed mechanical responses and the deformation mechanisms of the studied material.

As pointed out in Sec. 1.1, the experimental methods and the scientific insights from the in-depth study of PECVD SiO_x films will also contribute to the analysis of similar responses of other CVD materials (such as SiN_x and fluorosilicateglass) (Habermehl 1998; Blaauw 1983; Lubguban et al 2000) commonly used in the Microelectronics and MEMS industries, physical vapor deposited (PVD) materials (such as AlO_x) (Gardner 1977), spin-on glass materials (Cook and Liniger 1999), and low-*k* silsesquioxane-based materials (Stadtmüeller et al 1992; Baney et al 1995; Hollahan 1979).

1.4. Report Outline

This section (Sec.1) briefly summarizes the objective and scope of the work. The subjects of study, motivation and significance, as well as example of applications are introduced. Major contributions of each of the following sections are outlined below:

Sec.2 describes all the major *experimental methods* employed in this project in a comprehensive way. They are: 1) Wafer curvature measurement experiments (during/after thermal cycling and annealing); 2) Microbridge testing (of micro/local scale residual stress and Young's modulus); 3) Nanoindentation techniques (for measuring micro/nano scale mechanical responses, such as indentation strain rate etc.) and 4) Materials analysis techniques, including SEM, FTIR, XRD, etc.

Sec.3 is devoted to the "microbridge testing" method, and its application of measuring *microscale residual stress and elastic properties* in the PECVD SiO_x

films undergone different thermal processing. Both the theoretical modeling and experimental results are presented.

Sec.4 explores the use of nanoindentation techniques as a method of measuring *equivalent stress-strain curves* of the PECVD SiO_x thin films. Various different indenter tips were adopted in our experiments, enabling us to probe the elastic, elasto-plastic, and fully plastic deformation regimes of the PECVD SiO_x thin films. Based on the experimental results, a shear transformation zone (STZ) based amorphous plasticity theory is applied to explain the plastic deformation mechanism in the PECVD SiO_x.

Sec.5 focuses on the *time-dependent plastic deformation (creep)* behaviors of both the as-deposited and annealed PECVD SiO_x films. Nanoindentation load relaxation tests were performed at room temperature, and found a strong size effect in the creep responses of the as-deposited PECVD SiO_x thin films, which was much reduced after rapid thermal annealing (RTA). Based on the experimental results, the deformation mechanism is again depicted by the "shear transformation zone" (STZ) based amorphous plasticity theories.

Sec.6 investigates the *structural relaxation* phenomena of the PECVD SiO_x films at *elevated temperatures* (i.e. during thermal cycling and annealing). The stresses in the PECVD SiO_x films, determined by the wafer curvature measurement experiments, are shown to be sensitive to both viscosity and density changes of the material. A microstructure bonding-based mechanism is proposed to explain a series of experimental results that are related to thermal cycling as well as annealing of PECVD SiO_x films including stress hysteresis generation and reduction, and coefficient of thermal expansion (CTE) changes. In particular, the thickness effect is examined; PECVD SiO_x films with a thickness varying from 1 to 40 µm will be studied.

Finally, Sec.7 concludes the work by summarizing the major contributions of the work and pointing out potential future research directions.

Except for Sec. 1, 2, and 7, the other sections of the report are written in a format that resembles a journal article, complete with its own abstract, introduction, experimental details, results and discussion, and conclusions. As such, they can both serve as an integral part of the whole report, and be a good source of reference should one decide to read only parts of the report. For the convenience of the reader, a complete bibliography containing the references in all the sections is provided at the end of the report. Figures are separated from the texts and listed at the end of each section.
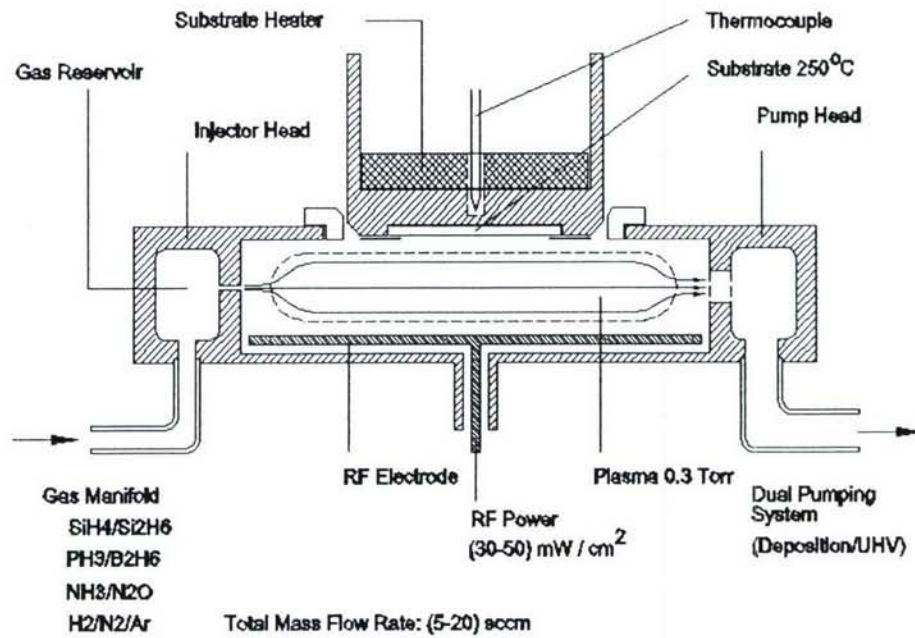
Fig.1.1. A schematic of the PECVD process (Madou 2002).
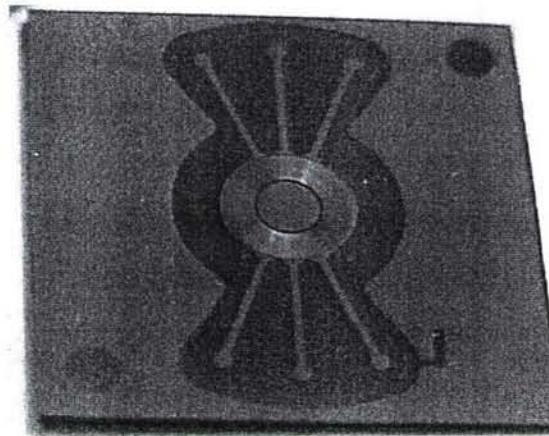
Fig.1.2. Optical photograph of a motor compressor stator after thin film processing (Zhang X et al 2001).
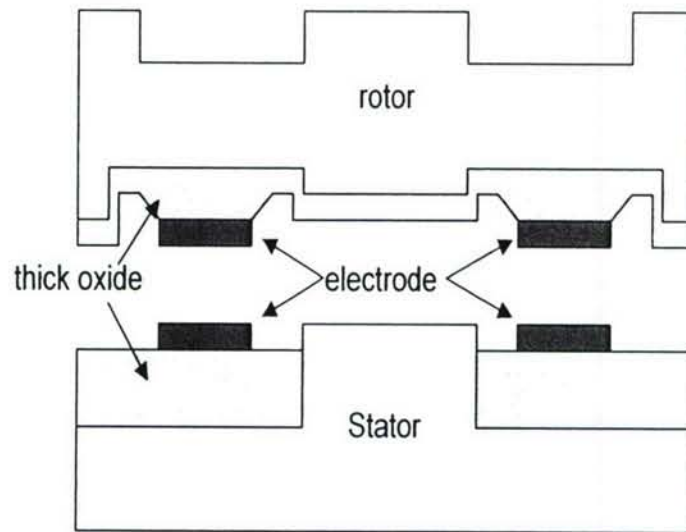
Fig.1.3. Cross section view showing PECVD SiO_x in micromotor compressor (Chen et al 2003).
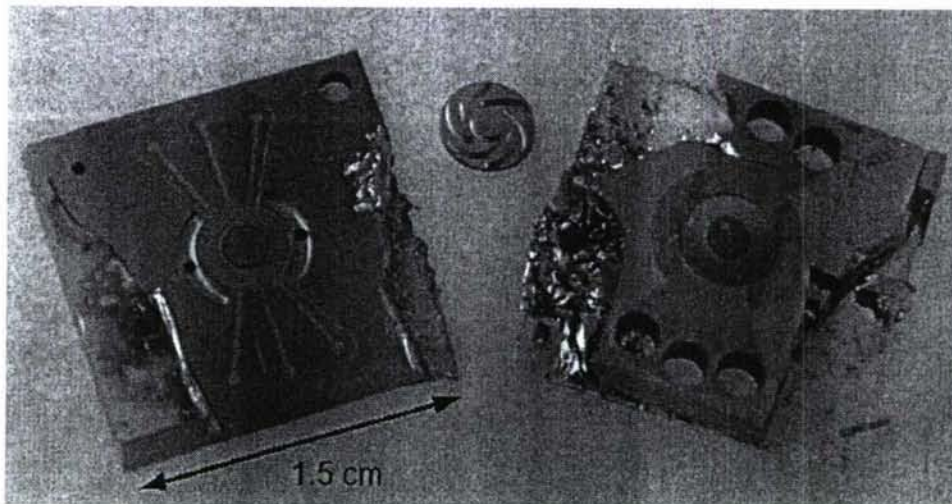
Fig.1.4. A device integration failure caused by residual stresses (Zhang X et al 2002).

2. EXPERIMENTAL METHODS

2.1. Statement of Objectives

In MEMS, many of the most important failure mechanisms such as fracture, buckling and delamination are mechanical in nature. Successful design and fabrication of MEMS requires a fundamental understanding of the mechanics and physics of thin films. Amorphous thin film materials are more and more commonly adopted in emerging new applications of MEMS. However, their mechanical behavior is still not yet well understood as compared with their crystalline counterparts. Particularly, amorphous plasma-enhanced chemical vapor deposited (PECVD) silicon oxide (SiO_x) is the most commonly used interlayer dielectric (ILD) in MEMS devices and structures, and often cause severe stress-related reliability problems under different processing conditions. In this research, PECVD SiO_x is chosen as an example for the systematic study of the mechanical responses and related physical processes of thin films for MEMS applications. Specifically, six major topics will be covered:

1) Microscale residual stress and Young's modulus measurement, by means of "microbridge testing".
2) Complete micro/nano scale elastic-plastic properties characterization, by means of "nanoindentation stress-strain curves".
3) Time-dependent plasticity (creep) and length-scale effects, by means of "nanoindentation load relaxation" experiments.
4) Room temperature plastic deformation mechanisms, including physical origin of transformation units, character of plastic flow, and cause of rate-sensitivity and size-effect.
5) Experimental investigation of structural relaxation phenomena at elevated temperatures, including intrinsic stress evolution, materials properties

changes etc., by mean of *in-situ* and *ex-situ* wafer curvature measurements.

6) Deformation mechanism at elevated temperatures, and its link to the microstructural changes in the material.

2.2. Wafer Level Experiments

2.2.1. Film deposition

In this project, all PECVD oxide films were deposited using a five-station continuous plasma processing system (Concept One™, Novellus™ Inc., San Jose, CA). The substrate material used are 4 and 6 inch, <100> orientation boron doped silicon wafers. The nominal gas flow rates of silane-based oxide are 300 standard cubic center meters per minute of SiH_4, 500 sccm of N_2O and 1500 sccm of N_2. Depositions were carried out at 400°C with a nominal deposition rate of 1 µm/min. The chemical reaction of silane-based oxide can be expressed as:

$$SiH_{4(g)} + 2N_2O_{(g)} \xrightarrow[\Delta]{RF} SiO_{2(s)} + 2N_{2(g)} + 2H_{2(g)} \qquad \text{(Eq. 2.1)}$$
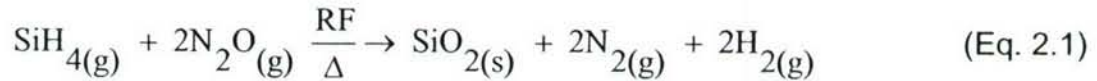
2.2.2. Thermal-mechanical responses

The basic stress-temperature behavior of thick oxide materials is not well understood. In Sec.6, thermal cycling tests will be conducted to assess the role of temperature dependent effects in determining the stress state in thick oxide films. The KLA-Tencor™ FLX wafer curvature measurement system (from KLA-Tencor Inc., San Jose, CA), shown in Fig.2.1 (a), will be used to carry out oxide-temperature experiments. It is capable of taking multiple optical scans to generate a map of wafer curvature while the high-temperature one can measure wafer curvature continuously during a temperature ramp. Room temperature wafer curvature will be measured across the wafer surface in 12 scans, rotating

the wafer by 30° between each scan. In situ wafer curvature will be measured between room temperature and 500°C. The heating rate will be ranged from 1-5°C/min. Subsequent analysis will be carried out to estimate the residual stress from the curvature of the wafer (see Sec. 2.2.4).

2.2.3. High temperature thermal cycling experiments

Note that 500°C is the maximum temperature that the Tencor system could reach. In order to turn our attention to the temperature response between 500°C and 1100°C, wafers coated with thick oxide films will be subjected to subsequent thermal cycling in an Instron[TM] MDS791 furnace with a CU666D temperature controller. Curvature measurements will be made after each cycling. A ramp up rate of between 0.5-1.0°C/min (near peak temperature) and 10°C/min (below deposition temperature) will be chosen for the proposed research. A 30-minute to 10-hour stabilization time will be set at the peak temperature to simulate annealing conditions. Observations of defects and curvature will be made after each cycle.

2.2.4. Data analysis

For a thin film on a relatively thick substrate (thin film approximation), the stress in the film can be calculated from the deflection of the free end of the beam as (Stoney equation) (Stoney 1909):

$$\sigma_f = \frac{E_s h_s^3}{6(1-v_s)Rh_f^2(1+h_s/h_f)} \tag{Eq. 2.2}$$

where $1/R$ is the curvature, h_s and h_f are thickness of substrate and film, respectively. E_s and v_s are Young's modulus and Poisson's ratio of the substrate. However, for the case of an oxide film with a relatively thick film thickness on a silicon substrate, the effect of *nonlinearity* must be taken into account.

In this project, we modified our experimental data by nonlinear finite element analyses using ABAQUS and a semi-analytical formulation developed

by Chen et al (Chen and Ou 2002). This formulation is based on the energy method and simultaneously considers effects of geometrical nonlinearity and mid-plane offset. With an appropriately assumed deformation shape, analytical solutions obtained by this method have a good agreement with highly meshed finite element simulation results (Chen and Ou 2002).

The Coefficient of Thermal Expansion (CTE) of the thin film material is then estimated from the following equation:

$$\frac{d\sigma_f}{dT} = \frac{E_f}{(1-v_f)}(\alpha_s - \alpha_f)$$
(Eq. 2.3)

Other materials properties changes, just as density and viscosity, may be also evaluated from a quantitative relation derived from stress-temperature curves, knowing the ramp rate. More details will be provided in Sec.6.

2.3. Microbridge Testing

2.3.1. Experiments

Wafer-deformation based mechanical characterization can only characterize stress/strain at the wafer level. In order to be able to perform local/micro scale mechanical characterization, many techniques have been developed, such as nanoindentation, uniaxial tensile testing of freestanding films, beam bending and bulge testing, etc (Hernandez et al 2002; Kucheyev et al 2000; Baker and Nix 1994; Shull and Spaepen 1996; Zhang TY and Xu 2002; Zheng et al 2000; Xu et al 2001; Fang and Wickert 1996; Brozen 1994; Vinci and Vlassak 1996).

Depth-sensing instrumentation, or nanoindentation is a popular technique for the estimation of mechanical properties of materials down to nanoscale. A picture of the Hysitron TriboIndenter[TM] nanoindentation system is shown in Fig.2.1(b), together with a schematic of typical load-displacement curve obtained by the nanoindenter (Oliver and Pharr 1992, 2004). The nanoindentation system

employs high-resolution sensors and actuators to continuously control and monitor the loads and displacements on an indenter as it is driven into and withdrawn from a material (Pharr 1998). More applications about nanoindentation techniques will be discussed later in this section.

In this section, we introduce a novel nanoindentation-based *microbridge testing* method, which has the advantage of being able to measure residual stress and Young's modulus of the thin film material simultaneously (Cao et al 2005). It is also easier to handle than uniaxile micro-tensile testing and avoids the problem of stress concentration of the bulge testing method (Cao et al 2005).

Free-standing single-layer microbridges made of PECVD SiO_x films were fabricated using state-of-the-art micromachining techniques (Madou 2002). A simplified fabrication process flow is shown in Fig. 2.2(a), and a fabricated sample microbridge array made of PECVD SiO_x films is shown in Fig. 2.2(b). The same fabrication process can be easily modified to manufacture other structures such as the microcantilever beams, shown in Fig.2.3. The major advantage of this process flow is that only one photomask is required, since the etchant that we used, Tetra Methyl Ammonium Hydroxide (TMAH), has a very high selectivity of silicon over silicon oxide (Madou 2002; Merlos et al 1992). A two-mask process flow design, shown in Fig.2.4, is also developed for general applications of fabricating freestanding microbridges (or cantilevers) made of a target thin film material.

A schematic depiction of the microbridge testing method is shown in Fig. 2.5(a). In the experimental setup, a nanoindenter applies the loads at the center of the microbridges, and obtains a high-resolution experimental load-displacement relationship. To analyze the data, we apply a theoretical model that uses a closed formula of deflection vs load, considering both substrate deformation and residual stress in the film (Cao et al 2005). Both residual stress and Young's modulus can be simultaneously evaluated. A brief summary of the

theoretical modeling will be provided in following Sec. 2.3.2. Mode details can be found in Sec. 3.

2.3.2. Data analysis

The mechanical analysis of the microbrige under a lateral load is illustrated in Fig. 2.5(b). When the residual stress is tensile ($N_r > 0$), the bridge deflection at the bridge center where the lateral load is applied is given by (Sec.3, Cao et al 2005):

$$w = -\frac{Q\tanh(kl/2)}{2N_x k} + \frac{Ql}{4N_x} - \frac{M_0}{N_x}[\frac{1}{\cosh(kl/2)} - 1] + S_{PN}(N_x - N_r) + S_{PP}\frac{Q}{2} - S_{PM}M_0$$

(Eq.2.4)

As shown in Fig. 2.5(b), l is the bridge length, N_r is the residual force per unit width in the middle plane of film along the length direction, N_x is the force per unit width in the middle plane along the length direction, $k = \sqrt{N_x/D}$, $D = E_f t^3/12$ with t being the film thickness and E_f the Young's modulus of the film. S_{ij} are the components of the compliance tensor reflecting substrate deformation (Fig. 2.6), and they depend only on the substrate properties and geometries, i.e. the support angle and film thickness. For a load Q, given an N_r and an E_f, N_x and generalized force M_0 can be calculated numerically from the following equations (Sec.3, Cao et al 2005):

$$M_0 = \frac{S_{MN}N_x(N_x - N_r) + \frac{1}{2}S_{MP}QN_x + \frac{1}{2}Q\left[\frac{1}{\cosh(kl/2)} - 1\right]}{S_{MM}N_x + k\tanh(kl/2)}$$

(Eq.2.5)

$$S_{NN}(N_x - N_r) + S_{NP}\frac{Q}{2} - S_{MM}M_0 = I - \frac{l(N_x - N_r)}{2E_f t}$$

(Eq.2.6)

$$I = \frac{1}{8}\left[\begin{array}{l}(a^2 + b^2 + 2c^2)kl + 8(a-b)c\sinh(kl/2) + 2abkl\cosh(kl) \\ + (a^2 + 2ab - b^2 + 8bc)\sinh(kl) + b^2\sinh(2kl)\end{array}\right]$$

(Eq.2.7)

$$a = -\frac{Q\sinh(kl/2)}{N_x\sinh(kl)} - \frac{M_0 k}{N_x\sinh(kl)}, \qquad b = \frac{M_0 k}{N_x\sinh(kl)}, \qquad c = \frac{Q}{2N_x}.$$

(Eq.2.8)

28

The applied load always acts as a stretching factor for the beam stress, resulting in a more tensile N_x. Thus if $N_x<0$, it corresponds to a compressive residual stress, i.e., $N_r<0$, and $|N_x|<|N_r|$. In this case, k is a pure imaginary number, and complex calculations are required. As a result, hyperbola functions $\sinh(x)$, $\cosh(x)$, and $\tanh(x)$ will be replaced by trigonal functions $\sin(x)$, $\cos(x)$ and $\tan(x)$.

The Young's modulus and residual stress are determined from fitting the experimental load-deflection curve with the theoretical solution by the least square technique, i.e. minimizing the positive function

$$S = \sum_{i=1}^{n} \left[w_i^e(Q_i) - w_i^t(Q_i, N_r, E_f) \right]^2 \qquad \text{(Eq.2.9)}$$

where n is the number of data, w_i^e is the experimentally observed deflection, and $w_i^t(Q_i, N_r, E_f)$ is the theoretical deflection obtained by the above equations. The iteration technique is used to regress the Young's modulus E_f and residual force N_r, which gives the residual stress as $\sigma_r = N_r/t$. Note that this method applies well only when deflection is large compared with film thickness. Otherwise, the non-linearity of the curve is not significant, and the solutions may not be unique. It should be noted that even a small difference in the load-deflection curve will lead to a large deviation in the Young's modulus and/or residual stress. That's why even the deformation of the substrate is small compared with total deflection; it should be taken into account so as to get more precise solutions.

2.3.3. Broader impacts

The microbridge testing method developed above may find broad applications in the mechanical characterization of thin films, which are of interest to the microelectronics and MEMS industries. In addition, a microbridge is a fundamental structure in MEMS, which may be applied in the microbridge-based sensors, such as the flow sensors, humidity sensors, and chemical gas sensors etc (Sec.3, Cao et al 2005).

2.4. Nanoindentation Tests

In applications such as Power MEMS, PECVD SiO_x endures a high level of stress even at low temperatures. Severe plastic deformations in the PECVD SiO_x thin films often occur, which cause device degradation or even prohibit the device process integration. So far, however, the plastic properties of the PECVD SiO_x, especially at lower temperatures, are not well understood.

At the microscale, the plastic responses of the thin films can be probed by many experimental methods. The most commonly used ones are: 1) micro tensile testing of a freestanding thin film (Huang and Spaepen 2000; Hommel and Kraft 2001), 2) microcantilever deflection (Baker and Nix 1994; Schwaiger and Kraft 2003) 3) bulge testing (Vlassak and Nix 1992; Xiang et al 2005); and 4) instrumented nanoindentation (Tymiak et al 2001; Bei et al 2004), etc.

As briefly introduced earlier, nanoindentation is a popular technique widely used for the estimation of mechanical properties of materials down to nanoscale. It can reveal a wealth of detailed information about the mechanisms and mechanics of the studied thin film materials, including elastic modulus, hardness, surface adhesion, creep, and stress relaxation behaviors, etc (Tymiak et al 2001; Bei et al 2004; Oliver and Pharr 1992, 2004; Lucas and Oliver 1999; Poisl et al 1995; Elmustafa and Stone 2003; Schuh and Nieh 2003, 2004; Schwaiger et al 2003; Li and Ngan 2004).

In this project, two types of nanoindentation experiments, constant rate of loading (CRL) and indentation load relaxation (ILR) (Poisl 1995), will be conducted on the blank PECVD SiO_x films. Both the time-independent and the time-dependent plastic responses are studied.

To gain more insights into the time-dependent properties of the PECVD SiO_x thin films, it is desirable to obtain the relationship between the nanoindentation strain rates ($\dot{\varepsilon_1}$) and the average indentation stress $\bar{\sigma}$.

30

A schematic of a nanoindentation test with a spherical tip and a sharp pyramidal shape is illustrated in Fig. 2.7. h and h_c are the measured depth (also the instant maximum depth) and the contact depth, respectively. In this case, the indentation strain rate at any stage is defined as (Poisl et al 1995; Tabor 1951):

$$\dot{\varepsilon_I} = \frac{1}{D}\frac{da}{dt} \qquad \text{(Eq. 2.10)}$$

where a is the radius of contact and $D = 2R$ is the diameter of the spherical indenter tip. From the similarity of triangles we can easily derive the expression of a, as

$$a = \sqrt{Dh_c - h_c^2} \qquad \text{(Eq. 2.11a)}$$

When $D \gg h_c$, we have

$$a \approx \sqrt{Dh_c} \qquad \text{(Eq.2.11b)}$$

For conical and pyramidal (such as Berkovich) tips, the indentation strain rate for deep indents is usually expressed as (Poisl et al 1995; Hill 1992; Bower et al 1993; Storåkers and Larsson 1994):

$$\dot{\varepsilon_I} = \frac{1}{h}\frac{dh}{dt} \qquad \text{(Eq.2.12)}$$

However, at very small depth, the shapes of the conical and pyramidal tips are rounded. For these tips, the maximum contact depth below which the indent shape is spherical can be estimated by the equation (Li and Ngan 2004):

$$\delta_0 = R(1 - \sin\beta) \qquad \text{(Eq.2.13)}$$

where β is the semiangle of the indenter tip. An equivalent expression for nanoindentation strain ε_I can also be derived by integration of $\dot{\varepsilon_I}$, by considering the tip shape changes during the indentation process. More details will be provided in Sec. 4.

2.4. Materials Characterization

Finally, several characterization techniques may be applied to further probe the PECVD oxide films. Scanning Probe Microscopy (SPM) is used together with nanoindentation to monitor the indentation area and shape, as well as "pile-up" and surface roughness effects. In-house optical microscopy and scanning electron microscopy (SEM) are applied to image the micro-fabricated samples, and measure geometries etc. For example, in Fig.2.8, the thicknesses of a 2 μm and a 5 μm PECVD SiO_x film were separately measured by the SEM.

Due to its amorphous nature, a direct determination of the microstructure in the stressed PECVD SiO_x films is a challenging job. Since SiO_x is non-conductive, the charging effect makes it difficult for the SEM to image at high magnifications with 10 nm or better resolution. Even FESEM (Field Emission SEM, for example the Supra^{TM} 40 vp by Carl Zeiss SMT Inc.), which has a better resolution than the conventional SEM, was found in our experiments to be not quite an adequate tool for the direct determination of the microstructure of PECVD SiO_x. Nevertheless, with FESEM, we are able to obtain some useful information about the surface topography etc., which can be used to indirectly confirm some of the microstructural changes. The details of such an application of FESEM will be given in Sec.6.

In this project, three other characterization techniques were utilized to enhance the previous discussions on property-structure relationships, including FTIR spectroscopy (Fig. 2.9(a)) (Sec.4, San Andrés et al 2000; Del Prado et al 2003), X-ray diffraction (XRD, Fig. 2.9(b)) (Sec.5, Zhu et al 1995; Werwa et al 1994), and Second Ion Mass Spectroscopy (SIMS) (Sec.6, Chen et al 2003).

Other characterization techniques may be useful for the future directions of research on this topic, such as Transmission Electron Microscopy (TEM) (Transmission Electron Microscopy) (Zhu et al 1995; Min et al 1996; Gourbilleau et al 2001; Werwa et al 1994; Inokuma et al 1998; Iacona et al 2000). Particularly, a technique named Energy Filtered Transmission Electron Microscopy (EFTEM) appears to be most promising (Iacona et al 2004).

Recently, it was reported that silicon nanoclusters embedded in SiO_2 was produced by thermal annealing of PECVD SiO_x films, and EFTEM was successfully applied to investigate the structural properties of this system (Iacona et al 2004).

(a)

(b)
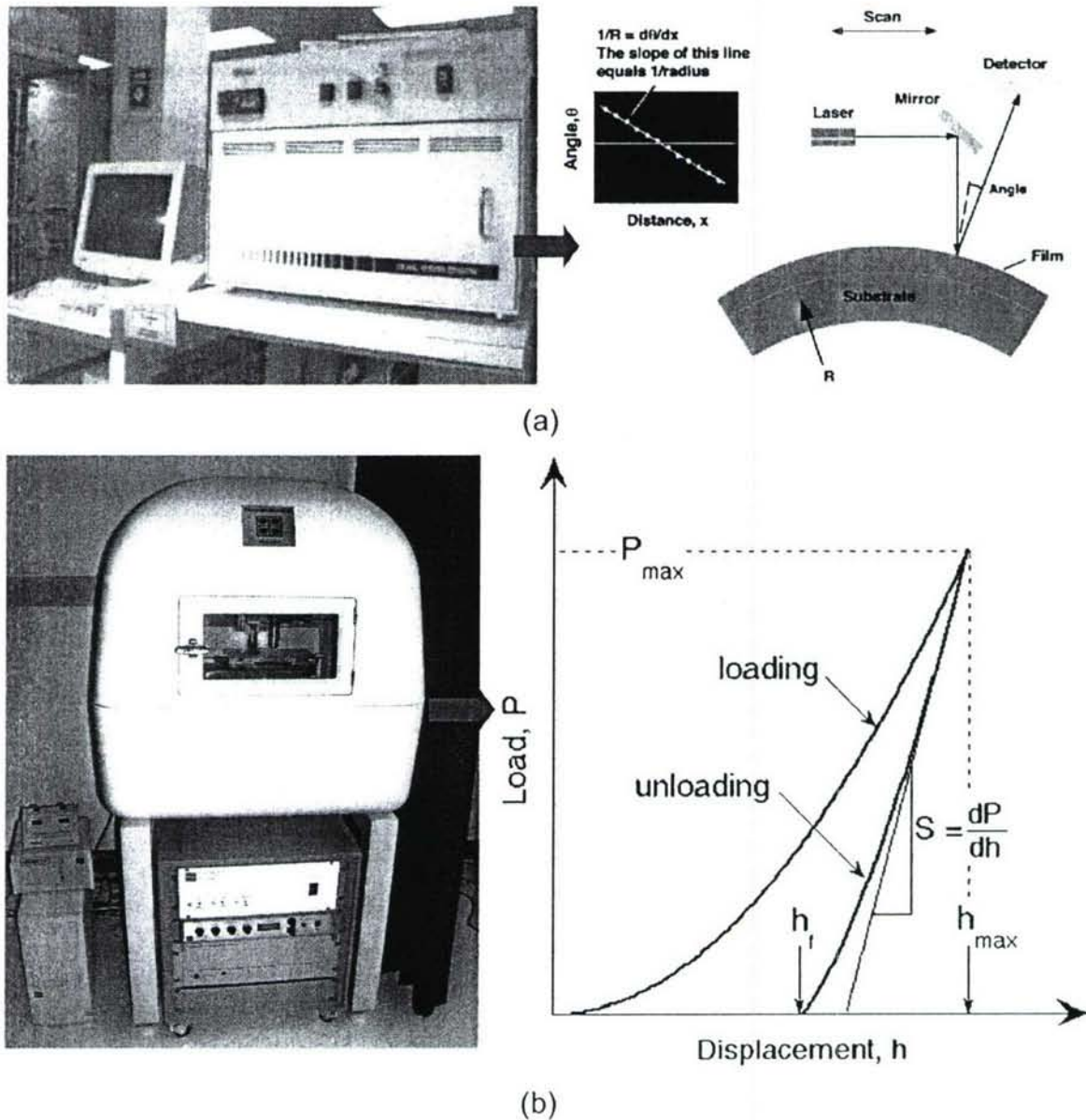
Fig.2.1. (a) The KLA-Tencor[TM] FLX system (Courtesy MTL@ MIT & KLA-Tencor Inc.); (b) Hysitron TriboIndenter[TM] nanoindentation system (Courtesy Prof. Klapperich) and a typical load-displacement curve.

(a)

(b)
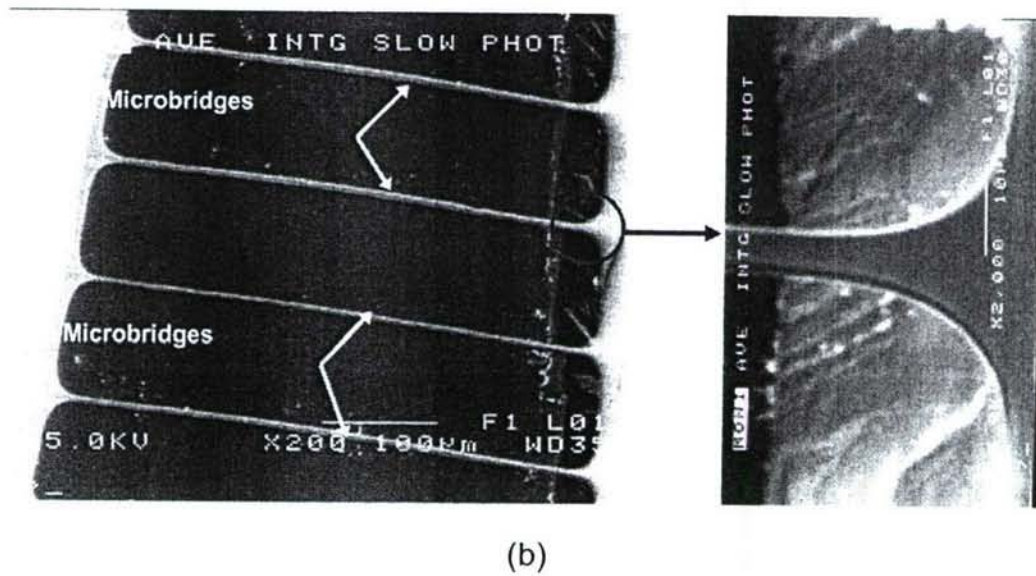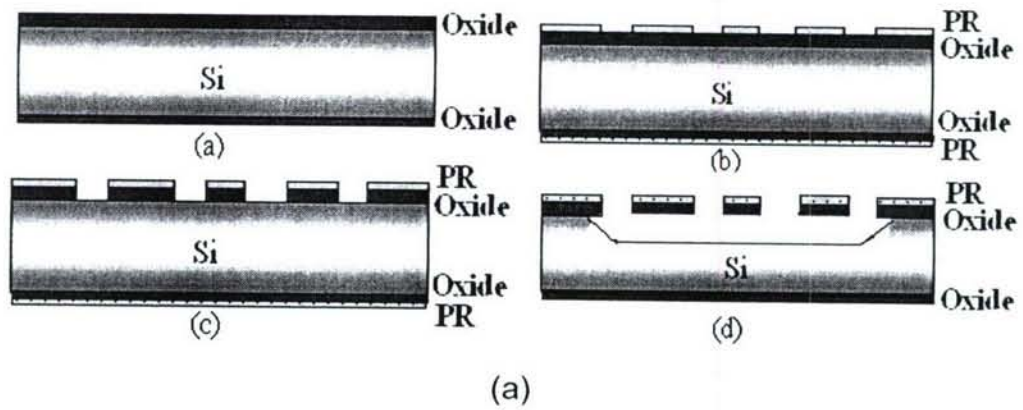
Fig.2.2. (a) Simplifed fabrication process for microbridges. (PR stands for photoresist. Oxide stands for PECVD SiO_x.) (b) SEM showing some fabricated freestanding PECVD SiO_x microbridge arrays.

(a)
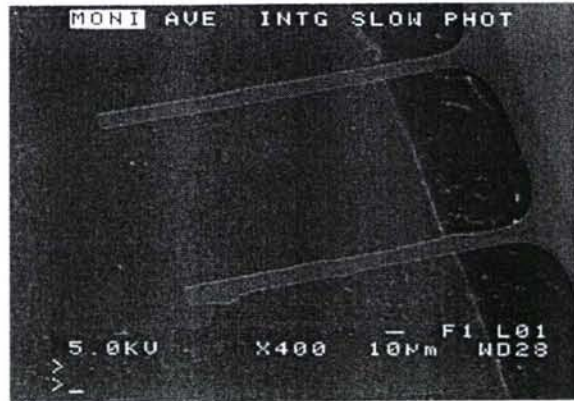
(b)

Fig.2.3. SEM images of various freestanding PECVD SiO$_x$ microcantilver arrays.
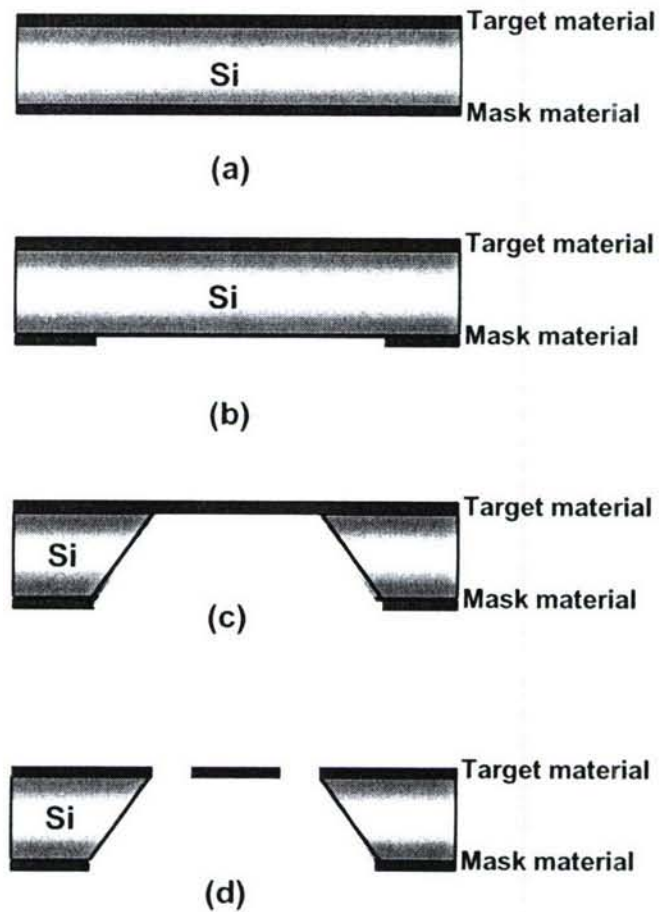
Fig.2.4. Simplified fabrication process flow of the microbridge samples made of gerneral target materials: (a) target thin film deposition on the front side, and mask thin film depostion on the back side; (b) Pattern and etch mask material on the backside; (c) Etch the silicon wafer by KOH or TMAH solution; (d) Pattern and etch the target thin film material on the frontside.
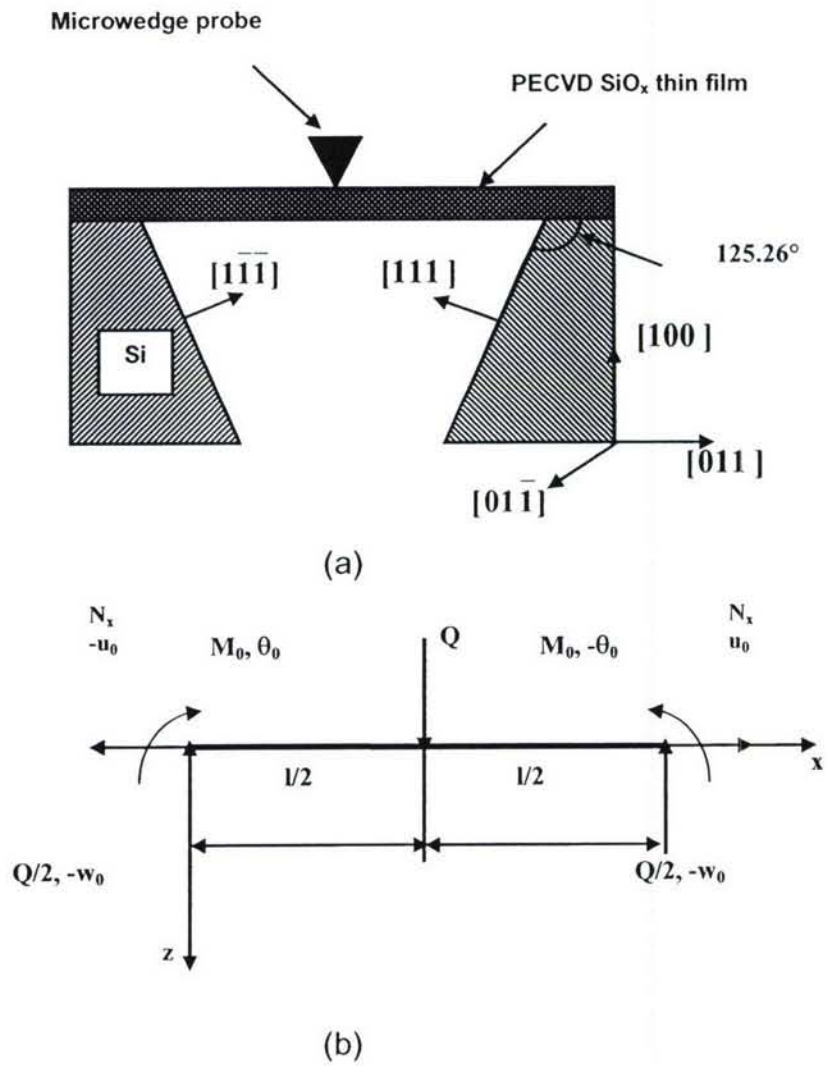
Fig.2.5. (a) Schematic depiction of the microbridge test. (b) Mechanical analysis of beam deflection.
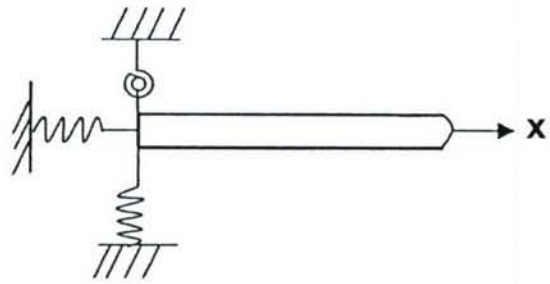
(a)
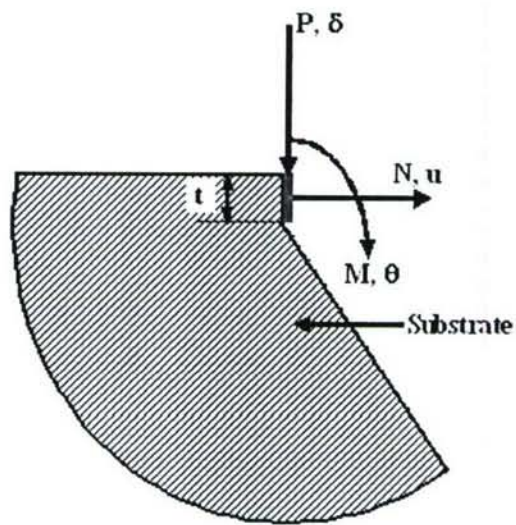
(b)

Fig. 2.6. The deformable substrate model (a) schematic depictions of three springs for a deformable substrate (b) mechanical analysis of the substrate.

Fig.2.7. Schematic of the indentation process with (a) a spherical shaped tip, and (b) a sharp pyramidal tip.

| 200nm | Mag = 23.78 K X | EHT = 2.00 kV | Signal A = SE2 | Signal B = SE2 | ZEISS |
| | WD = 5 mm | Aperture Size = 30.00 μm | Stage at T = 0.4 ° | Date :9 Jan 2006 | |

(a)

| 1μm | Mag = 10.00 K X | EHT = 2.00 kV | Signal A = SE2 | Signal B = SE2 | ZEISS |
| | WD = 4 mm | Aperture Size = 30.00 μm | Stage at T = 0.0 ° | Date :1 Mar 2006 | |
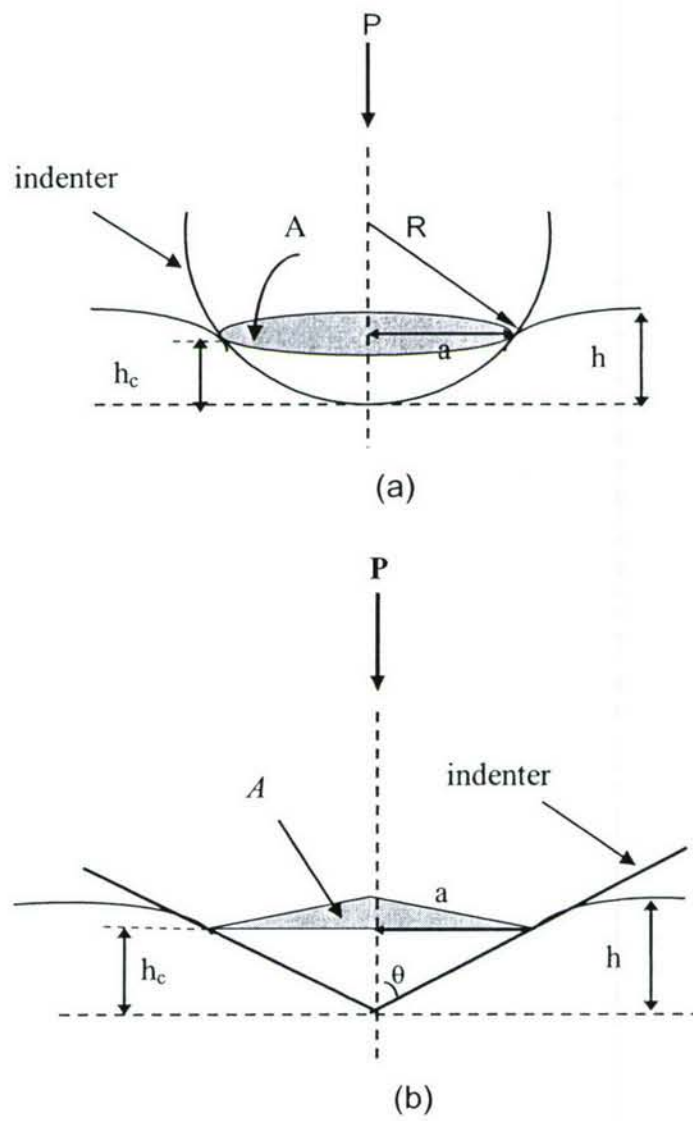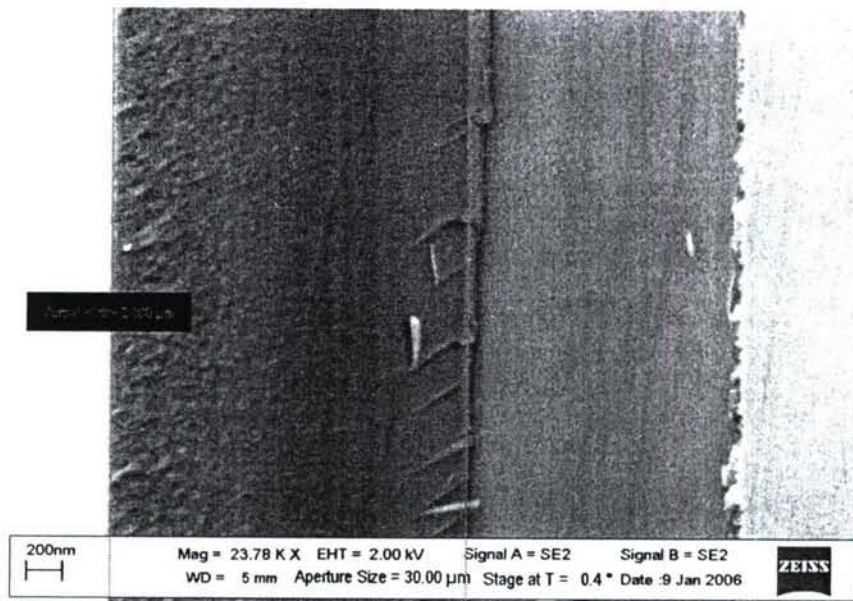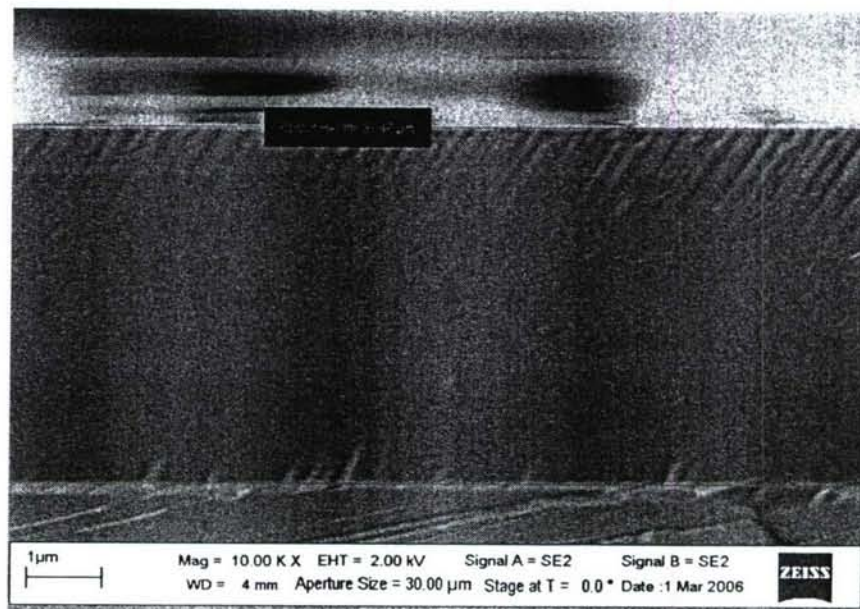
(b)

Fig.2.8. The thicknesses of (a) a 2 μm and (b) a 5 μm PECVD SiO_x film were separately measured by the SEM.
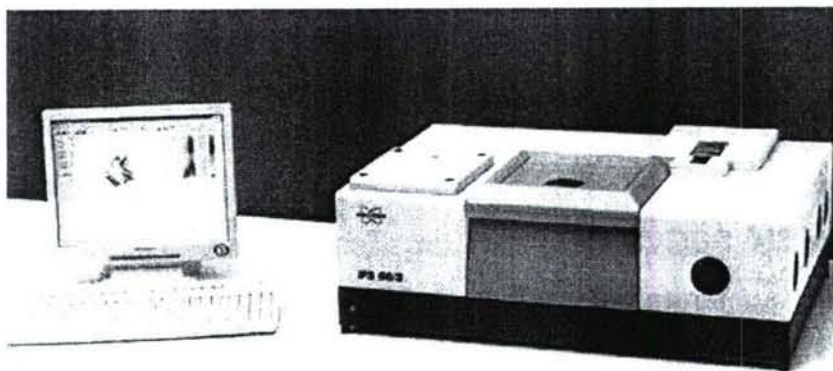
(a)
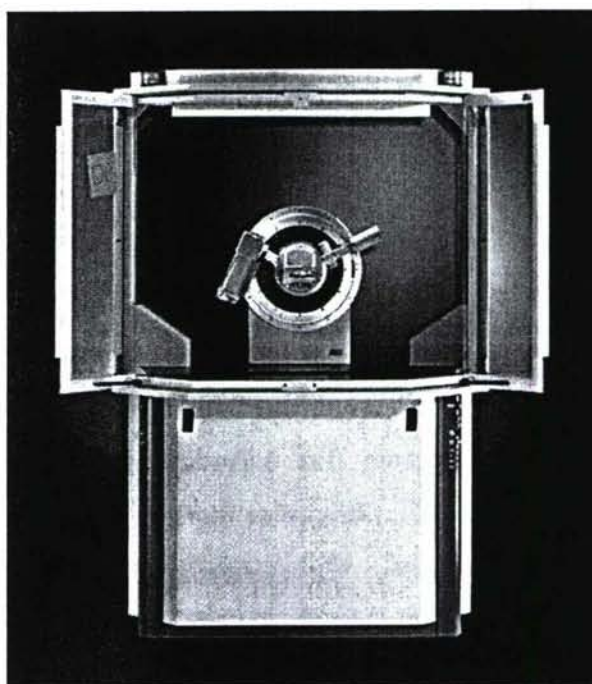
(b)

Fig.2.9. Two materials characterization tools used in this project: (a) IFS 66/s FTIR system (Bruker Inc.); (b) AXS D8 Focus^{TM} XRD system (Bruker Inc.).

3. MICROBRIDGE TESTING

Abstract: In this section, a novel nanoindentation-based microbridge testing method is developed to measure both the residual stresses and Young's modulus of PECVD SiO_x films on silicon wafers. Theoretically, we considered both the substrate deformation and residual stress in the thin film and derived a closed formula of deflection versus load. The formula fitted the experimental curves almost perfectly, from which the residual stresses and Young's modulus of the film were determined. Experimentally, freestanding microbridges made of PECVD SiO_x films were fabricated using the silicon undercut bulk micromachining technique. Some microbridges were subjected to rapid thermal annealing (RTA) at temperatures of 400 °C, 600 °C or 800 °C to simulate the thermal process in the device fabrication. The results showed that the as-deposited PECVD SiO_x films had a residual stress of -155±17 MPa and a Young's modulus of 74.8±3.3 GPa. After the RTA, the Young's modulus remained relatively unchanged at around 75 GPa, however significant residual stress hysteresis was found in all the films. A microstructure-based mechanism was then applied to explain the experimental results of the residual stress changes in the PECVD SiO_x films after the thermal annealing.

3.1. Introduction

As introduced earlier, Microelectromechanical systems (MEMS) refer to devices that have a characteristic length of less than 1 mm but more than 1 µm, that combine electrical and mechanical components and that are fabricated using integrated circuit batch-processing technologies (Gad-el-Hak 2002). The deposition of thin films is one of the most fundamental steps in the MEMS device fabrication (Madou 2002). The deposition process and the post-deposition thermal treatment (referred to as annealing) have a strong influence on both the

residual stress and the material properties of the thin films. Residual stresses in thin films affect the mechanical response of a device constructed by the thin films (Madou 2002), and may cause film cracking, buckling, and delamination (Ohring 1992; Freund and Suresh 2004). The material properties of thin films, such as Young's modulus, are in general different from their bulk counterparts, largely due to the higher surface-to-volume ratios (Ohring 1992; Freund and Suresh 2004). The mechanical properties and residual stresses of thin films are important design parameters. Therefore, the mechanical characterization of thin films is practically significant. However, it is also often academically challenging due to the small dimension of the film thickness. Novel mechanical characterization techniques have been developed to measure both residual stress and the mechanical properties of thin films. Most of them are mainly mechanics-based, such as nanoindentation (Oliver and Pharr 1992; Taylor 1991; Vlassak et al 1997; Baker and Nix 1994; De Boer and Gerberich 1996; Zhang TY et al 1999), uniaxial tensile testing of freestanding films (Mearini et al 1993; Brotzen 1994), micro-cantilever bending (Weihs et al 1988; Najafi and Suzuki 1989; Schweitz 1992; Schull and Spaepen 1996), and bulge testing (Vlassak and Nix 1992; Vinci and Nix 1996; Ziebart et al 1998). Others are mainly based on optical (Sharpe et al 1997; Espinosa 2003), X-ray scattering (Xu et al 2001) and laser-acoustic methods (Hernandez et al 2002) etc. The microbridge testing technique presented in this section is essentially a mechanical method.

The nanoindentation-based microbridge testing method pioneered by Zhang TY *et al* (2000) and further developed in this section has the capability of simultaneously measuring the residual stress, Young's modulus, yield strength, and the stress-strain relation of the thin film materials (Zhang TY et al 2000; Su et al 2000; Xu et al 2003). In this method, freestanding microbridges are fabricated from the thin films using the micromachining techniques (Madou 2002). The tests are performed at the center of the microbridges with an instrumented nanoindentation system and the load-deflection curves are recorded, from which

the mechanical properties of the tested films are extracted. The microbridge testing method will find broad applications in the mechanical characterization of thin films, which are of interest to the microelectronics and MEMS industries. In addition, a microbridge is a fundamental structure in MEMS, which may be applied in the microbridge-based sensors, such as the flow sensors, humidity sensors, and chemical gas sensors etc (Moldovan et al 2000; Matsuura et al 1997).

Plasma-enhanced chemical vapor deposited (PECVD) silane-based silicon oxides (SiO_x) have been widely used in both microelectronics and MEMS to form electrical and/or mechanical components (Madou 2002; Cao and Zhang 2004; Thurn and Cook 2002). In this section, we present both the theoretical analysis and the microbridge testing results of residually compressively stressed PECVD SiO_x films. The general solution to the bending behavior of a microbridge with an initial compressive stress was derived by following Timoshenko and Woinowsky-Krieger's approach (1959), which was qualitatively different from the solution with an initially residual tensile stress (Zhang TY et al 2000). To get more precise solutions, we specifically considered and modeled the substrate deformation with three coupled springs. Additionally, the associated postrelease deflection problem, which is common in micromachined beam-structures, was also addressed theoretically by adding a "fictitious load" (Timoshenko and Woinowsky-Krieger 1959).

We found that this model fit the experimental data almost perfectly. However, if the substrate deformation should be neglected, the theoretical curve would deviate from experimental data noticeably. These results also show that the as-deposited compressive stresses in the 2-μm-thick PECVD SiO_x films deposited at 400 °C were -155±17 MPa. To simulate the post-fabrication thermal process in the device fabrication, these microbridges were also subjected to rapid thermal annealing (RTA) up to 800 °C. After the RTA, significant residual stress hysteresis was observed for all the films. This hysteresis indicated a non-

44

reversible microstructural change, or structural relaxation, during post-fabrication thermal processing. We propose that "seams", bonds that were compressed, were responsible for tensile stress hysteresis generation and "voids", bonds that were stretched, were responsible for compressive stress hysteresis generation (Cao and Zhang 2004). The balancing of these two factors eventually determined the film stress.

3.2. Microbridge Testing Model

3.2.1. Deformation of the beam

Fig. 3.1 is a schematic depiction of the microbridge test, where the microbridge was made of a plasma-enhanced chemical vapor deposited silicon oxide (PECVD SiO$_x$) film and the crystallographic orientation of the silicon substrate was caused by the etching during the sample fabrication.

Following Timoshenko and Woinowsky-Krieger's approach (1959), we consider a beam of length l carrying a single concentrated load Q (force per unit width) at the center of the beam. The middle plane of the plate is chosen as the x, y- plane, the left end (point O) as the origin, and the positive direction of z-axis as to be downward, as shown in Fig. 3.2. The governing equation for the deflection of the beam is given by considering the equilibrium of moments for an element of the beam at x:

$$D\frac{d^2w}{dx^2}-N_x(w-w_0)+\frac{Q}{2}x+M_0=0, \qquad \text{for the left}$$

$$D\frac{d^2w}{dx^2}-N_x(w-w_0)+\frac{Q}{2}(l-x)+M_0=0, \qquad \text{for the right} \qquad \text{(Eq. 3.1)}$$

where w is the displacement in the z-axis, w_0 is the displacement at the two ends (i.e. $x = 0$ and l), $D=E_f t^3/12$ is the flexural rigidity (when neglecting the stress in the film in the y-direction so as to be consistent with the residual stress which is relaxed in the y-direction), t is the beam thickness, E_f is the Young's modulus of

the beam, N_x is the force per unit width in the middle plane of the beam along the length direction, and M_0 is a moment connecting the film and the substrate.

Note that Eq.(3.1) is based on elasticity and the beam theory which requires the deflection of the beam is small compared with the beam length. Eq.(1) is valid regardless of the sign of N_x, where $N_x > 0$ indicates a stretching (tensile) force in the middle plane of the beam along the length direction, and $N_x < 0$ indicates a compressive force in the middle plane of the beam along the length direction. In the case of the PECVD SiO_x films, the as-deposited residual stress in the film is compressive in nature (Sec6, Cao and Zhang 2004; Thurn and Cook 2002), i.e. $N_r < 0$, where N_r is the residual stress per unit width in the film along the length direction. If $N_r < 0$, $N_r < N_x$ will be in general true because the deformation stretches the beam length and generates a positive stretching force. As the deformation becomes severe, the sign of N_x will change from minus to plus. For an initially straight beam under an initial compressive stress, the general solution to Eq. (3.1) is:

$$w = A_l \cos(kx) + B_l \sin(kx) + \frac{Q}{2N_x}x + w_0 + \frac{M_0}{N_x},$$ for the left

$$w = A_r \cos(kx) + B_r \sin(kx) + \frac{Q}{2N_x}(l-x) + w_0 + \frac{M_0}{N_x}, f$$ or the right (Eq. 3.2)

where

$$k = \sqrt{-\frac{N_x}{D}}$$ (Eq. 3.3)

The integration boundary conditions for Eq. (3.2) are: 1) at the two ends (i.e. $x = 0$ and $x = l$), $w = w_0$; 2) at the loading point, the two portions should have the same deflection and a common tangent. These conditions yield:

$$A_l = -\frac{M_0}{N_x}, \quad A_r = -\frac{M_0}{N_x} - \frac{Q}{N_x k}\sin(kl/2)$$ (Eq. 3.4)

$$B_l = -\frac{Q\sin(kl/2)}{N_x k \sin(kl)} - \frac{M_0}{N_x}\frac{1-\cos(kl)}{\sin(kl)}$$

$$B_r = \frac{Q\sin(kl/2)}{N_x k \tan(kl)} - \frac{M_0}{N_x}\frac{1-\cos(kl)}{\sin(kl)} \qquad \text{(Eq. 3.5)}$$

Thus the general solution of Eq. (3.2) can be rewritten as

$$w = -\frac{Q\sin(kl/2)}{N_x k \sin(kl)}\sin(kx) + \frac{Q}{2N_x}x - \frac{M_0}{N_x}\left[\frac{\sin(kx)+\sin[k(l-x)]}{\sin(kl)}-1\right]+w_0, \quad \text{for the left}$$

$$w = -\frac{Q\sin(kl/2)}{N_x k \sin(kl)}\sin[k(l-x)] + \frac{Q}{2N_x}(l-x) - \frac{M_0}{N_x}\left[\frac{\sin(kx)+\sin[k(l-x)]}{\sin(kl)}-1\right]+w_0,$$

$$\text{for the right} \quad \text{(Eq. 3.6)}$$

From this equation, the slope of the deflection of the beam is obtained at the end $x = 0$

$$\theta_0 = \frac{Q[\cos(kl/2)-1]}{2N_x\cos(kl/2)} + \frac{M_0 k}{N_x}\tan(kl/2). \qquad \text{(Eq. 3.7)}$$

For the deformation of the beam in the x direction, we have

$$\frac{l}{2E_f t}(N_x - N_r) = \int_0^{l/2}\left[\frac{\partial u}{\partial x} + \frac{1}{2}(\frac{\partial w}{\partial x})^2\right]dx,$$

or $\qquad u\big|_0^{l/2} = -\frac{1}{2}\int_0^{l/2}(\frac{\partial w}{\partial x})^2 dx + \frac{l(N_x - N_r)}{2E_f t} \qquad$ (Eq. 3.8)

Because the deflection of the beam is symmetric with x = l/2, we have

$$u\big|_{x=l/2} = 0 \qquad \text{(Eq. 3.9)}$$

Then the displacement along the x-axis at the end of x = 0 is obtained

$$u_0 = I - \frac{l(N_x - N_r)}{2E_f t} \qquad \text{(Eq. 3.10a)}$$

where $\qquad I = \frac{1}{2}\int_0^{l/2}(\frac{\partial w}{\partial x})^2 dx \qquad$ (Eq. 3.10b)

The integral *I* above is calculated by substituting Eq. (3.6) into Eq. (3.10b):

$$I = \frac{1}{8k}\left[\left(a^2 + b^2 + 2c^2\right)kl + 8(a-b)c\sin(kl/2) + 2abkl\cos(kl) + \right.$$
$$\left. + \left(a^2 + 2ab - b^2 + 8bc\right)\sin(kl) + b^2\sin(2kl)\right]$$ (Eq. 3.11a)

where

$$a = -\frac{Q\sin(kl/2)}{N_x\sin(kl)} - \frac{M_0 k}{N_x\sin(kl)},$$
$$b = \frac{M_0 k}{N_x\sin(kl)},$$ (Eq. 3.11b)
$$c = \frac{Q}{2N_x}.$$

3.2.2. Deformation of the substrate

Though the deflection of the beam could be large, the base deformation is assumed to be linear and thus it is modeled by three coupled springs, as shown in Fig. 3.3(a). The base action to the beam is simulated by three generalized forces, e.g. two forces N and P along the x-axis and z-axis, respectively, and a moment, M (see Fig. 3.3(b)). The deformation of the film is coupled with the base deformation through the generalized forces and displacements. Thus, the values of N and P are affected by the film properties and geometries. The corresponding three generalized displacements are expressed by u, d, $?$, and the following constitutive equation applies

$$u = S_{NN}N + S_{NP}P + S_{NM}M,$$
$$\delta = S_{PN}N + S_{PP}P + S_{PM}M,$$ (Eq. 3.12)
$$\theta = S_{MN}N + S_{MP}P + S_{MM}M.$$

where S_{ij} are the compliances. As mentioned earlier, the deformation of the substrate is a second order effect and are assumed to be linear, thus the compliances S_{ij} depend only on the base properties (such as its Young's modulus and crystallographic orientation) and geometries (such as the film thickness and supporting angle) and are symmetric (i.e., $S_{NM} = S_{MN}$, etc.) for a given isotropic substrate. Due to our fabrication method, the silicon substrate in

48

this study has a support angle of 125.26°. Also, in the present study, the film thickness is 2 μm. For such a configuration, the compliances S_{ij} are determined by Finite Element Analysis (FEA) and listed in Table 3.1 (Zhang TY et al 2000).

3.2.3. Load-deflection relationship

At the connecting point of the film and the substrate, the displacement continuity and force equilibrium require

$$u = u_0, \delta = w_0, \theta = \theta_0,$$
$$N = N_x - N_r, P = Q/2, M = -M_0. \tag{Eq. 3.13}$$

From Eqs. (3.7), (3.10), and (3.13), we have

$$w_0 = S_{PN}(N_x - N_r) + S_{PP}\frac{Q}{2} - S_{PM}M_0 \tag{Eq. 3.14}$$

$$1 - \frac{l(N_x - N_r)}{2E_f t} = S_{NN}(N_x - N_r) + S_{NP}\frac{Q}{2} - S_{NM}M_0 \tag{Eq. 3.15}$$

$$M_0 = \frac{S_{MN}N_x(N_x - N_r) + \frac{1}{2}S_{MP}QN_x + \frac{1}{2}Q\left[\frac{1}{\cos(kl/2)} - 1\right]}{S_{MM}N_x + k\tan(kl/2)} \tag{Eq. 3.16}$$

Eqs. (3.11), (3.15) and (3.16) form a closed formula and determine the values of N_x and M_0 for a given load, Q, and a given residual force per unit width, N_r. The nonlinear solution of Eq. (3.6) must be simultaneously solved with Eqs. (3.14) - (3.16) and these equations in turn form a closed formula for theoretical deflection vs. load relation. Substituting $x = l/2$ into Eq. (3.6) gives the bridge deflection at the center where the lateral load is applied for built-in ends boundary condition, considering the substrate deformation:

$$w = -\frac{Q\tan(kl/2)}{2N_x k} + \frac{Ql}{4N_x} - \frac{M_0}{N_x}\left[\frac{1}{\cos(kl/2)} - 1\right] + S_{PN}(N_x - N_r) + S_{PP}\frac{Q}{2} - S_{PM}M_0, \tag{Eq. 3.17}$$

If we let all the compliances S_{ij} be zero, it is a straightforward matter to arrive at expressions of the deflection at the beam center for built-in ends boundary condition with a rigid substrate, which has no substrate deformation whatsoever (hereby referred to as the "rigid substrate model" in this section):

$$w = -\frac{Q\tan(kl/2)}{2N_x k} + \frac{Ql}{4N_x} - \frac{M_0}{N_x}\left[\frac{1}{\cos(kl/2)} - 1\right],$$
$$M_0 = \frac{Q[1 - \cos(kl/2)]}{2k\sin(kl/2)}$$

(Eq. 3.18)

3.2.4. Films with postrelease deflections

Different from tensile stress, compressive stress alone may cause microbridges to buckle, if it exceeds the Euler stress limit (Timoshenko and Gere 1961), so that the residual strain energy is partially released. Postrelease deflections are a common phenomenon in MEMS and the possible contributing factors include the residual stress in the film, the fabrication processes, and the "imperfection effects" such as the boundary and beam-geometry asymmetries, etc (Fang et al 1999).

When the initial deflection is small compared with the beam (film) thickness (i.e. $N_x \sim N_r$), we can approximate the initial beam curvature profiles as that produced by an equivalent lateral load (Timoshenko and Woinowsky-Krieger 1959; Tomoshenko and Gere 1961), referred to as the "fictitious load" in this section because its effect is equivalent as a real lateral load but it does not really exist. This so called fictitious load must produce the same deflection as the residual stress produced, so that it will produce an equivalent bending momentum diagram. Then we apply the principle of superposition (Timoshenko and Woinowsky-Krieger 1959) and add the fictitious load to the actual experimental load to obtain the theoretical load-deflection relation curve.

In this work, we give the full mechanical analysis of the deformation of a microbridge with an initial shape of a half sine curve. The outcome of this analysis directly proves that the principle of superposition is applicable for the

solution. If the initial shape of the beam is instead given by a trigonal series, similar analysis procedures can be followed, and it is straightforward to show that the principle of superposition will be still be valid.

In the numerical code, Young's modulus and the residual stress are determined simultaneously by fitting the experimental load-deflection curve using the "least square technique", i.e. minimizing the positive function

$$S = \sum_{i=1}^{n} \left[w_i^e(Q_i) - w_i^t(Q_i, N_r, E_f) \right]^2 \qquad \text{(Eq. 3.19)}$$

where n is the number of data, w_i^e the experimentally observed deflection, and $w_i^t(Q_i, N_r, E_f)$ the theoretical deflection obtained by the above equations. The iteration technique is used to regress the Young's modulus E_f and residual force N_r, which gives the residual stress as $\sigma_r = N_r/t$.

3.3. Experimental Details

3.3.1. Sample fabrication

The PECVD SiO_x films were separately deposited on both sides of a 6 in diameter, 625-μm-thick, n-type <100> silicon wafer at 400 °C at by the conditions specified in Sec.2.2.1. The thickness of the film deposited on the front side was measured by a surface prolifometer (Tencor^{TM} Alpha Stepper 500), and was found to be 2 μm and had a non-uniformity of less than 1%. On the backside, a 1-μm-thick film was deposited to protect the wafer during the bulk etching of silicon. However, if one uses an etching vessel which has a vacuum box for backside protection, this step may be omitted.

Fig. 3.4 shows a simplified process flow for the fabrication of the microbridges. First, the 2 μm PECVD SiO_x film on the front side of the wafer was patterned by the photolithography technique and then etched away by hydrofluoric (HF) acid. Subsequently, the exposed silicon on the front side was

etched in a 5% tetramethyl ammonium hydroxide (TMAH) solution at a temperature of 80 °C to undercut the silicon beneath the PECVD SiO$_x$ so as to release the freestanding microbridges. TMAH was preferred over potassium hydroxide (KOH) to etch silicon because firstly, its selectivity of silicon over silicon oxide is several orders of magnitude higher (Madou 2002; Merlos et al 1992) and secondly, it has a much better undercut ratio (Merlos et al 1992). The thickness of the PECVD SiO$_x$ was measured again after the TMAH etching, and the change in the film thickness was found to be negligible (<0.1%). This silicon-undercutting fabrication approach took advantage of the orientation-dependent silicon etching, and its major benefit was that it required only one photo-mask, thus simplifying the process flow and improving the fabrication yield (Chang et al 1990; Fang 1998).

A fabricated sample of PECVD SiO$_x$ microbridge arrays is shown in Fig. 3.5. The support angle of silicon substrate was 125.26° because of the much slower etch rate in the <111> directions (Madou 2002). Prior to each testing, we measured the curvature profiles of the microbridges with a WYKO™ interferometric microscope, and found that many of the beams had a non-negligible postrelease deflection. In the present study, the microbridge lengths were between 60 and 100 μm and the measured postrelease deflections were less than 2 μm at the center of the beams.

3.3.2. Microbridge test

The microbridge tests were conducted on a Hysitron TriboIndenter™ nanoindentation system equipped with a 20-μm-width wedge tip. Therefore, when the width of the microbridge is less than 20 μm, the mechanical analysis can be simplified to be one-dimensional. Prior to each indentation, both the length and width of each microbridge were precisely measured with the digital coordinates provided by the TriboIndenter™ system, which had a lateral resolution of 0.1 nm. The gap between two adjacent bridges was designed to be

large enough so that each microbridge can be treated as an isolated sample. Each microbridge was carefully aligned to be perfectly perpendicular to either the x, or y axis of the stage of the nanoindenter. All the indentations were performed at the exact geometrical center of the microbridge, with the help of the digital coordinates. The measurement resolution of the nanoindentation load and the vertical displacement were 0.1 μN and 0.1 nm, respectively. The maximum vertical displacement was 5 μm. All of the microbridge tests were conducted at the room temperature, at a loading rate of 100 μN/s and the same rate during unloading. The maximum loads of the experiments were in the order of 1000 μN. Before the microbridge tests, some samples were annealed by RTA for 30 min at 400 °C, 600 °C, or 800 °C.

3.4. Results and Discussion

3.4.1. Validity of the microbridge testing method

In our microbridge testing experiments, at least two indentations were performed on each sample. It was found that the load-deflection curve obtained in the first test often had a noticeable hysteresis between the loading and unloading, which was mainly caused by the change of residual beam-curvature profile from upward to downward. Starting from the second test, however, the hysteresis of load-deflection curve was generally eliminated nearly completely. This indicated an almost completely elastic behavior of the PECVD SiO_x and the silicon substrate under the given loading/unloading rate and the pre-set maximum loads. To further eliminate the effect of any potential plastic deformation, we used the unloading load-deflection curve for fitting to ensure that the elasticity treatment was valid.

Fig.3.6 (a) illustrates a typical load/unload-deflection curve for an 80-μm-long, 16-μm-wide, and 2-μm-thick microbridge made of an un-annealed PECVD SiO_x film. As discussed previously, the fact that the unload-deflection curve

coincided with the load-deflection curve indicated a completely elastic behavior of the PECVD SiO_x film and the silicon base. The maximum loads of all the experiments were in the order of 1000 μN, or 50~100 N/m, yielding a deflection at the order of micron, which was much smaller than the beam lengths, 60~100 μm. The measured postrelease deflections were also smaller than the 2 μm film thickness, indicating that the initial deflections were under small deformation. In this case, the theoretical model developed in Sec. 3.2 can be applied to fit the experimental data.

Using an entire experimental unload-deflection curve and Eqs. (3.15)-(3.17) and (3.19), we simultaneously evaluated both Young's modulus and the residual stress for each specimen. The analytical solution indeed describes the experimental curve nearly perfectly: Fig. 3.6(b) is an example comparison between the experimental data in Fig. 3.6(a) and its theoretical fitting, wherein the residual stress and Young's modulus were determined by the experimental data. For clarity, only the 20th data points are shown in the theoretical curve. If we did not consider the substrate deformation, as in the case of the "rigid substrate model" in Eq. (3.18), the predicted theoretical deflection would be noticeably smaller than that of the deformable substrate model, as shown in Fig. 3.7(a). The normalized deflection difference of the two models with the experimental data is shown in Fig. 3.7(b), in which w_d was the experimental deflection data. Fig. 3.7(b) shows that for both two models, the normalized deflection difference decreased rapidly at the beginning and then slowly as the load increased. Nonetheless, the normalized difference for the deformable substrate model was considerably smaller than that of the rigid substrate model at the same given load. It should be noted that even a small difference in the load-deflection curve would lead to a large deviation in Young's modulus and/or the residual stress. That is why the deformation of the substrate, a much smaller value as compared to the total deflection, should still be taken into account in order to obtain more precise solutions.

For the un-annealed films, a total of 14 microbridge specimens were tested and the results were analyzed in the same way as described previously. The averaged Young's modulus and residual stress with their standard deviations were 74.8±3.3 GPa and -155±17MPa, respectively. It is known that bulk SiO_2 has a Young's modulus of 69 GPa (Thurn and Cook 2002) and SiO_2 (thermal oxide) thin films have a nanoindentation-measured Young's modulus of 64 GPa (Weihs et al 1988). Previously, Young's modulus of a 1-μm-thick PECVD SiO_x film deposited at 250 °C was measured by nanoindentation and the value was 81.5±3.3 GPa (Thurn and Cook 2002). In the present study, we also measured Young's modulus of the un-annealed PECVD SiO_x films by nanoindentation alone and found it to be 76.8±3.4 GPa.

Previous substrate-curvature measurement experiments showed that the as-deposited residual stresses in the PECVD SiO_x films were compressive and varied from -260 MPa to -100 MPa, depending on the deposition parameters and the film thickness (Cao and Zhang 2004; Thurn and Cook 2002). Our evaluated residual stress value of -155±17 MPa were in agreement with the previous wafer-level experiments qualitatively. The variation of the evaluated residual stress might be caused by the non-uniformity of the film thickness, measurement errors of the beam geometries (additionally, the beam area was not perfectly rectangular in reality) and postrelease deflection, the boundary asymmetries, the fabrication processes, and the intrinsic errors of the theoretical model due to simplifications and assumptions.

Although it isn't demonstrated in this section, the microbridge test can also simultaneously extract several other important pieces of information about the thin film materials, along with the residual stress and Young's modulus. For example, it also has the capability to measure the bending strength of the brittle thin films, in which case it is similar to a three-point bending test and the samples are loaded to fracture. Additionally, this method can be potentially applied to study the plastic behavior of the ductile thin films as well.

3.4.2. Effects of high temperature annealing

To simulate the post-fabrication thermal process in the device fabrication, we further tested microbridge samples previously subjected to different RTAs. For each annealing temperature, at least 10 microbridge specimens were tested. The evaluated residual stress and Young's modulus of the 2 μm PECVD SiO_x film as a function of the peak annealing temperature are shown in Fig. 3.8. The data at room temperature (23 °C) represents the as-deposited films for comparison. As we can see, while Young's modulus of the PECVD SiO_x films remained relatively unchanged (~75 GPa), the residual stress of the films (-155±17 MPa after deposition) experienced a significant change in the residual stress (defined here as a stress hysteresis) after the annealing.

Previous substrate-curvature measurement experiments found that the PECVD SiO_x films underwent permanent plastic deformations and also exhibited strong stress hysteresis when thermally cycled at different peak temperatures ranging from 100 to 500°C (Cao and Zhang 2004; Thurn and Cook 2002). We think the cause of the stress hysteresis after thermal annealing of the PECVD SiO_x films was that during annealing, intrinsic stress, or growth stress in the films were partially relieved, accompanied by a non-reversible change in the material microstructure and correspondingly, the thermal-mechanical properties Cao and Zhang 2004). To be more specific, we know that PECVD is a fast deposition process, and the deposition temperature is relatively low (Madou 2002) which means that many atoms are not located at their equilibrium positions where their potential energy is minimized. In other words, there are a lot of bonds that are either distorted or dangling, forming defects. "Seams", here referring to bonds that are compressed, such as hydrogen incorporation and forming of Si-OH...HO bonds, may contribute to the generation of the compressive intrinsic stress. During the annealing at 400 °C, the deposition temperature, the bonds are less distorted and the bond length is increased. As a result, significant reduction in

the compressive stress, or a tensile stress hysteresis is to be expected. Macroscopically, this process is accompanied by a volume expansion, or a density decrease. On the other hand, when the annealing temperature is high enough, another factor comes into play, as "voids", here referring to bonds that are stretched or dangling, may contribute to the tensile stress hysteresis generation. At annealing temperatures higher than 600 °C, the loosely ordered atoms are rearranged in a more orderly structure, and the density of the voids is reduced. As a result, the film stress becomes less tensile, or more compressive. Macroscopically, this process is accompanied by a volume deduction, or a density increase. Equivalently, the deduction of voids also means an increased macroscopic viscosity. It is suggested that both seams and voids are present in the PECVD SiO$_x$ films at any time. At lower annealing temperatures, "seams" are dominant, and as the annealing temperature increases, "voids" will be more dominant. It is the balancing of these two factors that eventually determines the film stress.

3.5. Conclusions

This section proposed a microbridge testing method on elastic thin films deposited on the substrates. Using this method, both the residual stress and Young's modulus of the plasma-enhanced chemical vapor deposited (PECVD) silane-based oxides (SiO$_x$) films were measured simultaneously. Freestanding PECVD SiO$_x$ microbridges were fabricated using the tetramethyl ammonium hydroxide (TMAH) silicon undercutting micromachining technique. The microbridge tests were performed at the beam center and load-deflection curves were obtained. We modeled the substrate deformation as three coupled springs and derived a closed formula of deflection vs. load by solving the governing equation of the beam with initially compressive residual stress. In addition, the non-negligible postrelease deflections of the beam were also taken into account

theoretically by a "fictitious load" method. We found that this model fit the experimental data almost perfectly. However, if the substrate deformation should be neglected, the theoretical curve would deviate from experimental data noticeably.

Our experimental results show that after the rapid thermal annealing (RTA), the Young's modulus remained relatively unchanged at around 75 GPa, which is close to the value measured by nanoindentation on the same film. However, significant stress hysteresis was found in all the films after the RTA. This stress hysteresis indicated a non-reversible microstructural change, or structural relaxation, during annealing.

The microbridge testing method presented in this section has the ability to simultaneously measure Young's modulus, residual stress, yield strength, as well as stress-strain relation of the brittle thin film materials. Potentially, it is capable of studying the plastic behavior of ductile films as well. Since the microbridge samples are fabricated with the micromachining technique, they are easy to handle. We believe that it will find broad applications in the mechanical characterization of thin film materials, which are of interest to both the microelectronics and MEMS industries. In addition, microbridge is a fundamental structure in MEMS and the microbridge test may be a convenient and direct mechanical testing method for microbridge-based sensors.

Table 3.1. Spring compliances S_{ij} for the silicon substrate, with a support angle of 125.26° and a film thickness of 2 μm.

$S_{PN}(m^2/N)$	$S_{PP}(m^2/N)$	$S_{PM}(m/N)$	$S_{MN}(m/N)$	$S_{MM}(1/N)$	$S_{NN}(m^2/N)$
3.62×10^{-12}	2.35×10^{-11}	7.63×10^{-6}	1.13×10^{-6}	1.37×10^{1}	1.65×10^{-11}
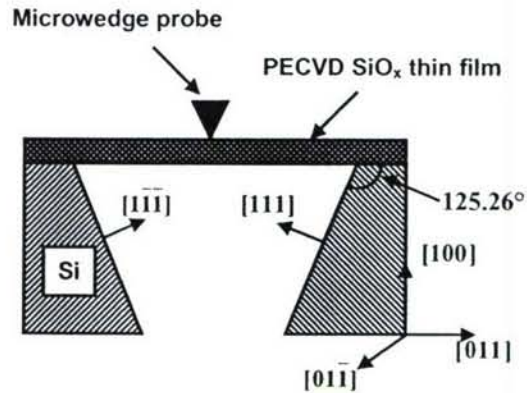
Fig.3.1. Schematic depiction of the microbridge test.
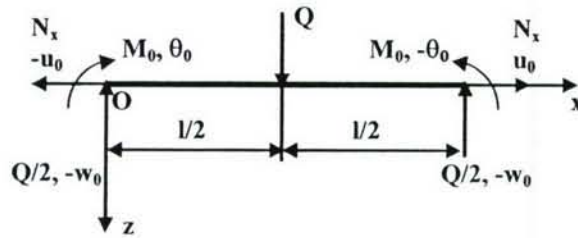
Fig.3.2. Mechanical analysis of the microbridge under a lateral load.

(a)   (b)
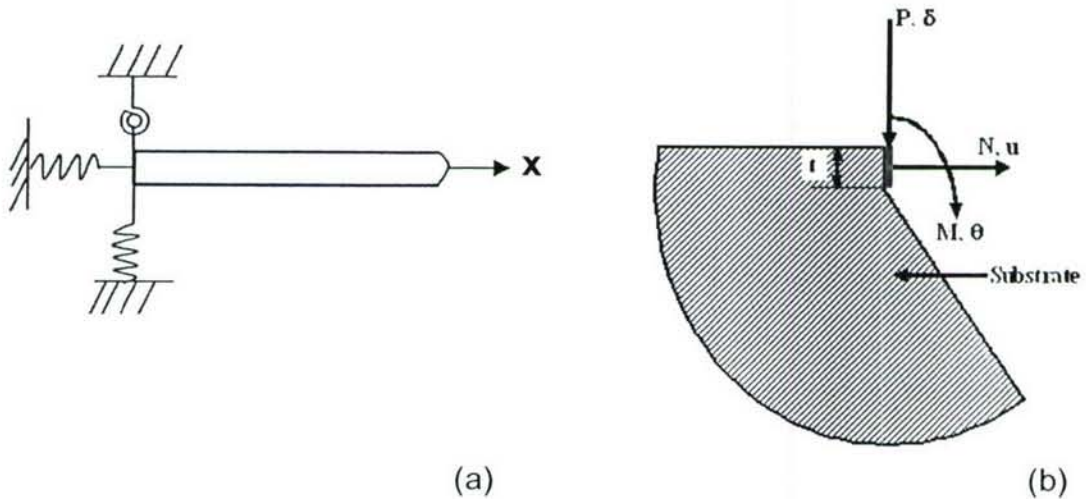
Fig.3.3. The deformable substrate model (a) schematic depictions of three springs for a deformable substrate (b) mechanical analysis of the substrate.

(a)

(b)

(c)

(d)
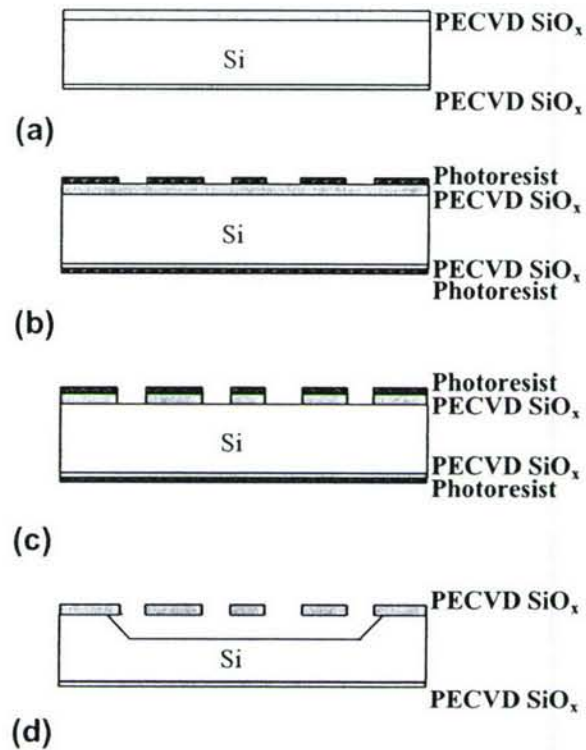
Fig.3.4. Simplified fabrication process flow of the microbridge samples (a) PECVD SiO$_x$ film deposition on both sides (b) Double-side photoresist(PR) coating and front-side patterning by photolithography (c) Hard baking PR and Buffered Oxide Etch (HF) (d) TMAH Anisotropic Wet Etching Si (etch profile is simplified).
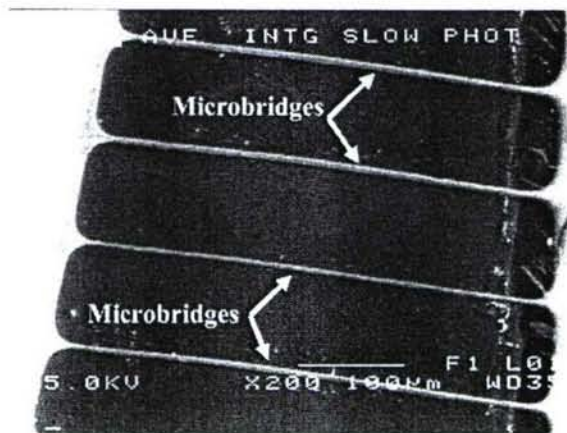
Fig.3.5. Fabricated sample of PECVD SiO$_x$ microbridges arrays with various lengths.
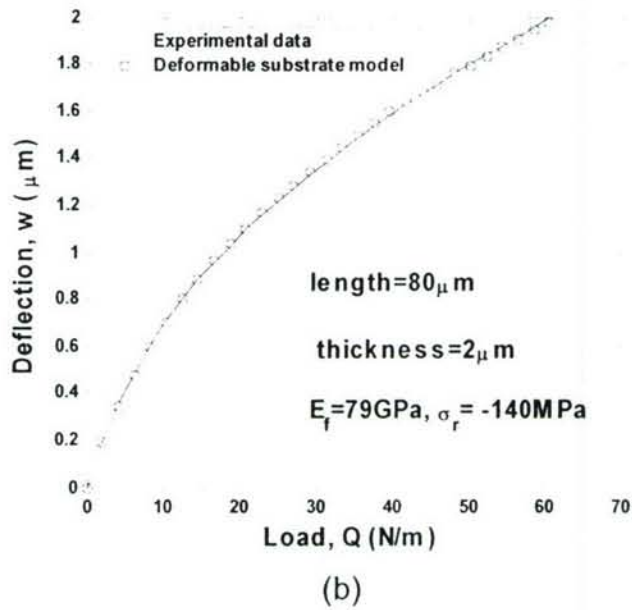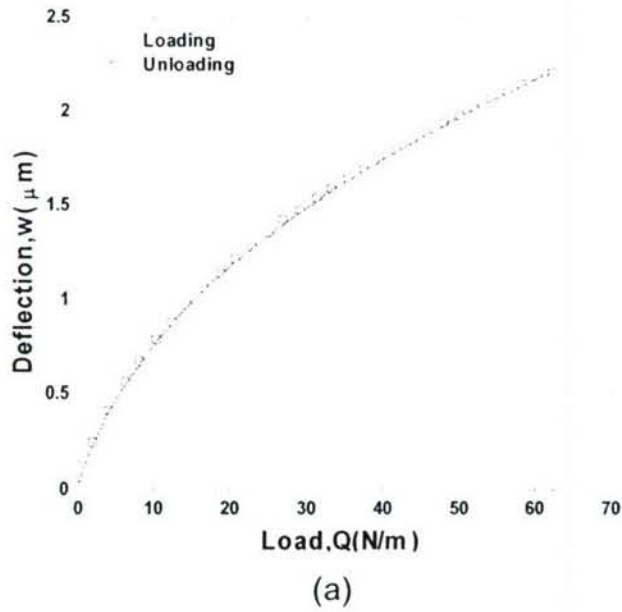
Fig.3.6. (a) A typical loading-unloading curve, for clarity, only the 20th data points are shown in the unloading curve; and (b) Fitting the experimental load-deflection curve with the theoretical model.
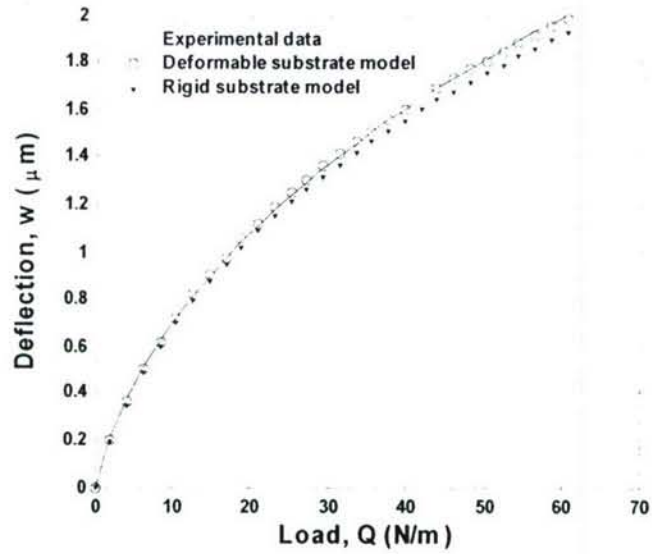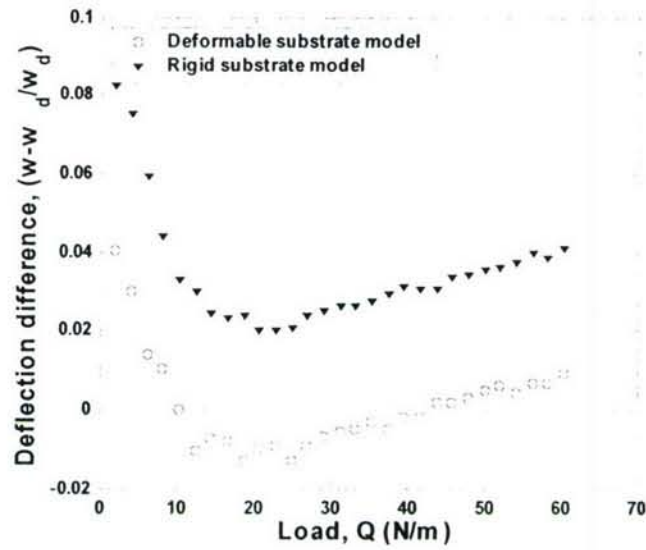
Fig.3.7. (a) Comparison of the beam center deflection with the deformable substrate and the rigid substrate models; (b) Normalized deflection differences of the deformable and rigid substrate model with experimental data.
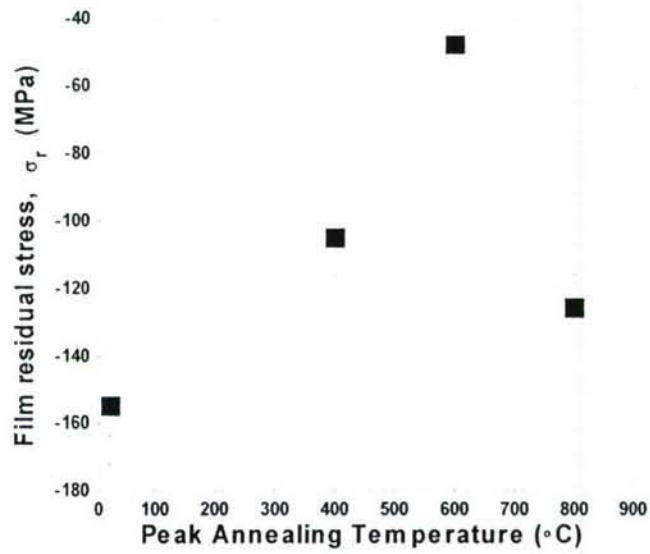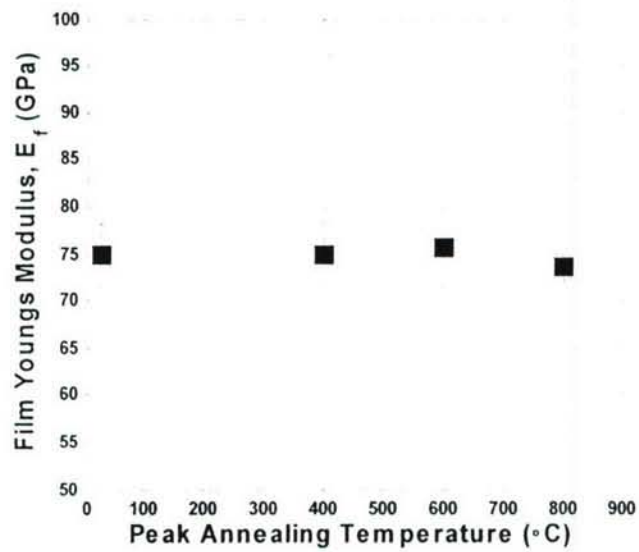
Fig.3.8. The evaluated (a) residual stress and (b) Young's modulus of PECVD SiO_x films as a function of peak annealing temperature.

4. NANOINDENTATION STRESS-STRAIN CURVES

Abstract: In this section, we explore the use of nanoindentation techniques as a method of measuring equivalent stress-strain curves of the PECVD SiO_x thin films. Four indenter tips with different geometries were adopted in our experiments, enabling us to probe the elastic, elasto-plastic, and fully plastic deformation regimes of the PECVD SiO_x thin films. Based on the experimental results, a shear transformation zone (STZ) based amorphous plasticity theory is applied to depict the plastic deformation mechanism in the PECVD SiO_x.

4.1. Introduction

As introduced earlier (Sec.1), in Power MEMS (micro energy-harvesting devices such as micro heat engines and related components) (Epstein and Senturia 1997), PECVD SiO_x serves as the insulation layers, and endures a high level of stress even at low temperatures (Cao and Zhang 2004). Severe plastic deformations often occur in the PECVD SiO_x thin films which cause device degradation or even prohibit the device process integration (Cao and Zhang 2004). So far, however, the plastic properties of the PECVD SiO_x, especially at lower temperatures, are not well understood.

Depth-sensing instrumentation, or nanoindentation, is a popular technique for the estimation of mechanical properties of materials down to nanoscale. The nanoindentation system employs high-resolution sensors and actuators to continuously control and monitor the loads and displacements on an indenter as it is driven into and withdrawn from a material (Pharr 1998). It can reveal a wealth of detailed information about the mechanisms and mechanics of the studied thin film materials, including elastic modulus, hardness, surface adhesion, creep, and stress relaxation behaviors, etc (Pharr 1998; Oliver and Pharr 1992,

64

2004; Lucas and Oliver 1999; Poisl et al 1995; Elmustafa and Stone 2003; Li and Ngan 2004).

In this section, we try to explore the use of nanoindentation as a method of measuring equivalent stress-strain curves of the thin film materials for MEMS applications. As an example, both as-deposited and annealed PECVD SiO_x thin films were tested. The theoretical analysis of nanoindentation strain is based on the previous work of Tabor (1951), Johnson (1970), Hill (1992), Bower et al (1993), Poisl et al (1995) and others (Storåkers and Larsson 1994; Poisl et al 1995), taking into account of indenter tip shape changes during the indentation process. The indentation stress is taken as the instant hardness, or mean pressure underneath the indenter. Most samples will show a varying hardness as load is changed, which is called "indentation size effect (ISE)" on hardness (Nix and Gao 1998; Fleck and Hutchison 2001; Elmustafa and Stone 2003). In addition, the hardness values measured by blunt tips, which have a large elastic component, may deviate from the mostly plastic values at higher forces or when using sharper tips. Therefore, in principle different regimes of elastic-plastic deformation may be probed by the various combinations of indenters and/or indentation loads. In our experiments, four different indenter tips were adopted: 1) conical tip with 5 μm radius; 2) conical tip with 1 μm radius; 3) Berkovich tip with ~150 nm radius; and 4) Cube corner tip with ~50 nm radius. These different indenter tips enable us to study the stress-strain relations of three different deformation regimes of the PECVD SiO_x thin films: 1) elastic, 2) elasto-plastic, and 3) fully plastic.

Based on the knowledge of these nanoindentation load-displacement and stress-strain curves, the plastic deformation mechanism of the PECVD SiO_x is depicted by the shear transformation zone (STZ) based amorphous plasticity theory (Falk and Langer 1998; Langer 2001; Falk et al 2004). The physical origin of the STZ is elucidated and linked with the plastic deformation dynamics.

4.2. Theoretical Background

4.2.1. Measurement of elastic modulus and hardness

Building on the work of many other researchers (Oliver and Pharr 1992), Oliver and Pharr introduced in 1992 a now-classic method for measuring hardness and elastic modulus by nanoindentation techniques. Since then, this method has been widely adopted to characterize the mechanical behavior of materials at small scales, while numerous changes and refinements have been made to further improve its accuracy (Oliver and Pharr 2004). The schematic of a typical nanoindentation load-displacement curve is shown in Fig. 2.1(b). The important parameters are labeled. The basic principle of the Oliver-Pharr method can be summarized as follows:

1)   Take the indentation load-displacement (*P-h*) data obtained during one cycle of loading and unloading. Measure the maximum load, P_{max}, the maximum displacement, h_{max}, and the elastic unloading stiffness (also called the contact stiffness), $S=dP/dh$, defined as the slope of the upper portion of the unloading curve during the initial stages of unloading.

2)   Assuming the "pile-up" at the contact periphery, if any, is negligible, the amount of sink-in is given by:

$$h_s = \varepsilon \frac{P_{max}}{S}$$ (Eq.4.1)

where ε is a constant and approximately $\varepsilon \approx 0.75$. The contact depth, h_c is defined as the depth along which contact is made between the indenter and the specimen, i.e. $h_c = h_{max} - h_s$, or:

$$h_c = h_{max} - \varepsilon \frac{P_{max}}{S}$$ (Eq.4.2)

3)   The key relation among the contact stiffness S, contact area A, and the effective elastic modulus of the material E_{eff} is:

$$S = \beta \frac{2}{\sqrt{\pi}} E_{eff} \sqrt{A} \qquad\qquad (Eq.4.3)$$

In Eq.(4.3), β is a correcting parameter, and $\beta \approx 1$ in the case of small deformation of an elastic material by a blunt conical tip. For sharp triangular indenters, $\beta \approx 1.05$ (Oliver and Pharr 2004). A is the projected area of the indenter at certain contact depth h_c

$$A = F(h_c) \qquad\qquad (Eq.4.4)$$

Finally, E_{eff} is the effective elastic modulus defined by:

$$\frac{1}{E_{eff}} = \frac{1-\upsilon^2}{E} + \frac{1-\upsilon_i^2}{E_i} \qquad\qquad (Eq.4.5)$$

where E and υ are the Young's modulus and Poisson's ratio of the specimen. E_i and υ_i are the Young's modulus and Poisson's ratio of the indenter. For diamond indenter tips that are typically used, $E_i = 1140$ GPa, and $\upsilon_i = 0.07$.

From Eq.(4.3), knowing two of the quantities S, A, and E_{eff} will enable us to derive the third one. In practice, S is measured by first fitting the upper portion of unloading curve with a power law relation $P = \alpha (h-h_f)^m$, where α and m are fitting constants, and h_f is the measured final or permanent depth of penetration after the indenter is fully unloaded. The area function $A = F(h_c)$ is calibrated by a standard material such as the fused quartz, whose $E = 72$ GPa, $v = 0.170$, and $E_{eff} = 69.6$ GPa. Subsequently, E_{eff} can be easily calculated by rearranging Eq.(4.3).

4)   The hardness of the specimen, H, is simply estimated from:

$$H = \frac{P_{max}}{A} \qquad\qquad (Eq.4.6)$$

4.2.2. Nanoindentation stress-strain curves

The stresses generated in an indentation test include compressive, tensile, and shear stresses in all the directions. However, it is found that most of the material underneath the indenter is subjected to a constant level of equivalent

67

stress (Bower et al 1993), approximated by the mean pressure that can be sustained under the indentation load.

For each specimen, the relation $h_c = f(h)$ between contact depth (h_c) and the measured instant maximum depth (h) can be calibrated before the experiments through Eq.(4.2). Knowing $h_c = f(h)$ and the area function of the nanoindenter tip $A = F(h_c)$, it is possible to evaluate also the instant hardness H in a creep process following $H=P/A$. Note that H also signifies the mean pressure, or the average stress $\overline{\sigma}$, that can be sustained under the indentation load (Freund and Suresh 2004), i.e.:

$$\overline{\sigma} = \frac{P}{A} \tag{Eq.4.7}$$

The stresses generated in an indentation test include compressive, tensile, and shear stresses in all the directions. Nevertheless, it is found that most of the material underneath the indenter is subjected to a constant level of equivalent stress, approximated by the mean pressure that can be sustained under the indentation load (Bower et al 1993). In other words, we can also define a single representative or "equivalent stress" (Eq.4.7) during the indentation process.

The determination of an equivalent indentation strain is more complicated. A schematic of a nanoindentation test with a spherical shaped tip and a sharp trigonal pyramid tip is illustrated in Fig.4.1 (a) and (b). In Fig.4.1 (a), a represents the contact radius, defined by

$$a = \sqrt{\frac{A}{\pi}} \approx 0.5642\sqrt{A} \tag{Eq.4.8a}$$

where A is the tip area function defined previously in Eq.(4.4). In Fig.4.1 (b), a is the contact semi-width. Given that the projected area is an equilateral triangle, we can easily derive:

$$a = 2\sqrt{\frac{A}{3\sqrt{3}}} \approx 0.8774\sqrt{A} \tag{Eq.4.8b}$$

At very small depth, even the shapes of the conical and pyramidal tips (collectively called geometrically self-similar tips) are rounded, thus only Eq.(4.8a) applies. If we assume that the blunt tip profile is approximately circular with radius R, the maximum contact depth, δ_0, below which the indent shape is spherical can be estimated by the Eq. (Li and Ngan 2004):

$$\delta_0 = R(1 - \sin\theta) \qquad \text{(Eq.4.9)}$$

where θ is the semiangle of the indenter tip. Johnson's (1970) contact mechanics analysis of the indentation process shows that for geometrically self-similar tips, the equivalent indentation strains at shallow depth can be estimated by:

$$\varepsilon_I = K\frac{h_c}{a} \qquad \text{(Eq.4.10)}$$

where K is a constant, and can be determined by indenting a standard sample material with known Young's modulus (see Sec. 4.4 for details). From the similarity of triangles it is straightforward to derive another expression of a, as:

$$a = \sqrt{2Rh_c - h_c^2} \approx \sqrt{2Rh_c}\ (2R >> h_c) \qquad \text{(Eq.4.11)}$$

Eq.(4.11) gives $h_c \tilde{\ } a^2/2R$ at shallow indentation depth of blunted tips. In such cases, Eq.(4.10) also matches the ratio a/R, a widely adopted definition of indentation strain for spherical tips (Tabor 1951).

In this project, the indentation strain ε_I is adopted as Eq.(4.10) only when a/R is small (e.g. $h_c < \delta_0$ for blunt Conical tips). This is because in the case of sharp self-similar indentation of the pyramidal Berkovich and Cube Corner tips, where a/R is typically much higher, Eq.(4.10) may no longer be applicable. Instead, when $h_c > \delta_0$ we turn to the expressions of indentation strain rate $\dot{\varepsilon}_I$ for sharp self-similar indentation, which has been validated by a number of researchers (Poisl et al 1995; Hill 1992; Bower et al 1993; Storåkers and Larsson 1994) through both rigorous theoretical modeling and experiments. In the next section (Sec.5), we will have a more detailed discussion on the equivalent

indentation strain rate. Here, without going into the details, we simply give the form of expression for $\dot{\varepsilon}_I$:

$$\dot{\varepsilon}_I = \frac{1}{h}\frac{dh}{dt} \qquad \text{(Eq.4.12a)}$$

In our experiments, we find that the relation $h_c = f(h)$ is approximately linear for sharp indenters such as the Berkovich and Cube Corner tips. Thus Eq.(4.12a) is rewritten as:

$$\dot{\varepsilon}_I \approx \frac{1}{h_c}\frac{dh_c}{dt} \qquad \text{(Eq.4.12b)}$$

Integration of Eq.(4.12b) yields:

$$\varepsilon_I \approx \log(\frac{h_c}{\delta_0}) + K\frac{\delta_0}{\sqrt{\frac{A(\delta_0)}{\pi}}} \quad (h_c \geq \delta_0) \qquad \text{(Eq.4.13)}$$

A full nanoindentation stress-strain curve can now be obtained by combining Eq.s (7), (10) (for $h_c < \delta_0$), and (13) (for $h_c \geq \delta_0$, if needed).

4.3. Experimental Details

4.3.1. Specimen preparation

A 2μm-thick, silane-based PECVD SiO_x film was deposited on silicon wafers using the conditions specified in Sec.2.2.1. The wafer was subsequently diced into approximately 10 mm × 10 mm squares as specimen for nanoindentation. Before testing, some samples were annealed in an RTP-600S rapid thermal annealing (RTA) system (from Modular Process Technology Corp., San Jose, CA) for 10 min at 800°C in a nitrogen environment. All the references of the "annealed film" in the rest of the section refer to the PECVD SiO_x films that were treated by RTA described above.

Both as-deposited and annealed films were characterized by means of FTIR spectroscopy with an IFS 66/s spectrometer (Bruker Inc., Madison, WI) working in the transmission mode at normal incidence.

4.3.2. Nanoindentation tests

The nanoindentation tests were conducted at room temperature on a TriboIndenter^{TM} system (from Hysitron Inc., Minneapolis, MN). The vertical load resolution of the nanoindentation system is 1 nN, with a noise floor of 100 nN, and the vertical displacement resolution is 0.04 nm, with a noise floor of 0.2 nm. As mentioned in the introduction, four different indenter tips were used: 1) conical tip with 5 μm radius and a semi-angle $\theta = 30°$; 2) conical tip with 1 μm radius and same semi-angle $\theta = 30°$; 3) Berkovich tip with approximately 150 nm radius, a total included angle of 142.3°, and a semi-angle $\theta = 65.35°$; and 4) Cube corner tip with approximately 50 nm radius, a total included angle of 90°, and a semi-angle $\theta = 35.3°$). Both the machine compliance and the tip area functions were carefully calibrated on a standard fused quartz sample (also from Hysitron Inc.), following the procedure proposed by Oliver and Pharr (1992, 2004). Separate area functions were calibrated for different ranges of loads to ensure good fits at all depths.

Constant rate of loading (CRL) tests were performed on both the PECVD SiO$_x$ thin film samples and the standard fused quartz sample in load-control mode, using constant loading rates and the same rate during unloading. A wide range of loads and loading rates were covered. The maximum loads (P_{max}) ranged from 10s of μN to 1000s of μN. The loading rates ranged from 10s of μN/s to 1000s of μN/s.

In all the experiments, the maximum indentation depth was kept below 300 nm, or 15% of the PECVD SiO$_x$ film thickness (2 μm). This was to avoid any influence of the substrate effects to the results (Bhattacharya and Nix 1988).

Whenever possible, scanning probe microscopy (SPM) was performed

after each indent by using the indenter itself as an imaging tip. For example, Fig.4.2(a) and (b) illustrate a 3D topography and a line profile of an indent made on the fused quartz sample, obtained by a Cube Corner tip (the sharpest of the four tips used). Such images generally show that the "pile-up" was negligible during the indentation process, and thus the assumption of the theoretical analysis in Sec. 4.2 is met. Consequently we analyzed the nanoindentation *P-h* data using the equations developed in the previous section, and the results are presented next.

4.4. Experimental Results

4.4.1. *General features of the P-h curves*

Before moving on to the nanoindentation stress-strain curves, we shall describe some qualitative differences of the load vs. displacement (*P-h*) curves obtained by tips with different radii. First, as expected, with sharper indenter tip radii, it usually leads to a more pronounced plastic deformation under the same loading conditions. Additionally, the plastic responses of the sample are more sensitive to loading rate when the tip is sharper. To illustrate these points, typical nanoindentation results on the as-deposited PECVD SiO_x are shown in Fig.4.3 (a) and 3(b) for two of the nanoindenter tip radii, 150 nm (Berkovich) and 5 μm (Conical). It can be further observed from Fig.4.3 that as the loading rate decreases, the curves appear to shift toward larger total displacements. Since the projected tip area increases with depth, the sample appears to be "softer" at lower loading rates.

The rate-sensitive plastic response of the PECVD SiO_x is clearly different from a lot of metallic glasses, which exhibit many distinct displacement bursts during the loading portion of their *P-h* curves at low loading rates (Schuh and Nieh 2004). This "pop-in" effect is analogous to the "serrated flow" observed in compression tests, and was lined to the discrete events of isolated shear banding

(Schuh and Nieh 2004). In Fig.4.3, a wide range of loading rates is covered. The *P-h* curves exhibit no distinct displacement bursts. This may suggest a qualitatively different plastic flow behavior in the PECVD SiO_x thin film.

Next, we will present the nanoindentation stress-strain curves obtained by four different indenter tips, covering the elastic, elasto-plastic, and fully plastic regimes of deformation. The loading and unloading time was both only 5s in all the example cases. Due to the relatively short loading/unloading time, it is believed that the effect of time-dependent processes is minimal, and the differences indicate an elastic-plastic rate-independent response of the material, which will be the focus of our investigation.

4.4.2. Elastic regime

To establish its validity, we first obtain the indentation stress-strain curves of the standard fused quartz, which is amorphous silica in microstructure and has a known Young's modulus of 72 GPa. When using the bluntest of our tips, i.e., the 5 µm conical tip, we found that the indentation load-displacement (*P-h*) curve, shown in Fig.4.4 (a), represents an almost completely elastic response at loads up to the mNs. Its corresponding indentation stress-strain ($\overline{\sigma}$ -ε_l) curve is shown in Fig.4.4 (b), which is almost completely linear and no plastic yielding is evident. If we assume $K=1$ in Eq.(4.10), a slope of 76 GPa can be obtained, which is within 10% of range of error of 72GPa. By keeping the same K value, we further calculated the nanoindentation stress-strain curves when indenting the PECVD SiO_x thin films (both as-deposited and annealed) with the 5 µm conical tip, and the results are presented in Figs. 4.5 and 4.6. It can be observed for both samples that under the same loading conditions, the final (plastic) depth h_f is non-zero, indicating that small plastic deformation occurred during the indentation process. However, their nanoindentation stress-strain curves still remain relatively linear, confirming that the amount of plastic deformation was minimal.

4.4.3. Elasto-plastic regime

From Figs. 4.4-4.6 in Sec. 4.4.2, it can be inferred that sharper tips have to be employed to better probe the elasto-plastic regime of the deformation. In our experiments, a 1 μm conical tip was used for this purpose. The nanoindentation load-displacement and stress-strain curves of the fused quartz sample are shown in Fig.4.7. It can be seen in Fig.4.7 (b) that the plastic yielding occurs at around 5 GPa in the fused quartz. We denote this point by the parameter σ_I, or the initial yielding point. For $\bar{\sigma} < \sigma_I$, the deformation is almost completely elastic. As $\bar{\sigma}$ exceeds σ_I, there begins to have significant plastic deformation beneath the indenter, but it is still constrained by the elastic surroundings. Therefore, this regime is termed the "elasto-plastic" deformations. The same regime is also identified for the as-deposited and annealed PECVD SiO_x thin films, whose representative results are shown in Figs 4.8 and 4.9, respectively. The initial yielding point σ_I for the as-deposited film is ~3.5 GPa, and for the annealed film, it is ~4.5 GPa, both slightly lower than that of the fused quartz. Correspondingly, their P-h curves also exhibited enhanced plastic deformations (i.e. increased h_f), as shown in Figs. 4.8(a) and 4.9(a).

4.4.4. Fully plastic regime

Finally, fully plastic deformation is achieved when the plastic region beneath the indenter extends to the surface of the sample (Martínez et al 2003). For example, the P-h and $\bar{\sigma}$-ε_I curves of a nanoindentation test with a Berkovich tip on the fused quartz are shown in Fig.4.10. It can be seen that the indentation stress $\bar{\sigma}$ is increases very slowly with increasing h_c after a certain point. We denote the point where the flow becomes fully plastic parameter σ_{II}, or the stationary yielding point (Martínez et al 2003). For the fused quartz, σ_{II} is approximately 9 GPa, corresponding to its hardness value. The initial yielding

point, σ_I cannot be clearly distinguished in Fig.4.10 (b) because the fully plastic flow develops early in the loading stage. If we define a constant C as the ratio between σ_{II} and σ_I, i.e. $\sigma_{II} = C\sigma_I$, the elasto-plastic regime in Sec. 4.4.3 falls into $\sigma_I < \bar{\sigma} < C\sigma_I$. Tabor reported $C=3$ for metals (Tabor 1951). In the case of the fused quartz, we found it to be close to 2, which is reasonable considering a lower E/H value makes the fused quartz not as easy to yield as typical metals. Similar experimental results of nanoindentation P-h and $\bar{\sigma}$-ε_I curves of the PECVD SiO$_x$ thin films when using the Berkovich tip are shown in Figs 4.11 and 4.12, respectively. These figures also clearly identify a fully plastic regime in both the as-deposited and annealed PECVD SiO$_x$ thin films. The stationary yielding point σ_{II} for the as-deposited film is close to 6 GPa, much lower than that of the annealed film, which is approximately 10 GPa. Furthermore, the nanoindentation stress-strain curves Figs. 4.11(b) and 4.12(b) have slopes that are flatter at their largest strains compared with that in Fig.4.10 (b).

It is well known that in the tensile testing, the engineering stress-strain curves often plunges after peaking (Courtney 2000). This is due to the development of a necking instability, and is considered a precursor of ductile fracture (Courtney 2000). In our nanoindentation experiments, we have also tried to probe whether and how the fully plastic regime of our sample materials will develop such instability, by employing the Cube corner tip, the sharpest of the four tips used. Representative results of the P-h and $\bar{\sigma}$-ε_I curves of the fused quartz, as-deposited and annealed PECVD SiO$_x$ thin films using the Cube corner tip are separately shown in Figs. 4.13-4.15. We can see the $\bar{\sigma}$-ε_I curves of all the three sample materials have shown signs of a decreasing slope at the largest strains. Drucker (1952) first proposed that when the work increment required for a fixed increment of plastic deformation begins to decrease, this must signify a change of the nature of the plastic flow from being homogenous to being inhomogeneous. From Figs. 4.13(b), 4.14(b) and 4.15(b), it is apparent

that the inhomogeneous plastic flow occurs earliest in the as-deposited PECVD SiO_x, then the fused quartz, and last in the annealed PECVD SiO_x.

In order to better understand the plastic deformation mechanism of the PECVD SiO_x, in the next section, we will invoke a "shear transformation zone (STZ)" based amorphous plasticity theory to interpret the above experimental results.

4.5. Discussion

4.5.1. Amorphous plasticity theories: An overview

Due to their fabrication methods, both the PECVD SiO_x and fused quartz are known to be amorphous in microstructure. Generally speaking, in amorphous solids, the physical processes of plastic deformation differ substantially from those of the crystalline, polycrystalline, and nanocrystalline materials. In this case, clearly identifiable defects, such as dislocation and grain boundary (GB), cease to provide a useful description of the microstructural dynamics (Falk et al 2004). In the most widely accepted theory of amorphous plasticity, Spaepen (1977), Argon (1979), and others postulate that the basic deformation mechanism in an amorphous solid is a local atomic-scale redistribution of "free volume", which is defined as (V_a-V_c), where V_a and V_c are the respective specific volumes of the amorphous and crystalline phases. At high temperature and low stress, the plastic flow is homogeneous and Newtonian viscous, i.e., the strain rate is related linearly to the applied stress. At low temperature and high stress, the flow is heterogeneous and plastic deformation occurs at localized sites (called flow defects) in the form of "shear bands" (Spaepen 1977; Argon 1979). Falk, Langer and others (Falk and Langer 1998; Langer 2001; Falk et al 2004) have further built on such "free volume" models and proposed that the deformation is mediated by the activation of the rearrangement of a particularly oriented cluster of atoms, known as shear

transformation zones (STZ). The potential causes of localization include softening due to STZ proliferation and elastic interactions between STZs (Falk et al 2004).

4.5.2. Physical origin of STZ clusters in PECVD SiO$_x$

The PECVD SiO$_x$ thin films were deposited at a fast rate (~1 μm/min), at relatively low temperature (~400°C), and with the facilitation of the RF plasma. Due to such fabrication conditions, a lot of the atoms are not in the positions where their potential energy is minimized. As a result, a large density of the Si-O bonds is either distorted (i.e. compressed or stretched) or dangling (such as – SiO$_3$ bonds), forming defects. In addition, our previous SIMS (Second Ion Mass Spectroscopy) analysis found that there was a significant hydrogen concentration near the free surface of the film (~ 6.7%), which decreased to ~ 2% at about 500 nm from the free surface (Cao and Zhang 2004). Due to the RF plasma environment, the incorporated hydrogen atom is likely to be ionized and enters into the Si-O network. Fig.4.16 shows the FTIR spectra of the as-deposited and annealed PECVD SiO$_x$ thin films. Si-O-H bonds, associated with a peak at around 3500 cm^{-1} (Domínguez et al 2003), were clearly present in both films. After RTA however, the peak was slightly reduced, indicating a reduction in the Si-O-H bonding. Si-H bonds, whose peaks are at around 2100-2200 cm^{-1}, were much less dominant compared with Si-O-H bonds. Other identifiable main features in Fig.4.16 include: 1) Si-O (bending mode), at around 810 cm^{-1} (San Andrés et al 2002); 2) Si-O (stretching mode), at around 1100 cm^{-1} with a "shoulder" (San Andrés et al 2002); and 3) H-O-H (water), at around 1600 cm^{-1} (Domínguez et al 2003).

Therefore, according to the FTIR spectra, the STZ clusters in the PECVD SiO$_x$ films should be mainly comprised of a combination of either the fundamental Si-O units or the Si-OH units, as illustrated in Fig.4.17. The bonding among the

STZ clusters may be either shorter than the normal length (i.e. compressed) or longer than the normal length (i.e. stretched or even broken).

During the nanoindentation process, a high level of stress is applied to the Si-O and Si-OH based STZs. This applied stress will cause the proliferations and interactions among the STZ clusters. Shuffling within a STZ is also possible, but given the relatively strong covalent bonds between atoms its effect expected to be much less compared with metallic glasses. The proliferations and the interactions among the STZs will result in a permanent rearrangement of the STZ clusters, and consequently the plastic deformation in PECVD SiO_x films.

4.5.3. Character of plastic flow in PECVD SiO_x

In the conventional STZ theory, as the applied stress exceeds the yield stress, the movement of a first STZ will cause a local dilatation, or expansion of the nearby free volumes (Argon 1979). This, in turn, creates localized distortions of neighboring STZs, and triggers the autocatalytic formation of large bands of STZs, commonly called "shear bands" (Langer 2001; Falk et al 2004). If a single band can rapidly accommodate the applied strain, it will lead to a "strain burst", which is measurable (i.e. as "pop-in" bursts in *P-h* curves) if the resolution of the instrument is high enough (Schuh and Nieh 2004). However, as shown in Fig.4.3 and various other nanoindentation *P-h* curves, no distinct "pop-in" displacement bursts are observed for the loading rates ranging from 10 s to 1000 s of μN/s. This may imply a more homogeneous deformation mechanism. The nanoindentation stress-strain curves in Sec. 4.4 also indicate that the inhomogeneous plastic flow sets in only at late stages of fully plastic deformation regime.

One possible explanation for these results is that, in the early stages of plastic deformation, instead of a single large shear band that can accommodate the applied strain, numerous smaller shear bands could be formed simultaneously every instant at different locations. Given the relatively short

distance of propagation in the thickness direction (the direction of applied load) of the thin film, these shear bands may quickly overlap with each other before any single band relaxes. This will form a field of continuous shear bands, thus resulting in a more homogeneous flow behavior than the heterogeneous plastic flow caused by the discrete shear bands in many metallic glasses (Schuh and Nieh 2004). However, if the applied strain continues to increase, the rapid dynamic formation and relaxation of the STZ clusters will result in a local "softening" of the material. Thus the amount of plastic work needed for a fixed increment of plastic deformation will decrease, which means the stress may drop even if the plastic strain continues to increase. From this point on, the flow becomes unstable against formation of large-scale shear bands. Consequently, an inhomogeneous flow behavior will be resulted, as reflected in the indentation stress-strain curves in Fig.4.14 (b) and 4.15(b). In the next section (Sec.5), we will also discuss how what stops the deformation in a band during a time-dependent plastic deformation process, once the localization occurs.

Finally, we briefly address the effect of RTA on the plastic flow behavior of the PECVD SiO_x. In the nanoindentation stress-strain curves in Sec. 4.4, the as-deposited film has a lower initial and stationary yielding point compared with the annealed film. In addition, in the fully plastic flow, inhomogeneous flow also occurs earlier in the as-deposited film. We believe this is because that after RTA, the microstructure of the PECVD SiO_x becomes relatively more orderly. Consequently, the density of defects such as STZs (including the compressed/stretched Si-O and Si-OH bonds) is decreased. Thus we can expect the plastic deformation in the as-deposited film to be more pronounced, as evidenced by the nanoindentation stress-strain curves.

We'd like to end this section by noting that the shear transformation zone (STZ) based deformation mechanism presented in this project is just one possible way to interpret the experimental results. Nevertheless, this theory relies on few assumptions and does not exclude other possibilities. For example,

79

if there is a densification or an ordering transition under the indent, it will have an influence on the character of the plastic flow. However, from the STZ point of view, the changes in the size of shear bands and STZ clusters are equivalent as the densification or order transition effects at a local scale. In this sense, the two mechanisms are not contradictory to each other.

4.6. Conclusions

In this section, we explore the use of nanoindentation techniques as a method of measuring equivalent stress-strain curves of the PECVD SiO_x thin films.

Nanoindentation strain was analyzed by considering tip geometry changes during the indentation process. Nanoindentation stress was taken as the instant hardness, or mean pressure, underneath the indenter. Four indenter tips with different geometries were adopted in our experiments, enabling us to probe the elastic, elasto-plastic, and fully plastic deformation regimes of the PECVD SiO_x thin films.

Based on the experimental results, a shear transformation zone (STZ) based amorphous plasticity theory is applied to depict the plastic deformation mechanism in the PECVD SiO_x. The physical origin of the STZ is elucidated and linked with the plastic deformation dynamics.
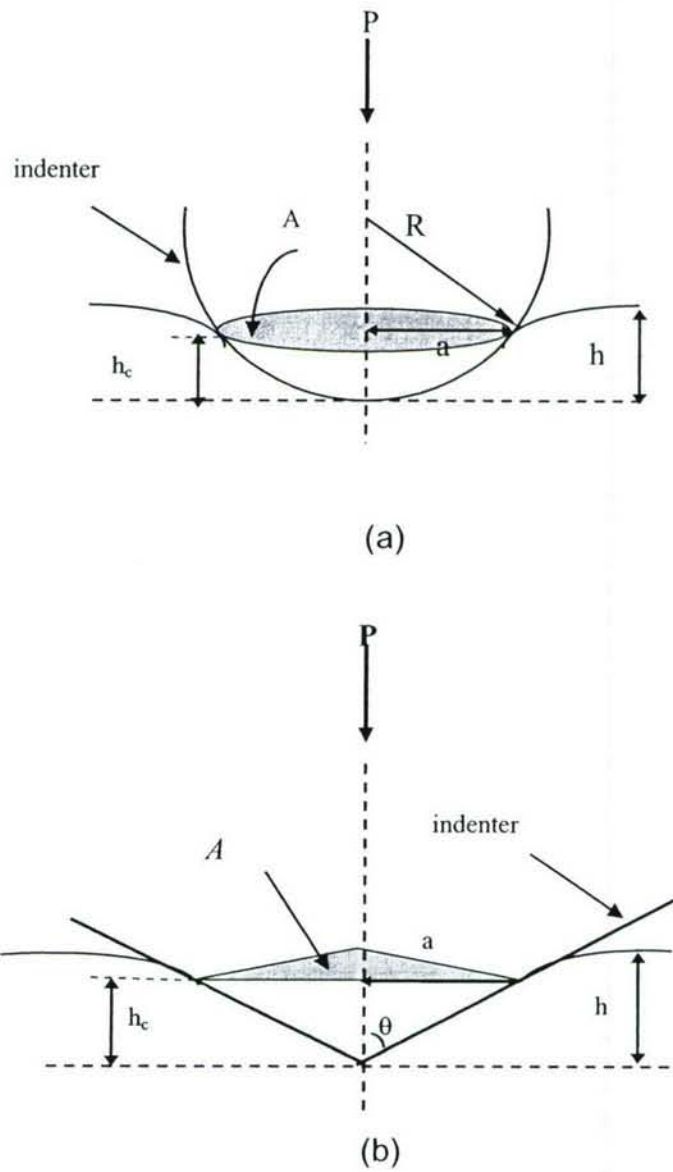
Fig.4.1. Schematic of the indentation process with (a) a spherical shaped tip, and (b) a sharp pyramidal tip.
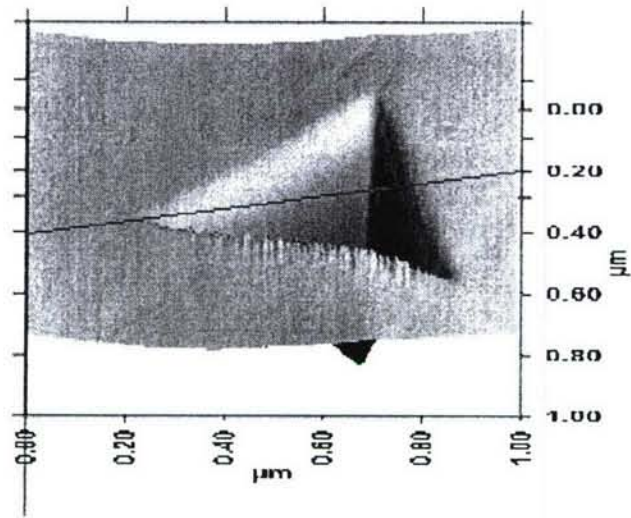
(a)
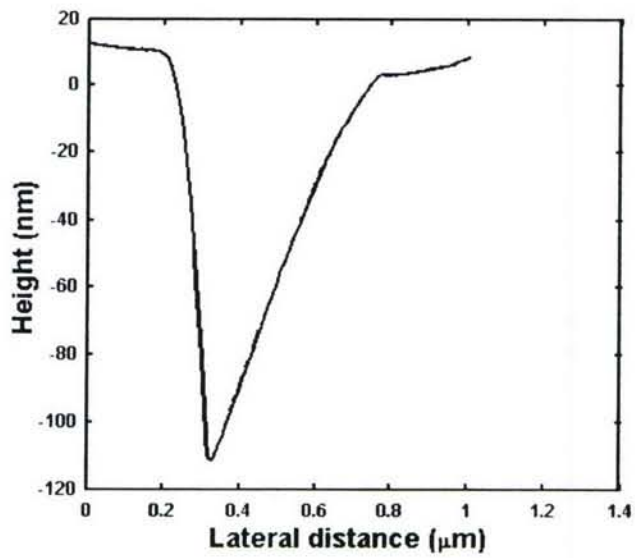
(b)

Fig.4.2. (a) The 3-D image and (b) cross section line profile (through an edge and opposing face) of an indent made by the Cube Corner tip on the standard fused quartz sample (CRL experiment, P_{max}=2 mN).
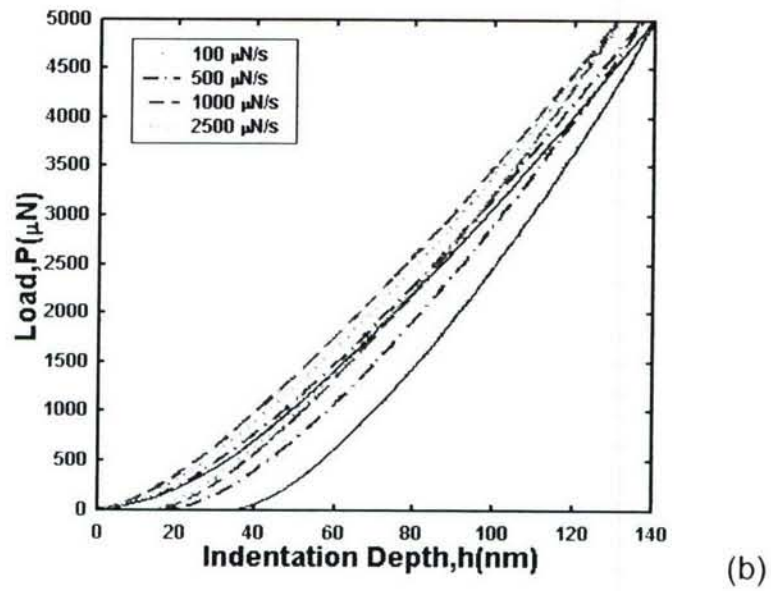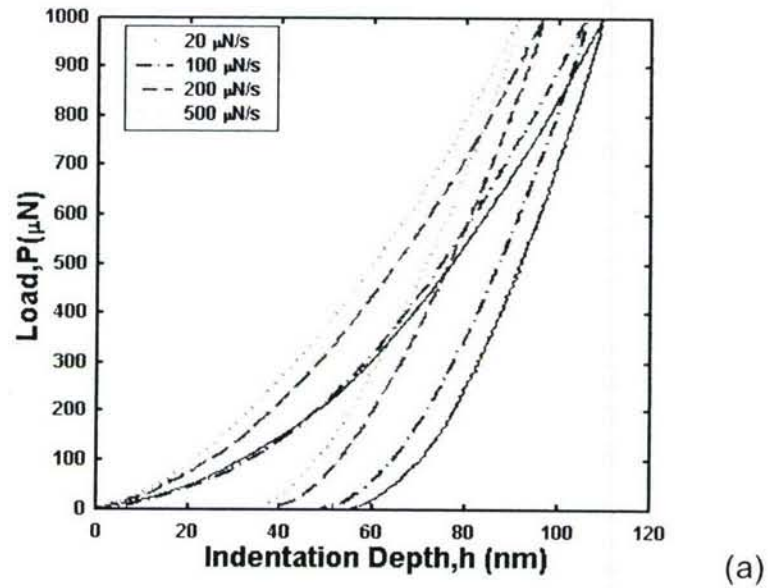
Fig.4.3. Nanoindentation load-depth (*P-h*) curves with various loading rates, obtained from (a) Berkovich tip and (b) 5-μm conical tip on the as-deposited PECVD SiO$_x$ thin film.
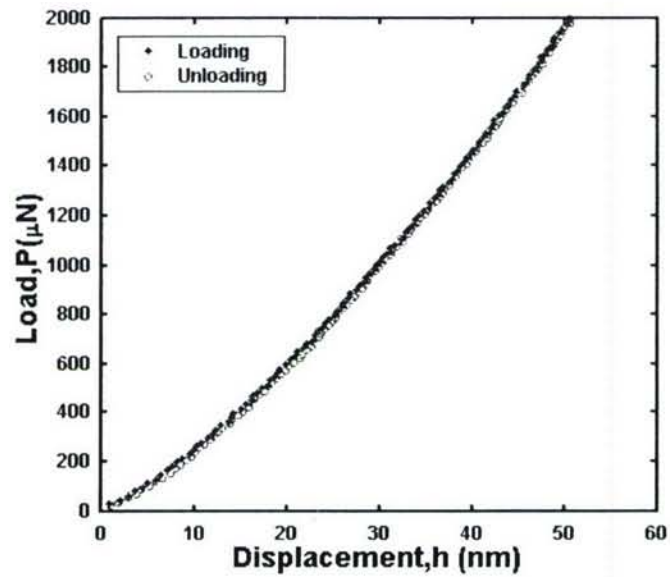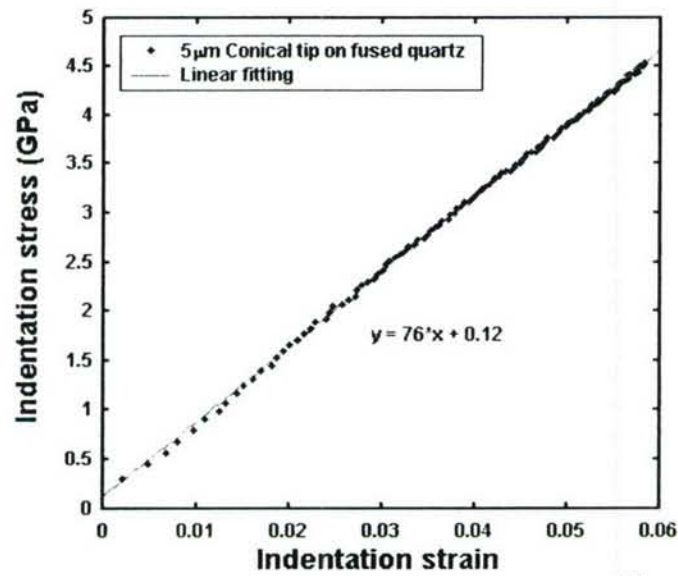
Fig.4.4. (a) Load-displacement (*P-h*) and (b) indentation stress-strain ($\overline{\sigma}$ -ε_I) curves of a constant rate of loading (CRL) nanoindentation test with a 5μm Conical tip on the fused quartz.
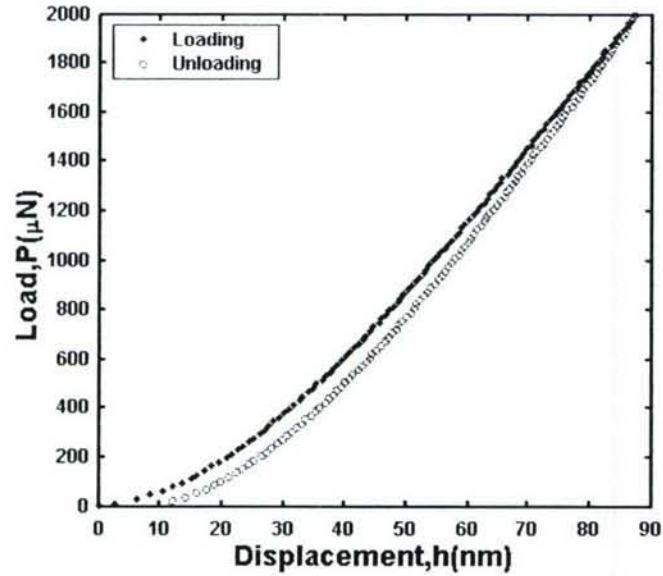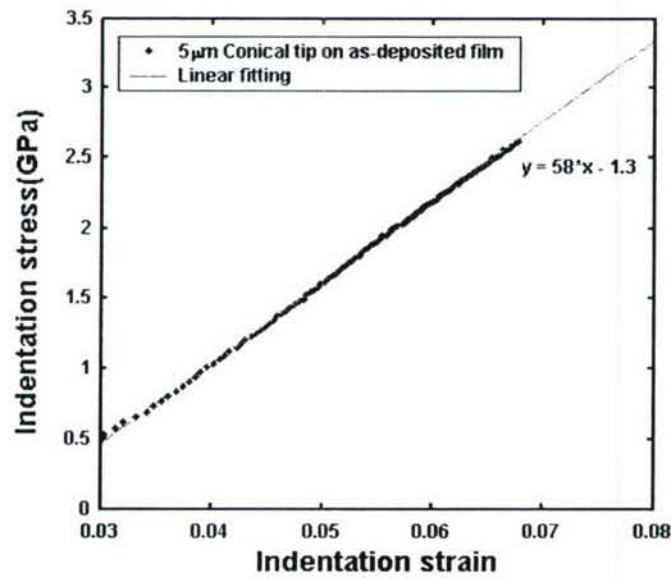
Fig.4.5. (a) Load-displacement (*P-h*) and (b) indentation stress-strain ($\bar{\sigma}$ -ε_I) curves of a constant rate of loading (CRL) nanoindentation test with a 5μm Conical tip on the as-deposited PECVD SiO$_x$ thin film.
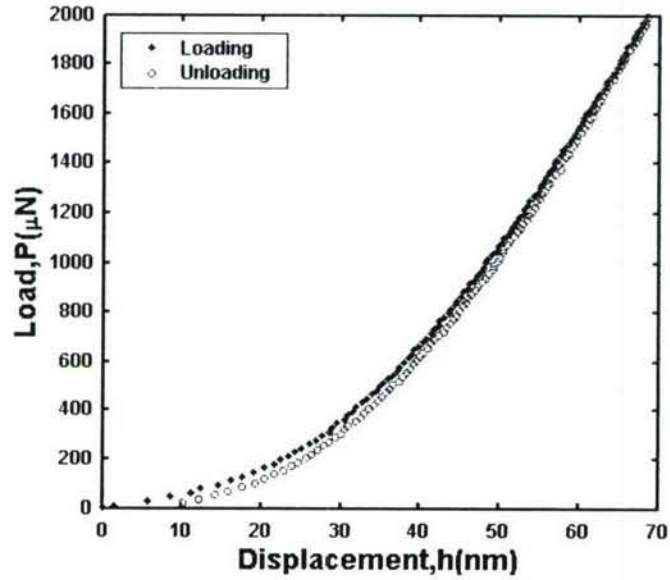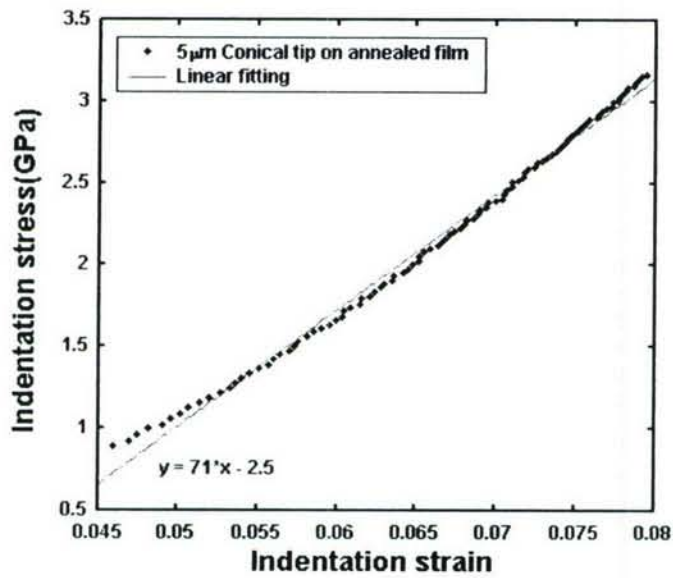
Fig.4.6. (a) Load-displacement (*P-h*) and (b) indentation stress-strain ($\bar{\sigma}$ -ε_I) curves of a constant rate of loading (CRL) nanoindentation test with a 5μm Conical tip on the annealed PECVD SiO$_x$ thin film.
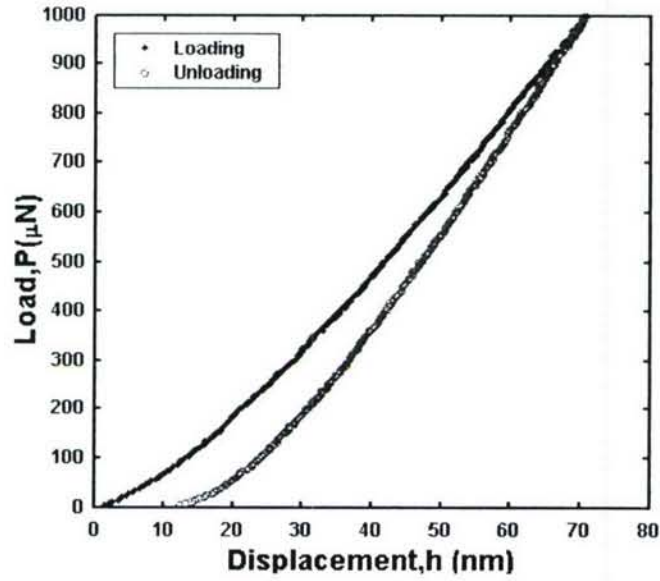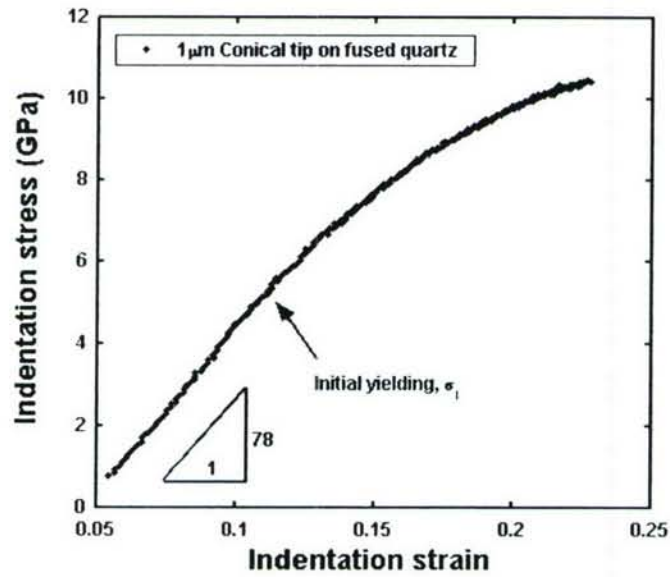
Fig.4.7. (a) Load-displacement (*P-h*) and (b) indentation stress-strain ($\bar{\sigma}$-ε_I) curves of a constant rate of loading (CRL) nanoindentation test with a 1μm Conical tip on the fused quartz.
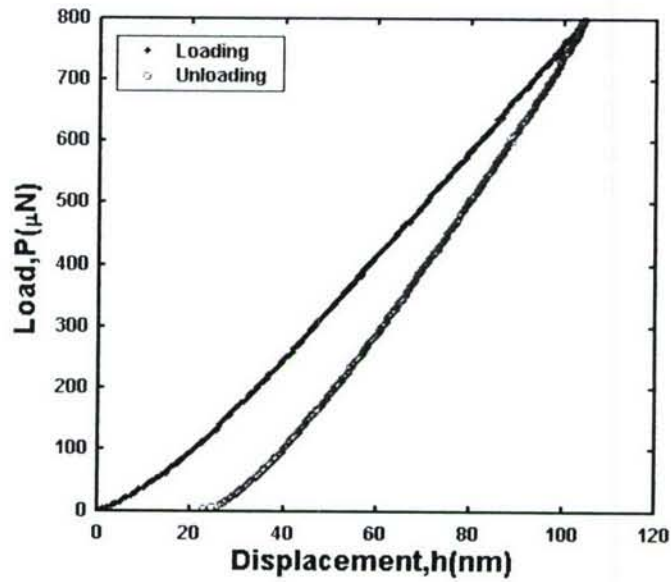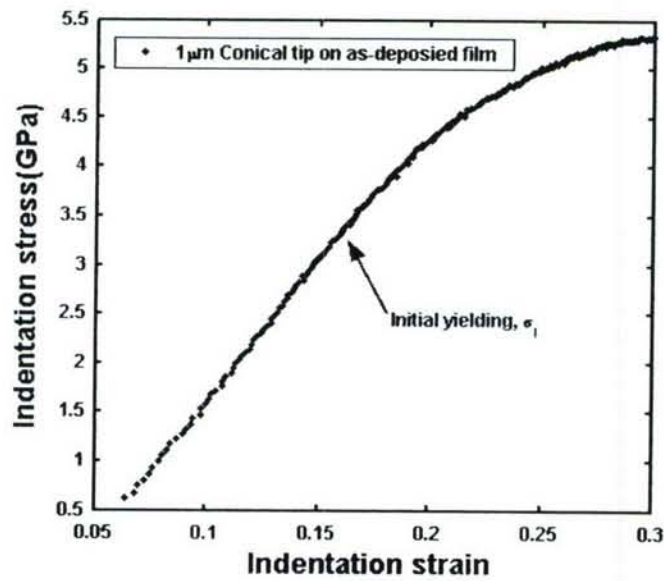
Fig.4.8. (a) Load-displacement (*P-h*) and (b) indentation stress-strain ($\bar{\sigma}$ -ε_J) curves of a constant rate of loading (CRL) nanoindentation test with a 1μm Conical tip on the as-deposited PECVD SiO$_x$ thin film.
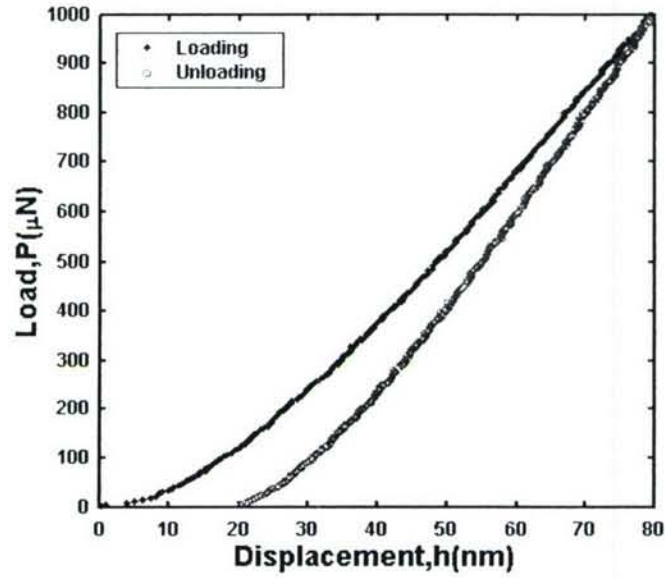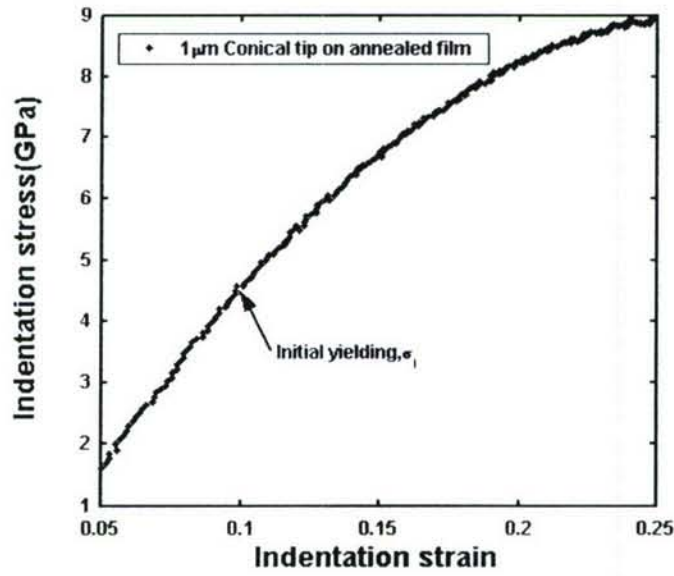
Fig.4.9. (a) Load-displacement (P-h) and (b) indentation stress-strain ($\bar{\sigma}$ - ε_I) curves of a constant rate of loading (CRL) nanoindentation test with a 1µm Conical tip on the annealed PECVD SiO$_x$ thin film.
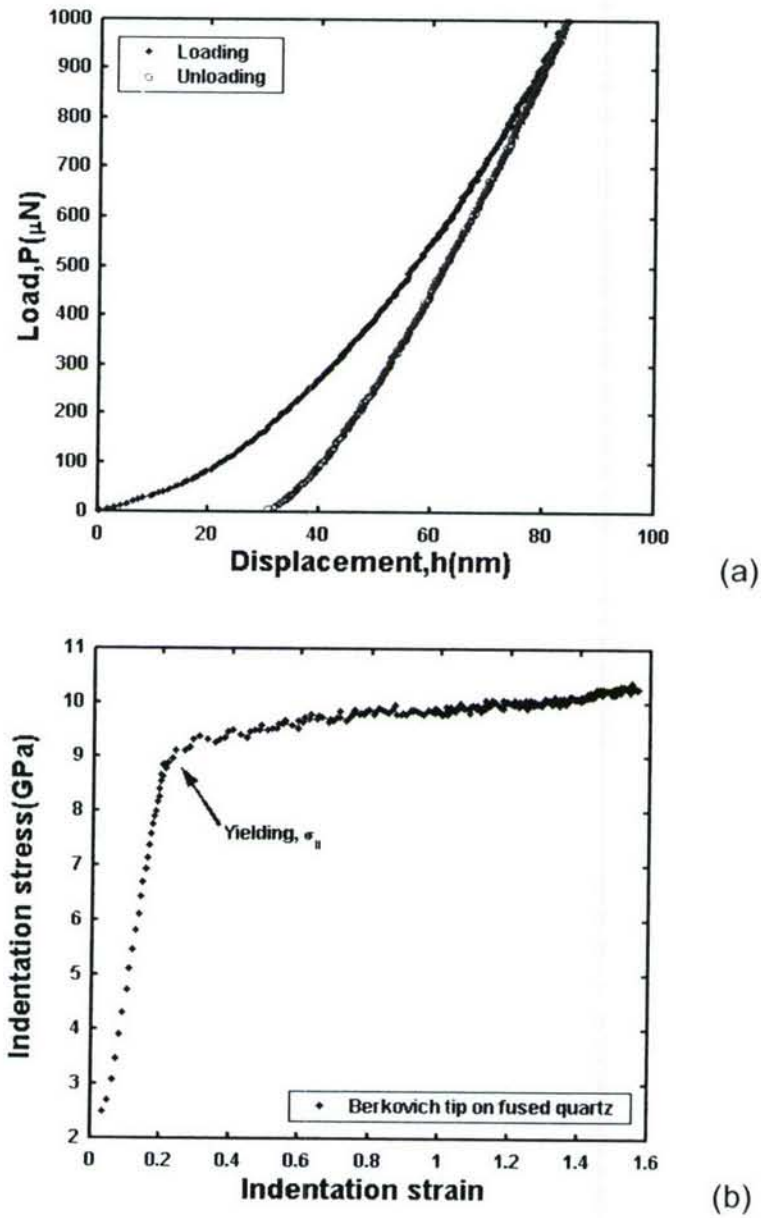
Fig.4.10. (a) Load-displacement (*P-h*) and (b) indentation stress-strain ($\overline{\sigma}$-ε)
curves of a constant rate of loading (CRL) nanoindentation test with a Berkovich
tip on the fused quartz.
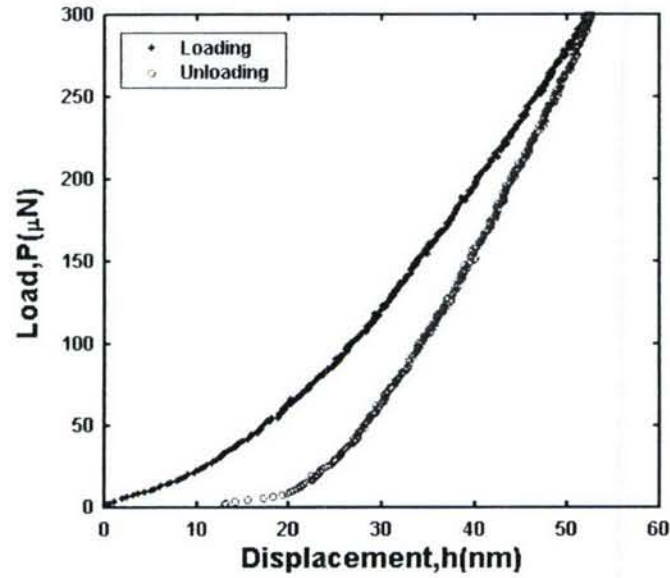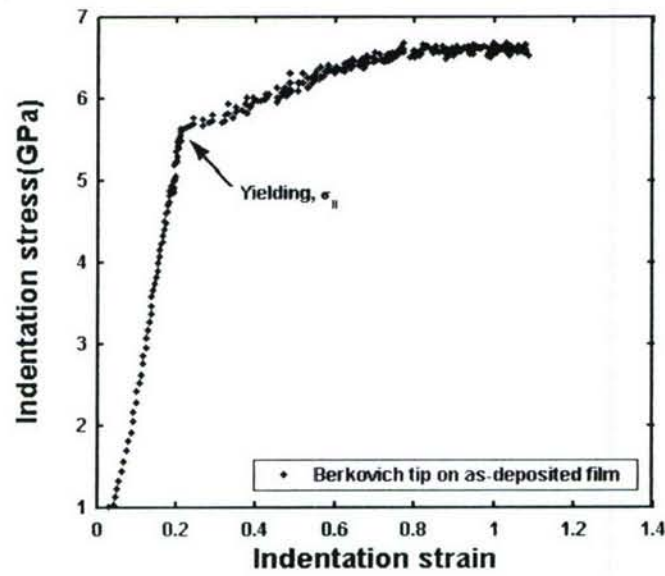
Fig.4.11. (a) Load-displacement (*P-h*) and (b) indentation stress-strain ($\overline{\sigma}$-ε_r) curves of a constant rate of loading (CRL) nanoindentation test with a Berkovich tip on the as-deposited PECVD SiO_x thin film.
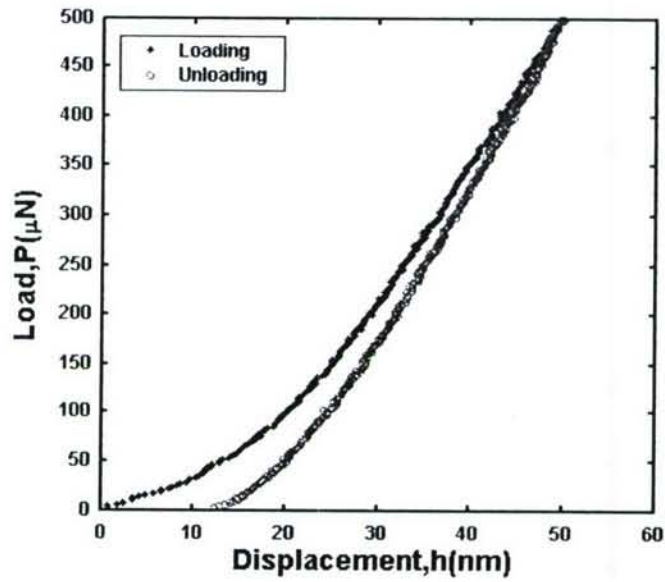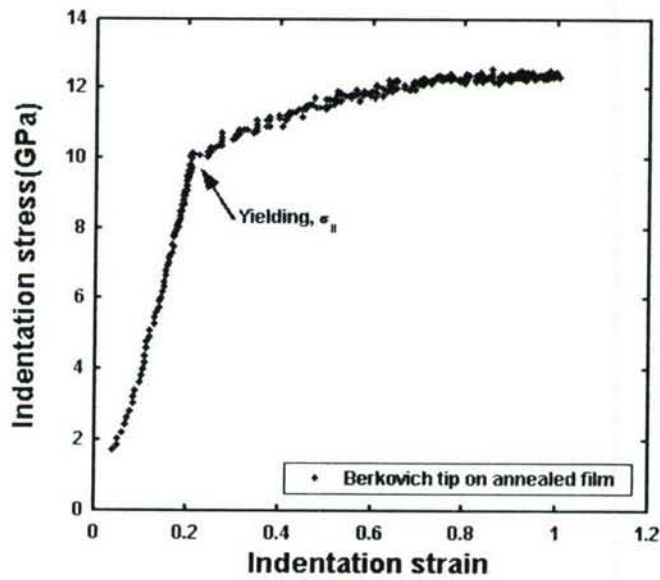
Fig.4.12. (a) Load-displacement (*P-h*) and (b) indentation stress-strain ($\overline{\sigma}$ -ε,) curves of a constant rate of loading (CRL) nanoindentation test with a Berkovich tip on the annealed PECVD SiO$_x$ thin film.
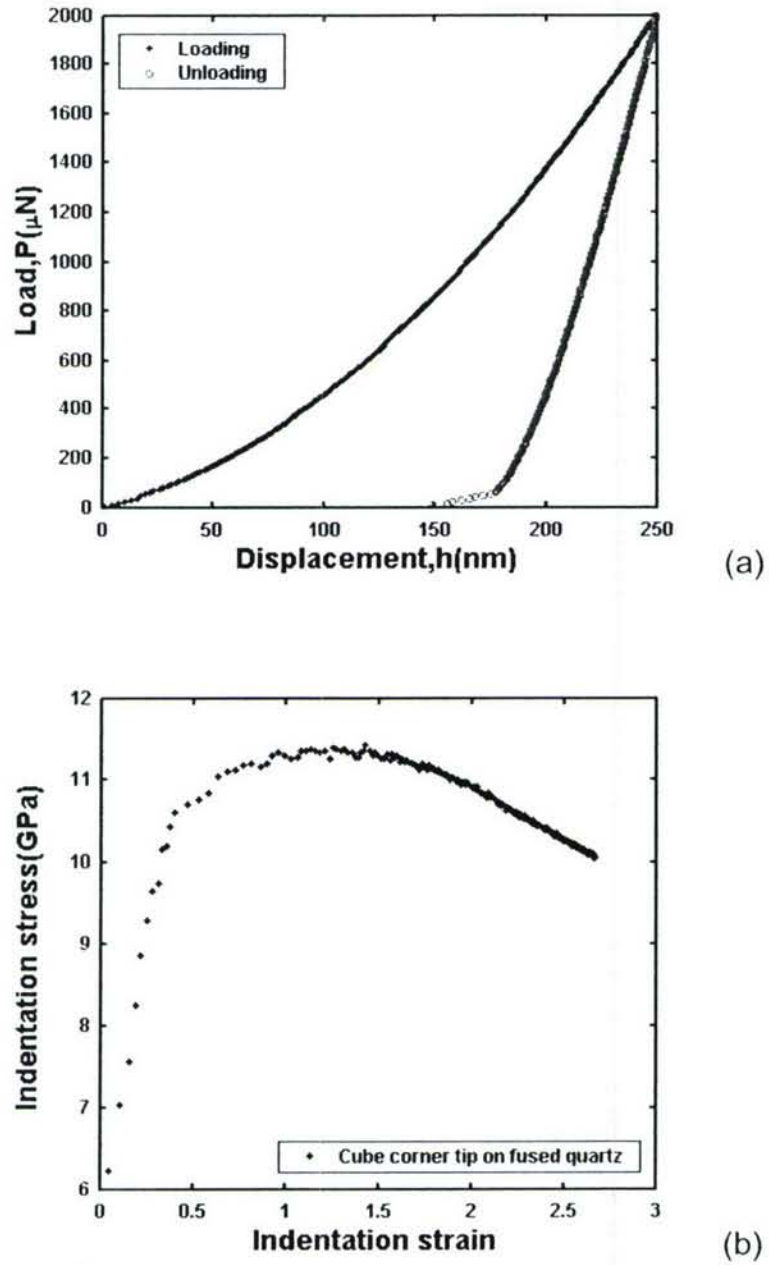
**Fig.4.13.** (a) Load-displacement (*P-h*) and (b) indentation stress-strain ($\bar{\sigma}$ -ε_I) curves of a constant rate of loading (CRL) nanoindentation test with a Cube corner tip on the fused quartz.
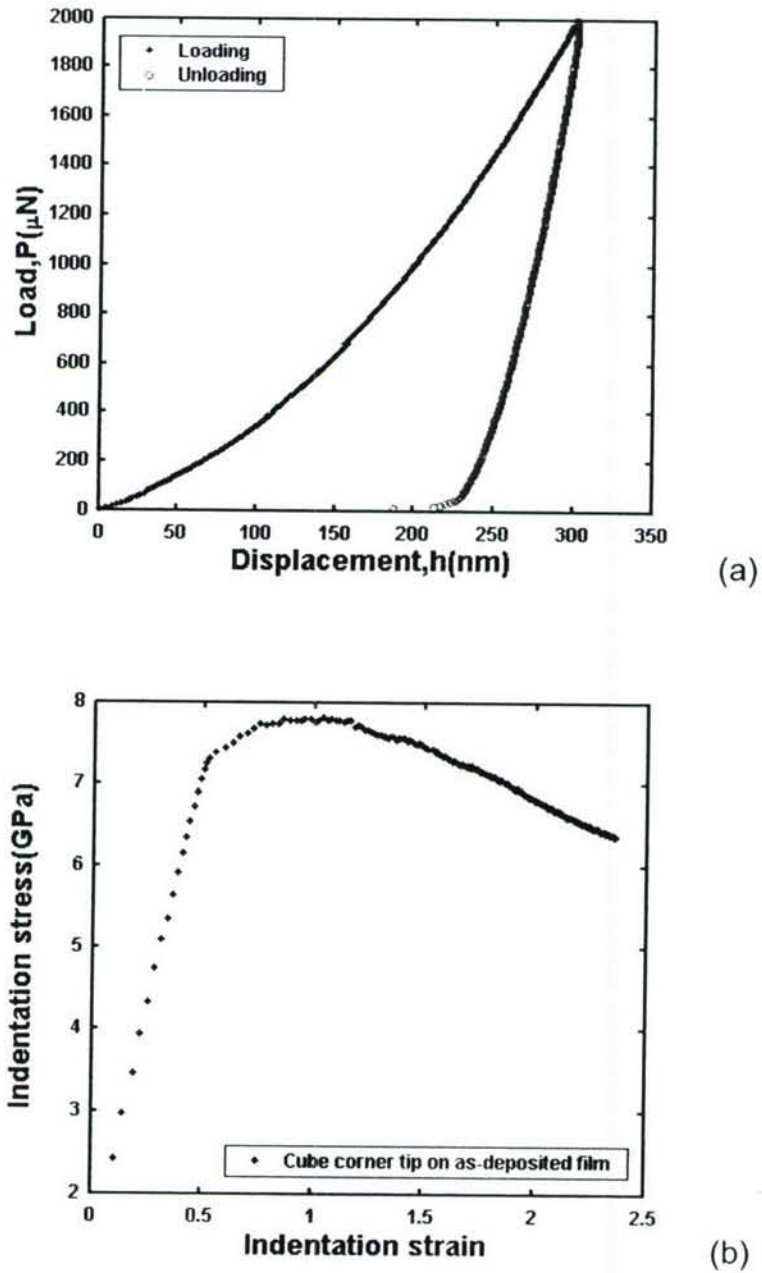
Fig.4.14. (a) Load-displacement (*P-h*) and (b) indentation stress-strain ($\overline{\sigma}$ -ε_I) curves of a constant rate of loading (CRL) nanoindentation test with a Cube corner tip on the as-deposited PECVD SiO$_x$ thin film.
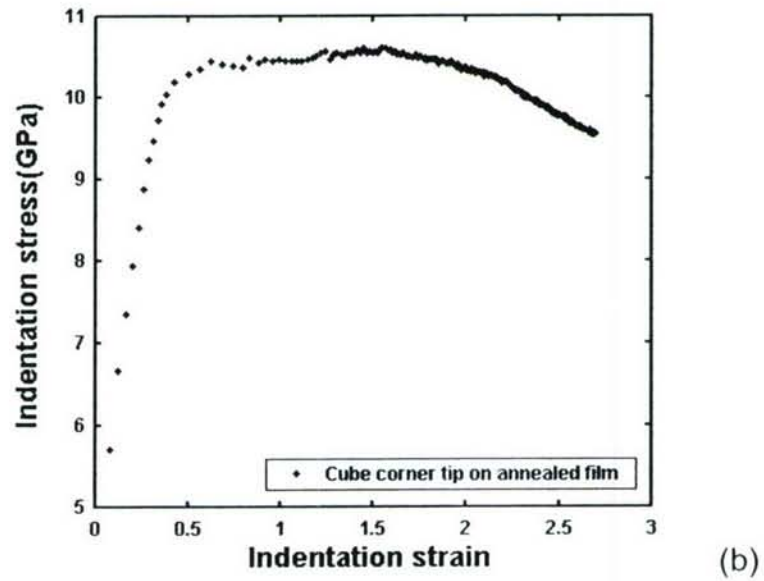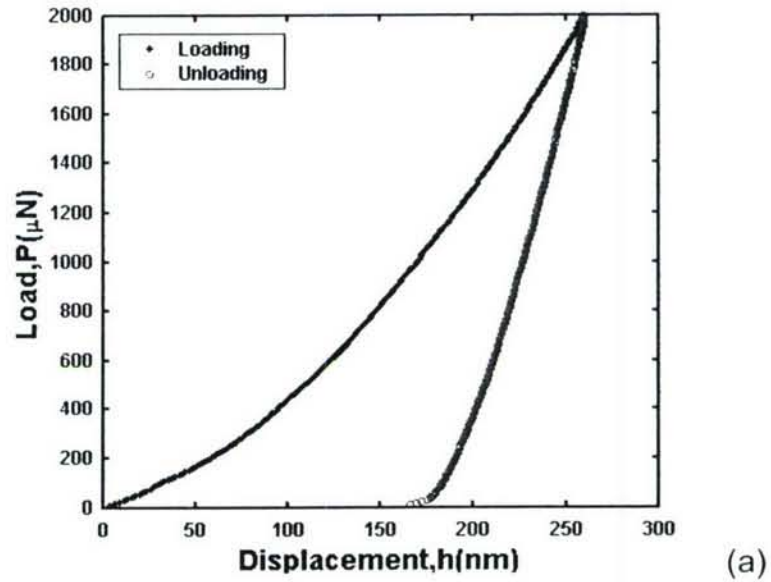
**Fig.4.15.** (a) Load-displacement (*P-h*) and (b) indentation stress-strain ($\bar{\sigma}$-ε_I) curves of a constant rate of loading (CRL) nanoindentation test with a Cube corner tip on the annealed PECVD SiO$_x$ thin film.
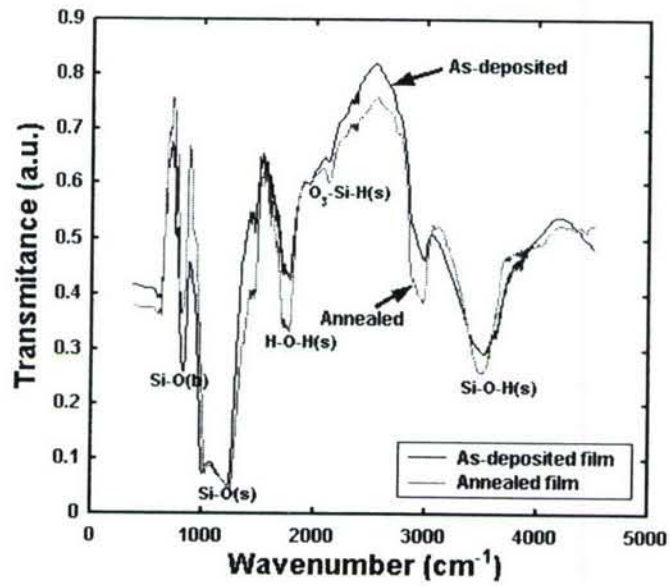
Fig.4.16. FTIR spectra of the as-deposited and annealed PECVD SiO$_x$ thin films. The main features have been identified.
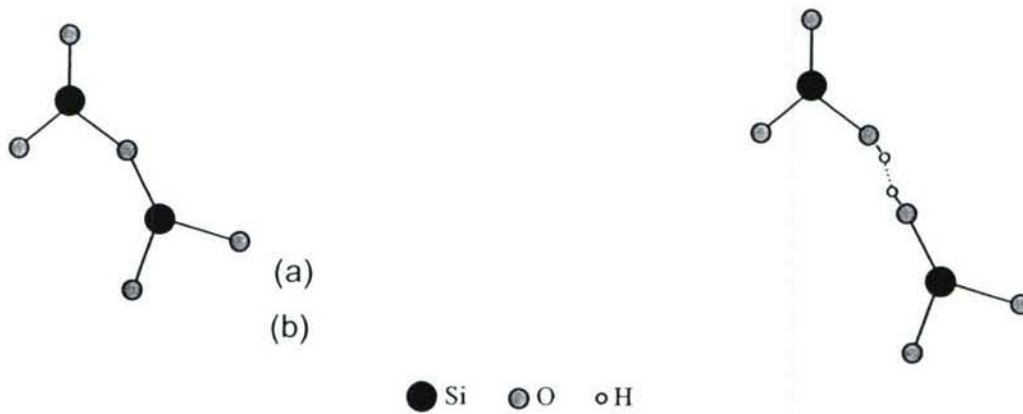
Fig.4.17: Schematic of the fundamental STZ cluster units: (a) Si-O units; (b) Si-OH units.

5. SIZE-DEPENDENT CREEP BEHAVIOR

Abstract: The time-dependent plastic deformation (creep) behaviors of both the as-deposited and annealed plasma-enhanced chemical vapor deposited (PECVD) silicon oxide (SiO_x) films were probed by nanoindentation load relaxation tests at room temperature.   Our experiments found a strong size effect in the creep responses of the as-deposited PECVD SiO_x thin films, which was much reduced after rapid thermal annealing (RTA).   Based on the experimental results, the deformation mechanism is depicted by the "shear transformation zone" (STZ) based amorphous plasticity theories. The physical origin of the STZ is elucidated and linked with the shear banding dynamics. It is postulated that the high strain gradient at shallow indentation depths may be responsible for the reduction in the steady-state stress exponent n= ?log(strain rate)/?log(stress), characteristic of a more homogenous flow behavior.

5.1. Introduction

The time-dependent plastic deformation, or creep, behaviors of PECVD SiO_x, is related to the long-term reliability issues in its applications in MEMS and are currently not well understood. In this section, creep responses of both the as-deposited and annealed PECVD SiO_x films were probed by the nanoindentation (introduced in Sec.2, 4) load relaxation experiments at room temperature. As a comparison, a standard fused quartz sample was also tested under the same conditions. In the as-deposited PECVD SiO_x thin films, our experiments found a strong size effect in the nanoindentation creep responses, which is characterized by the variations in the steady-state stress exponent, n=?log(strain rate)/?log(stress). Furthermore, this size effect was much reduced for both the annealed PECVD SiO_x thin film and the fused quartz.   The deformation mechanisms of the various nanoindentation creep processes are

depicted by the "free volume" and "shear transformation zone" (STZ) based amorphous plasticity theories (Spaepen 1977; Argon 1979; Falk and Langer 1998; Langer 2001; Falk et al 2004). The physical origin of the STZ is elucidated and linked with the shear banding dynamics. It is postulated that the high strain gradient at shallow indentation depths may be responsible for the reduction in the stress exponent, characteristic of a more homogenous flow behavior. We also propose that the increase of the dispersed quasicrystal-like order in the annealed film may contribute to a more localized flow behavior than its as-deposited counterpart.

5.2. Experimental Details

A 2μm-thick, silane-based PECVD SiO$_x$ film was deposited silicon wafers using the same conditions as Sec.3 and 4. The wafer was subsequently diced into approximately 10 mm × 10 mm squares. Similar to Sec.4, before testing, some samples were annealed in an RTP-600S rapid thermal annealing (RTA) system (from Modular Process Technology Corp., San Jose, CA) for 10 min at 800°C in a nitrogen environment. All the references of the "annealed film" in the rest of the section refer to the PECVD SiO$_x$ films that were treated by RTA described above.

The nanoindentation tests were conducted at room temperature on a TriboIndenter[TM] system (from Hysitron Inc., Minneapolis, MN), which is capable of high-rate, high-resolution measurements, as introduced in Sec.4. A standard Berkovich tip was used, with a pyramidal tip shape and a tip radius of approximately 150 nm. The machine compliance and tip area functions were calibrated following the procedures outlined in Sec.4.3.2 in Sec.4.

Prior to each test, efforts were made to minimize the effects of the thermal drift by allowing thermal equilibrium to be reached for more than one hour. Consequently, the thermal drift became steady and typically could reach 0.01

nm/s or less. Compensations were then automatically made to correct the data.

Indentation load relaxation (ILR) tests were separately performed on the as-deposited PECVD SiO_x, annealed PECVD SiO_x, and the fused quartz samples, all in a load-controlled mode and under a constant peak load ranging from 500 to 5000 μN. The holding time was 100 s in all the experiments, as shown in the load scheme Fig.5.1. Each test was repeated at least 5 times under the same loading condition for each sample.

For our PECVD SiO_x thin films samples (both as-deposited and annealed), when the peak load was 5 mN, the maximum indentation depth was less than 300 nm, or 15% or the film thickness. Thus, the influence of the silicon substrate effects should have been minimal (Bhattacharya and Nix 1988).

5.3. Data Analysis

For a given material, different creep mechanisms may be operative at the different temperatures and stress levels. To gain more insights into the time-dependent properties of the sample materials, it is desirable to obtain the relationship between the nanoindentation strain rates ($\dot{\varepsilon_i}$) and the average indentation stress $\bar{\sigma}$ during the holding time. In the uniaxial tests, the steady-state creep behavior of a wide range of materials can be described by (Lucas and Oliver 1999; Poisl et al 1995):

$$\dot{\varepsilon} = A\sigma^n \qquad \text{(Eq. 5.1)}$$

Here, σ is the uniaxial stress on the specimen, $\dot{\varepsilon}$ the experimental strain rate, n the exponent of power-law stress, termed the stress exponent, and A is a constant for given material and temperature. In the conventional uniaxial creep tests, either the stresses or the strain rates are kept constant. Indentation creep tests, however, are different with traditional uniaxial tests in several ways. First, the stresses generated in an indentation test include compressive, tensile, and

shear stresses in all the directions. The strain rates experienced in an indentation test is also much more complex and may cover a wide range, especially at the beginning of the indentation (Poisl et al 1995). Despite all the differences, a number of previous theoretical and experimental studies have found that it is possible to link the results of indentation to those obtained from the uniaxial tests (Tabor 1951; Bower et al 1993; Storåkers and Larsson 1994; Hill 1992). Tabor (1951) first proposed an empirical "equivalent strain" concept, which was validated by Bower et al (1993) through both rigorous theoretical modeling and finite element analysis. Storåkers and Larsson (1994) extended the work of Hill (1992) on the contact mechanics of the indentation process, and also determined that the indentation creep could be defined by an equivalent indentation strain rate. These results generally show that for Berkovich (and other self-similar) tips, the indentation strain rate $\dot{\varepsilon}_I$ scales as:

$$\dot{\varepsilon}_I \sim \frac{1}{h}\frac{dh}{dt} \qquad \text{(Eq. 5.2)}$$

In Eq.(5.2), h is the indentation depth, and t is the time. dh/dt is calculated by first fitting the h-t curve during holding with the empirical law (Li and Ngan 2004):

$$h(t) = h_0 + a\,(t\text{-}t_i)^b + kt \qquad \text{(Eq. 5.3)}$$

where h_0 (close to h_i, the initial indentation depth), a, b, and k are fitting constants, and t_i is the time when the creep process is initiated. As we will show later, Eq.(5.3) fits most of the results very well, with $R^2 > 0.95$ or better. We have found that the choice of the fitting equations does not significantly influence the final results, as long as they can reproduce the trend of the data reasonably well. For example, a good parabola fitting in segments generates approximately the same results with Eq.(5.3). However, Eq.(5.3) is more preferable in capturing the overall trend of the data, and it generally has the best fitting results as it utilizes the whole data set, except at $t=t_0$, which is excluded in the analysis to avoid singularity.

At very small depth, the shapes of the pyramidal tips and conical tips are rounded (Sec.4). For these tips, the maximum contact depth below which the indent shape is spherical can be estimated by the equation (Li and Ngan 2004):

$$\delta_0 = R(1 - \sin \beta) \qquad \text{(Eq. 5.4)}$$

where β is the semiangle of the indenter tip, and R is the tip radius. δ_0 is approximately 14 nm for our Berkovich tip, whose $\beta= 65.35°$. All our experimental results in this section were obtained at indentation depths far greater than 14 nm.

As we discussed previously in Sec.4, many applications of the instrumented indentation are limited by the complications in clearly interpreting the results. Such complications arise mainly from the "pile-up" or "sink-in" of the material around the indenter (Oliver and Pharr 2004). Fig.5.2 shows the load-displacement (P-h) relations of the constant rate of loading (loading/unloading times: 2s) and ILR experiments with a maximum load (P_{max}) of 5 mN. In our experiments, the indentation depths were small (<300 nm), and from Fig.5.2 (a) $h_f / h_{max} < 0.7$, where h_f is the final indentation depth, and h_{max} is the maximum indentation depth. Therefore, theoretically the "pile-up" should have been negligible (Oliver and Pharr 2004). This assumption was proven experimentally by the in-situ SPM (scanning probe microscopy) images which used the indenter itself as the imaging tip. For example, Fig.5.3 is a complete (inverse) 3D image showing the topography and the curvature of the faces after an indent on the standard fused quartz sample. Fig.5.4 demonstrates both the top view and a cross section line profile of the same indent as in Fig.5.3. During loading, both elastic and plastic deformation processes occur, and the indenter conforms perfectly to the pyramidal shape of the hardness impression. During unloading, however, the elastic recovery causes the hardness impression to change its shape, as accentuated by the (red) dashed straight lines in Fig.5.4 (b) (Oliver and Pharr 2004). Similarly, typical residual indents of the as-deposited and annealed PECVD SiO$_x$ films were shown in Fig.5.5. It can be directly observed from the

SPM images such as Figs.5.3-5.5 that the "pile-up", if any, was negligible in all the tested sample materials.

The "sink-in" was primarily caused by the elastic deflection of the specimen surface, and the relation $h_c = f(h)$ between contact depth (h_c) and the measured instant maximum depth (h) was calibrated before the experiments. In our experiments, we found that $h_c = f(h)$ is approximately linear, as predicated by theory (Oliver and Pharr 1992; 2004). By examining a wide range of different loading/holding conditions, we also found that the variations of f is small and well within the ±5% error range typically associated with nanoindentation measurements. Knowing $h_c = f(h)$ and the area function of the nanoindenter tip $A = F(h_c)$, it is possible to evaluate also the instant hardness H in a creep process following

$$H = \frac{P}{A}$$
(Eq. 5.5)

Note that H also signifies the mean pressure, or the average stress $\bar{\sigma}$, that can be sustained under the indentation load (Freund and Suresh 2004).

5.4. Experimental Results

Significant creep displacements were observed in all the samples during the holding time of the ILR tests. The relations between the creep displacement (h-h_i) and creep time (t-t_i) for the three materials under different peak loads (P_{max}) are plotted by the colored dots in Figs.5.6 (a)-(c). The smooth black solid lines represent the respective fittings by Eq.(5.3). It can be seen that for the larger peak loads, its total creep displacement is relatively larger.

The creep rate (strain rate during creep) $\dot{\varepsilon}_I$ and the stress $\bar{\sigma}$, both during the holding time, were calculated from Eq.(5.2) and Eq.(5.5), respectively. It is

found that $\dot{\varepsilon}_I$ declines with time, as shown in Figs.5.7 (a)-(b), reaching approximately a steady state as the displacement rate *dh/dt* decreases. Obviously, $\bar{\sigma}$ also decreases with time as the creep displacement (and thus the projected area) increases. Comparing Figs.5.7 (a)-(b), it is also apparent that the strain rate at small indentation depths is relatively larger than that of the deeper indentation depths.

Figs.5.8 (a)-(b) are the $\log \dot{\varepsilon}_I - \log \bar{\sigma}$ relations of the as-deposited PECVD SiO_x films under the minimum (500 μN) and maximum (5 mN) constant peak loads. The slopes of both the curves, i.e. $n = \partial(\log \dot{\varepsilon}_I) / \partial(\log \bar{\sigma})$, drop significantly as the creep displacement increases and stress decreases. Evidently, with the smaller indent this reduction in the slopes is faster. At the steady state (i.e. toward the end of the holding time), *n* represents the stress exponent of a power-law creep (Lucas and Oliver 1999; Poisl et al 1995), and will be analyzed further for the better understanding of the creep process. It is apparent from Figs.5.8 (a)-(b) that at for very shallow indents, the steady-state stress exponent *n* is on the order of unity (~5). As the load increases 10 times, *n* increases quite dramatically (to ~67). The above observations, including the size effects in stress exponents in Figs.5.8 (a)-(b), are qualitatively the same for the annealed PECVD SiO_x thin film and the fused quartz samples, whose related results are shown in Figs.5.9-5.10 for comparison.

Finally, Fig.5.11 shows the variations of stress exponent values at the end of holding time, as a function of peak load for three different sample materials. The nominal initial indentation depths at the various loads are tabulated in Table 5.1. After RTA, the stress exponents of the PECVD SiO_x films are generally much increased under comparable loading conditions. In addition, it is evident that the stress exponents of all the sample materials exhibit a strong size effect at the smallest indentation depth, with a value on or approaching the order of unity. As the load and indentation depth increases, *n* quickly saturates into a

large value of ~150 for the annealed film. For the fused quartz sample, it also shows a sign of saturation within the tested range. However, as for the as-deposited film, no similar trend is yet observed within the 5 mN range.

The different size effects in the stress exponent values of the tested samples may suggest there is a difference in their deformation mechanisms during creep. To understand the phenomena better, we also measured the hardness (equivalent as average stress) values of different samples, as shown in Fig.5.12. After RTA, the hardness of the PECVD SiO_x thin film is increased to a value close to that of fused quartz. There are, however, no significant size effects in hardness in the annealed film and the fused quartz within the same load range. For the as-deposited PECVD SiO_x film, a small but noticeable size effect can be observed at small peak loads. At larger loads, the hardness values do not vary significantly. In any case, the size effects in stress exponent in Fig.5.11 seem hardly directly correlated with the size effects in hardness, shown in Fig.5.12.

5.5. Discussion

Indentation size effects (ISE) are mostly found in both microhardness and nanohardness tests of crystalline/polycrystalline materials (Tymiak et al 2001; Nix and Gao 1998; Fleck and Hutchison 2001). Although the underlying mechanisms remain irresolute, a "strain gradient plasticity (SGP)" theory (Nix and Gao 1998; Fleck and Hutchison 2001) has been successfully applied to explain a wide range of experiments. This theory proposes that the large strain gradient inherent to small indents leads to "geometrically necessary dislocations" that cause enhanced hardening. When the grain size decreases to the nanometer range, i.e. in nanocrystalline solids, enhanced size effects and strain rate sensitivity are often observed, and attributed to the presence of a large density of grain boundaries (GB) (Schwaiger et al 2003; Lu et al 2000; Schiøtz et al 1998).

104

The occurrences of plastic deformation in all of our sample materials were confirmed by both the nanoindentation load-displacement (P-h) curves and the SPM images of residual indent prints such as Fig.5.2 and Figs.5.3-5.5. Thus, the creep behaviors observed in Sec.4 were apparently induced by plasticity.

Due to their fabrication methods, both the fused quartz and the PECVD SiO_x are known to be amorphous. Generally speaking, in amorphous solids, the physical process of plastic deformation differs substantially from those of the crystalline, polycrystalline, and nanocrystalline materials. Clearly identifiable defects, such as dislocation and GB, cease to provide a useful description of the microstructural dynamics (Langer 2001). In the most widely accepted theory of amorphous plasticity, Spaepen (1977), Argon (1979) and others have shown that at low temperature and high stress, the flow is inhomogeneous and plastic deformation occurs at localized sites (called flow defects) in the form of "shear bands". Falk, Langer, and others (Falk and Langer 1998; Langer 2001; Falk et al 2004) have further built on such models and proposed that the deformation is mediated by the activation of the rearrangement of a particularly oriented cluster of atoms, known as shear transformation zones (STZ).

As a result of the PECVD process, a large density of the Si-O bonds in the as-deposited PECVD SiO_x is either distorted (i.e. compressed or stretched) or dangling/broken (such as $-SiO_3$ bonds), forming defects. In addition, our previous SIMS (Second Ion Mass Spectroscopy) analysis found that there was a significant hydrogen concentration near the free surface of the film ($\sim$ 6.7%), which decreased to $\sim$ 2% at about 500 nm from the free surface (Cao and Zhang 2004). Due to the RF plasma environment, the incorporated hydrogen atom is likely to be ionized and enters into the Si-O network, forming Si-OH bonds. After thermal annealing, this hydrogen concentration is dramatically reduced (to a relatively constant level of $\sim$0.1% at all depths). The hardness of the film is increased (shown in Fig.5.12), as the defect density is reduced and a relatively more orderly microstructure is resulted.

In the STZ theory of amorphous plasticity, a large n (for example, $n>100$) implies that the flow is inhomogeneous. On the other hand, a small n (for example, <10) implies the flow is more viscous (in the case of $n=1$, the flow would be Newtonian viscous).

It can be inferred from Figs.5.8-5.10 that, due to a high stress level, the nanoindentation creep process starts out to be almost ideally plastic, with a high stress exponent and almost rate-insensitive. This may be explained by the conventional STZ theory: when the applied stress exceeds the yield stress, the movement of a first STZ (either weak Si-O, Si-OH bonds or the dangling/broken $-SiO_3$ bonds) will cause a local dilatation, or expansion of the nearby free volumes (Spaepen 1977). This, in turn, creates localized distortions of neighboring STZs, and triggers the autocatalytic formation of large bands of STZs, commonly called "shear bands" (Spaepen 1977; Argon 1979). Note that the shear bands formed here, although much larger than a single STZ, are still so small that they may not be detectable by techniques such as SPM (Figs.5.3-5.5). Nevertheless, they will result in a local softening of the material, as the dynamic excess free volume lowers the average shear resistance of the sheared regions. Eventually, the applied strain relaxes, and the growth of the bands stops due to dynamic effects or small but rapid stress drops in the vicinity of the bands (Argon 1979). Thus near the end of the holding time, we see a reduction in the stress exponent, indicating that the flow has become more homogeneous (i.e. viscous-like) than the start.

During the nanoindentation process of a sharp wedge (including the Berkovich tip), at very shallow depths, the applied strain gradient is significantly higher than that of the deeper indents (Tymiak et al 2001; Nix and Gao 1998; Fleck and Hutchison 2001). We postulate that this will create an extra imbalance among the STZs and promote the rate at which the shear bands form and relax underneath the indenter tip. To verify this argument, we turn to Figs.5.7-5.10. Faster rates of shear band formations would result in a higher strain rate at

smaller indentation depth, which is clearly supported by Fig.5.7. On the other hand, Figs.5.8-5.10 demonstrate that the relaxation rate is much greater at the smaller indentation depths. As a result of the quick termination in growth, the shear bands generated at very shallow depths should be generally much smaller. At steady state, atomic diffusion may be enhanced as a result of a higher rate of dynamic equilibrium of the rearrangement of STZs. As such, the numerous smaller shear bands in the specimen may collectively exhibit a more macroscopically viscous-like flow behavior, which is experimentally confirmed by a reduction in its stress exponent at shallow depths in Fig.5.11. In other words, the length-scale effect in an amorphous material might be related to the sizes of the shear bands. When the shear bands are small and numerous, a more "homogenous" flow behavior will be resulted; whereas if the shear bands are large and few, the flow behavior will become more "inhomogeneous". Variations in their stress/strain distribution profiles might also play a role in determining the quantitative values of stress exponents at different loads/depths, but based on our previous discussions on the "equivalent stress/strain" concept, it's unlikely that such variations would affect the overall qualitative conclusions.

We further propose that the size effect in the stress exponents is much more pronounced in the as-deposited PECVD SiO_x film, mainly because 1) its defect density is higher, especially near the free surface and 2) the shear resistance of the STZs is intrinsically weaker than that of the annealed film or the fused quartz. This is based on the recent experimental evidence and simulation study that suggest the dispersed local quasicrystal-like order plays a critical role in controlling the qualitative nature of amorphous plasticity (Shi and Falk 2005; Saksl et al 2003). Larger degrees of quasicrystal-like order tend to increase shear localization (Shi and Falk 2005). To validate this claim, we performed additional X-ray diffraction (XRD) measurements (with a D8 Focus [TM], from Bruker AXS Inc., Madison, WI) on both the as-deposited and annealed PECVD SiO_x thin films and the results are presented in Fig.5.13. It can be seen that for

the as-deposited film, the data does not show any clear features, confirming that the material microstructure is totally amorphous. However, after RTA, a noticeable peak can be resolved at ~22°, indicating that some of the amorphous SiO_x clusters possess an increased medium-range order (Gaskell and Wallis 1996; Comedi et al 2006). In other words, after RTA, the microstructure becomes relatively more orderly and the "quasicrystal-like order" is increased.

It is possible that in the as-deposited PECVD SiO_x, the paucity of such "quasicrystal-like order" may contribute to a generally less inhomogeneous flow behavior, or a reduction in steady-state stress exponent, as seen in Fig.5.11. On the other hand, the increase of the dispersed quasicrystal-like order, by reducing the defects in the annealed film, may contribute to a more localized flow behavior in the steady-state than its as-deposited counterpart.

Due to the depth dependence of the hydrogen content, we caution here that the clear interpretation of the results of the as-deposited films is likely to be complicated. However, the size effects in stress-exponents were also observed at small loads/depths in the annealed films, which had a constant level of hydrogen of ~0.1%; as well as in the fused quartz, which does not contain similar defects. It is therefore argued that the size effect in this paper is a true local length-scale effect, although it can be influenced by other factors such as defect density distributions etc.

Since the conventional STZ theories generally do not contain an explicit "length scale" factor, we call for further experimental and theoretical studies into the size effects in amorphous plasticity to gain more understanding of the underlying mechanisms.

6. Conclusions

The time-dependent plastic behaviors of both the as-deposited and annealed plasma-enhanced chemical vapor deposited (PECVD) silicon oxide

(SiO$_x$) films were probed by the nanoindentation creep experiments at room temperature. Our experiments found a strong size effect in the creep responses of the as-deposited PECVD SiO$_x$ thin films, which was much reduced after annealing. Based on the experimental results, the deformation mechanism is depicted by the "shear transformation zone" based amorphous plasticity theories. The physical origin of the STZ is elucidated and linked with the shear banding dynamics. It is postulated that the high strain gradient at shallow indentation depths may be responsible for the reduction in the stress exponent, characteristic of a more homogenous flow behavior. We also propose that the increase of the dispersed quasicrystal-like order in the annealed film may contribute to a more inhomogeneous flow behavior than its as-deposited counterpart.

Table 5.1. Initial indentation depths at various loads in different samples.

| Nominal P_{max} (mN)		0.5	1	2	3	4	5
Initial indentation depths (nm)	As-deposited	57.552	99.067	149.71	184.39	215.21	250.68
	Annealed	54.773	84.08	125.03	145.58	181.53	202.76
	Fused quartz	56.628	83.674	122.35	153.36	182.61	207.47
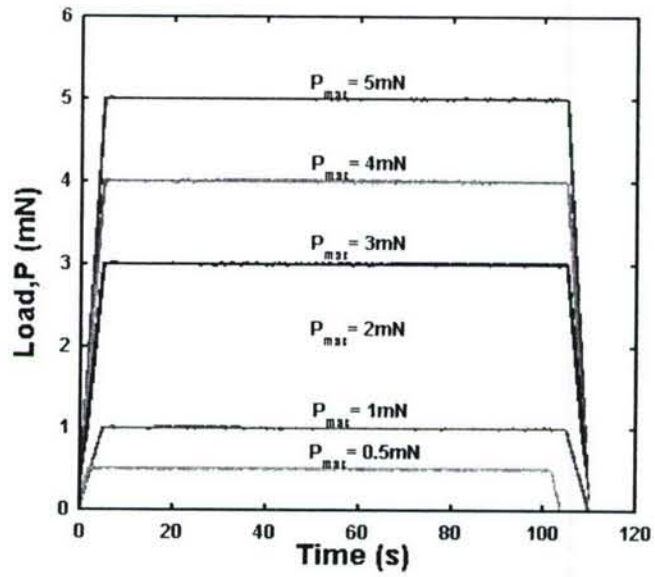
Fig.5.1. Load scheme of the indentation load relaxation (ILR) experiments.
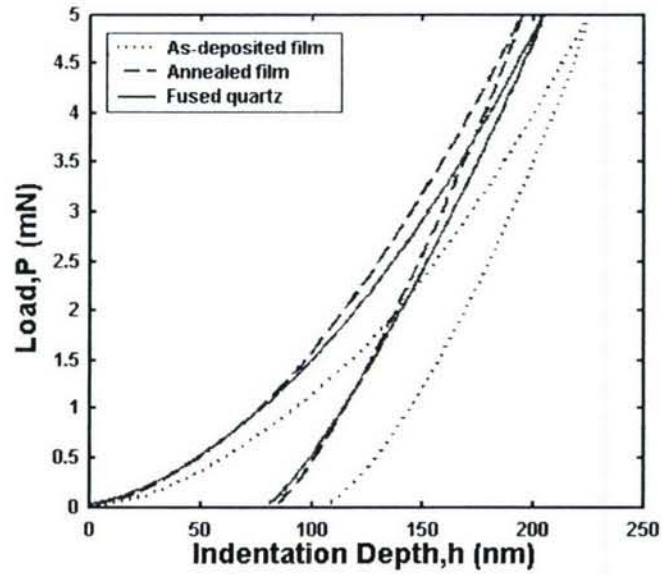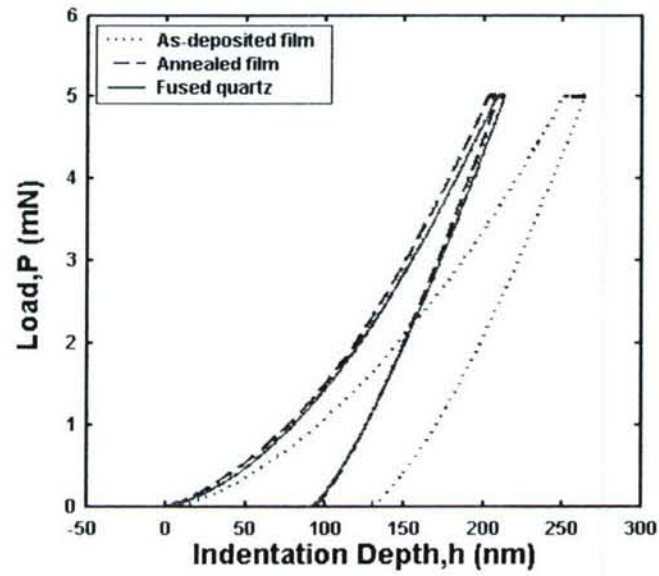
Fig.5.2. Load-displacement (*P-h*) relations of the (a) constant rate of loading (loading/unloading times: 2s) and (b) indentation load relaxation experiments with a maximum load (P_{max}) of 5 mN.
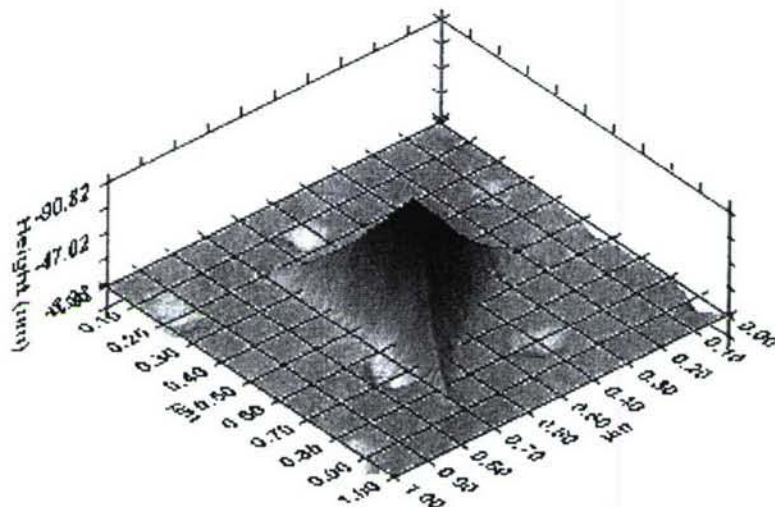
Fig.5.3. A complete (inverse) 3D image showing the curvature of the faces after an indent on the standard fused quartz sample (ILR experiment, P_{max}=5 mN).

(a)

(b)

(b)
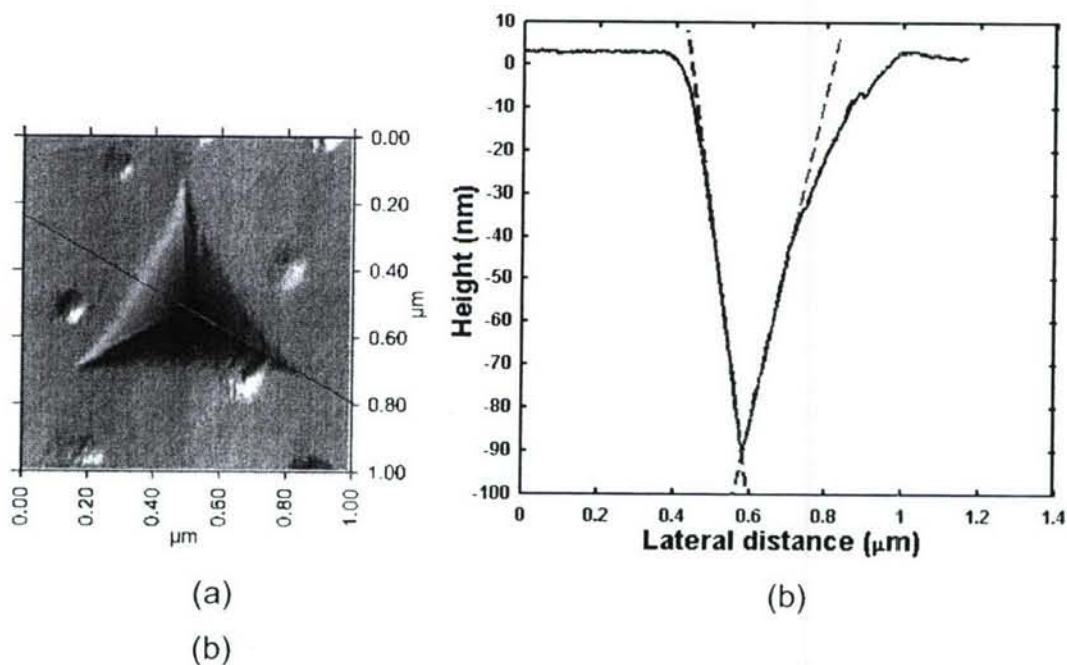
Fig.5.4. (a) The 3-D top view and (b) cross section line profile (through an edge and opposing face) of indent on the standard fused quartz sample (ILR experiment, P_{max}=5 mN).

112
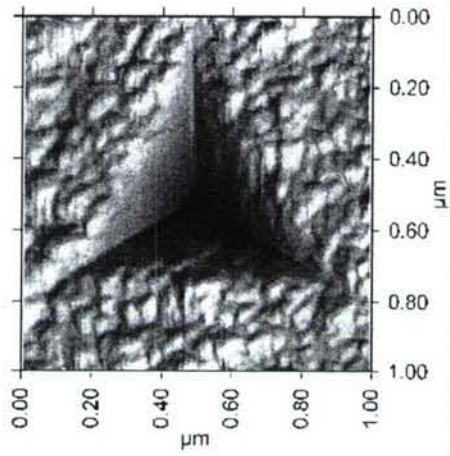
(a)
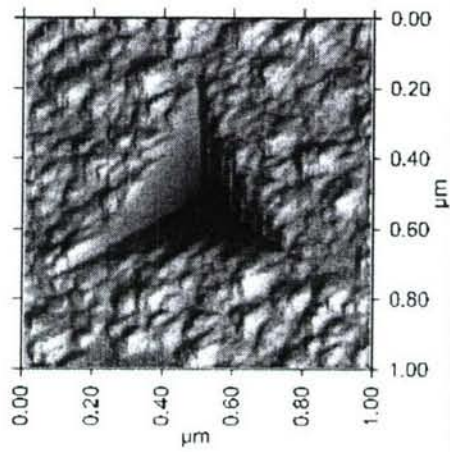
(b)

Fig.5.5. *In-situ* SPM images of residual prints of (a) as-deposited and (b) annealed PECVD SiO$_x$ films (ILR experiment, P_{max}=5 mN).
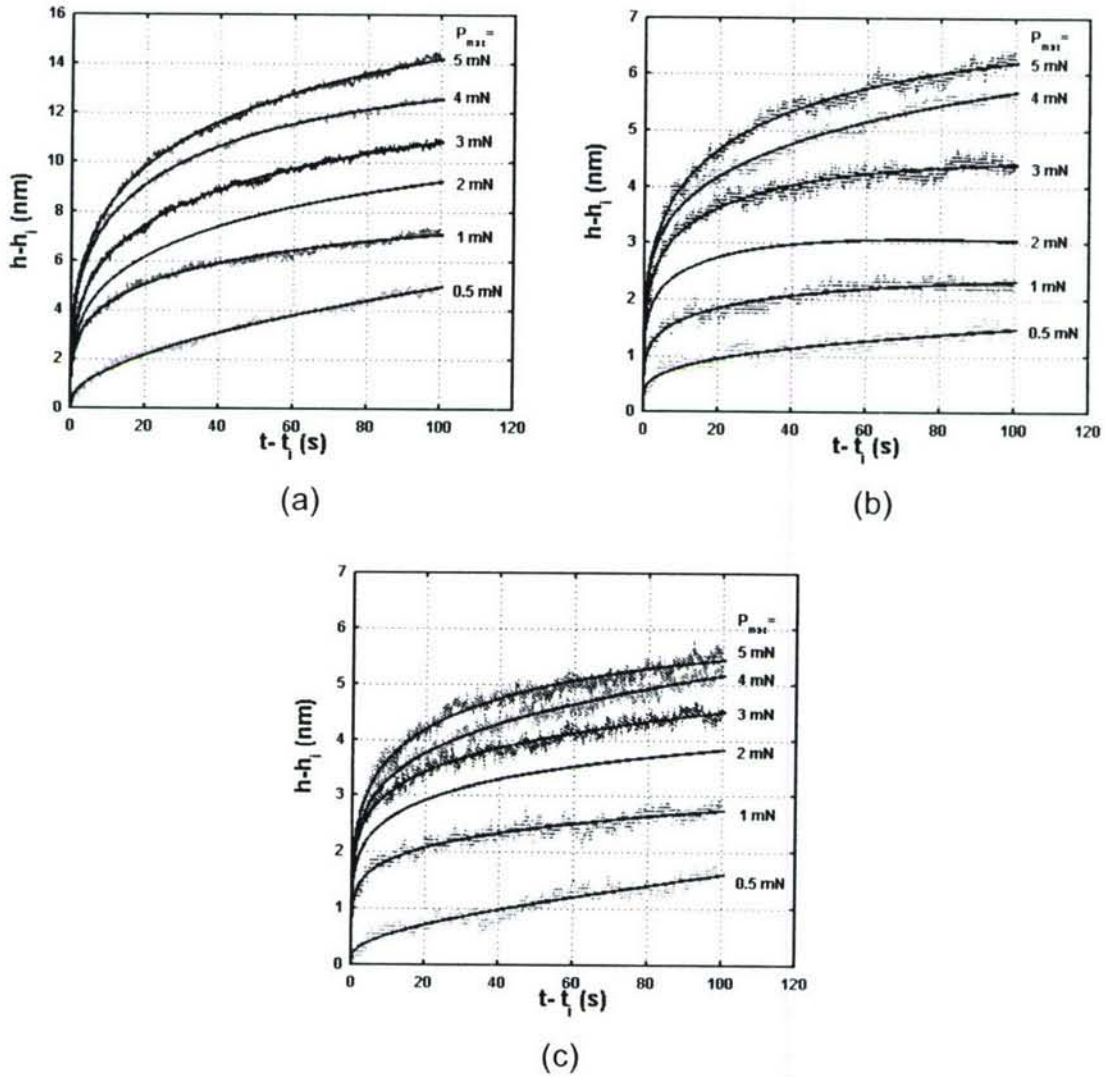
Fig.5.6. The experimental data (colored dots) and fitting (black lines) of the creep displacement (h-h_i) vs. hold time (t-t_i) relations of (a) the as-deposited PECVD SiO$_x$ film (b) annealed PECVD SiO$_x$ film, and (c) fused quartz under different peak loads (P_{max}).
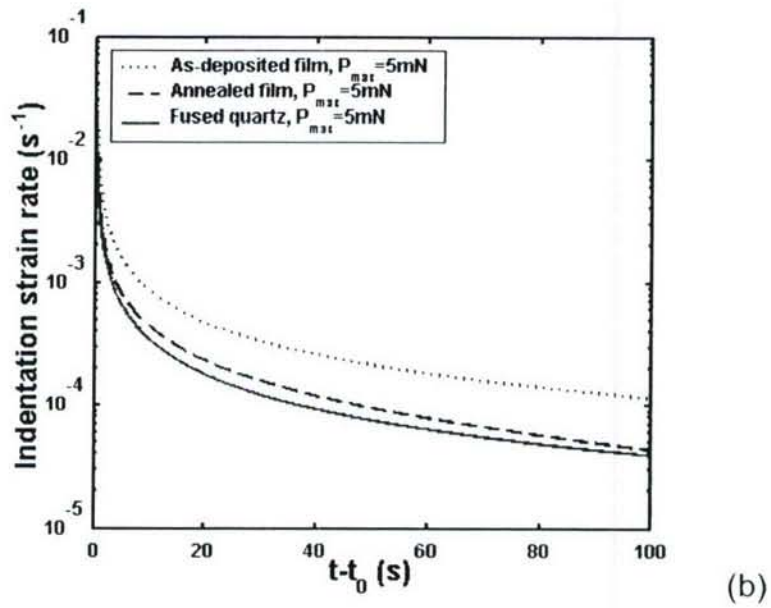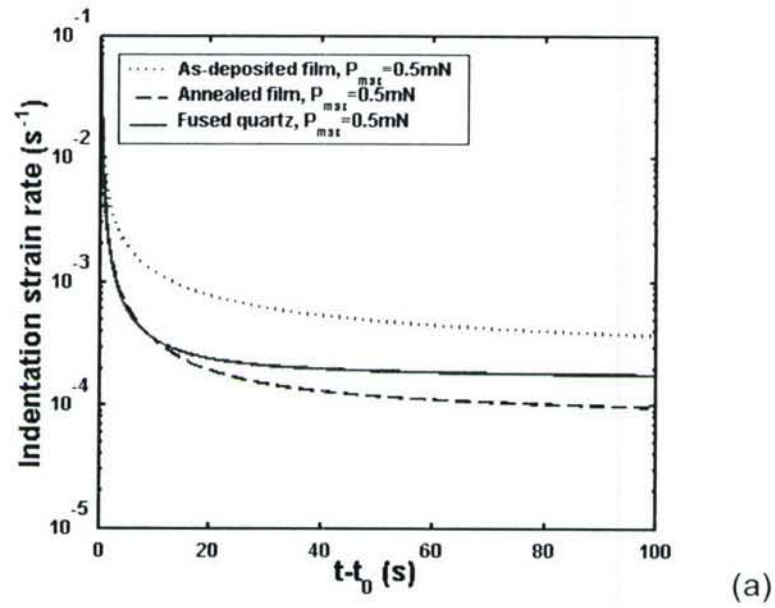
Fig.5.7. The $\dot{\varepsilon}_I \sim (t - t_0)$ (indentation strain rate vs. creep time) relations of the three sample materials under (a) 500µN and (b) 5mN constant peak loads.
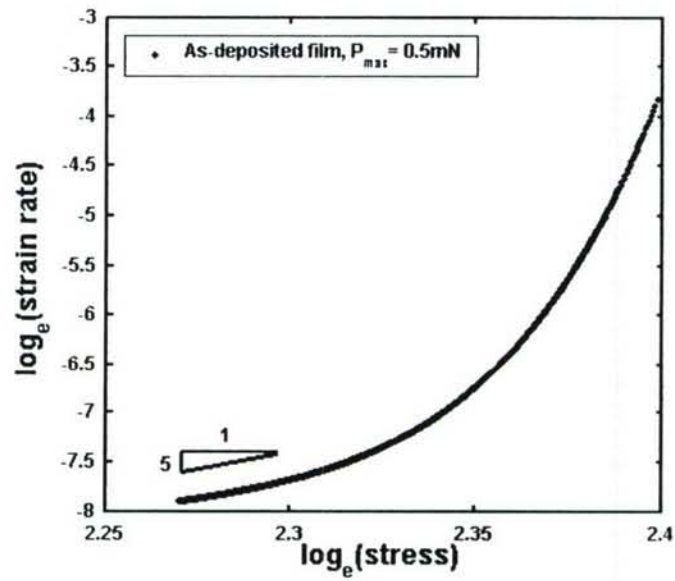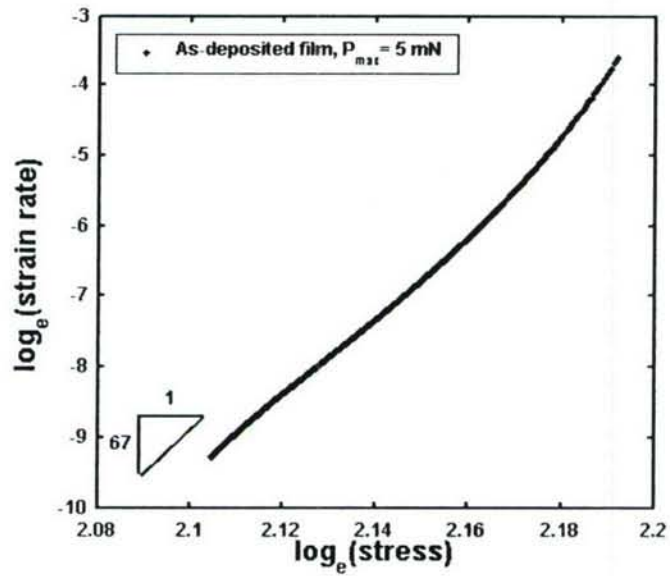
Fig.5.8. The $\log \dot{\varepsilon}_I - \log \bar{\sigma}$ relations of the as-deposited films under (a) 500μN and (b) 5mN constant peak loads.
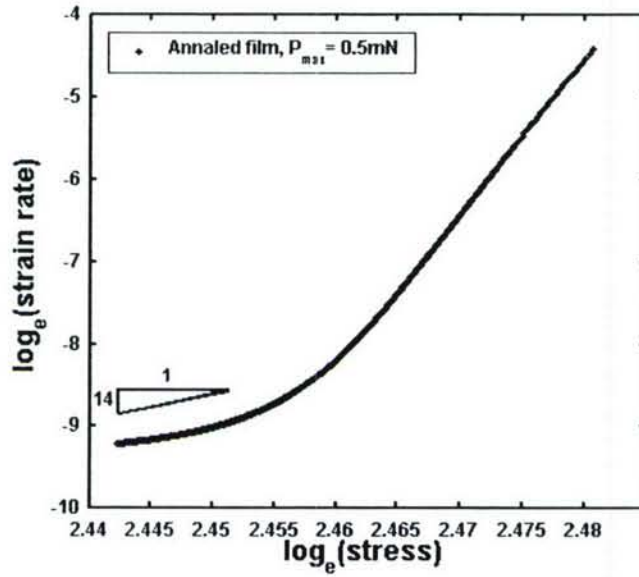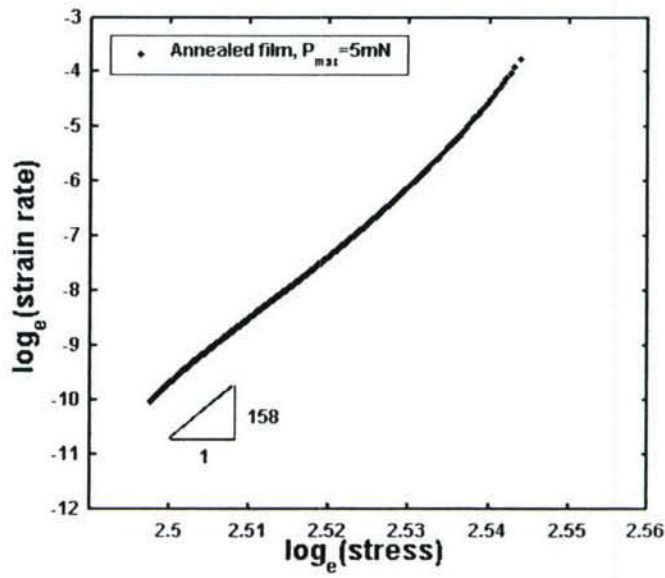
Fig.5.9. The $\log \dot{\varepsilon}_I - \log \bar{\sigma}$ relations of the annealed films under (a) 500μN and (b) 5mN constant peak loads.
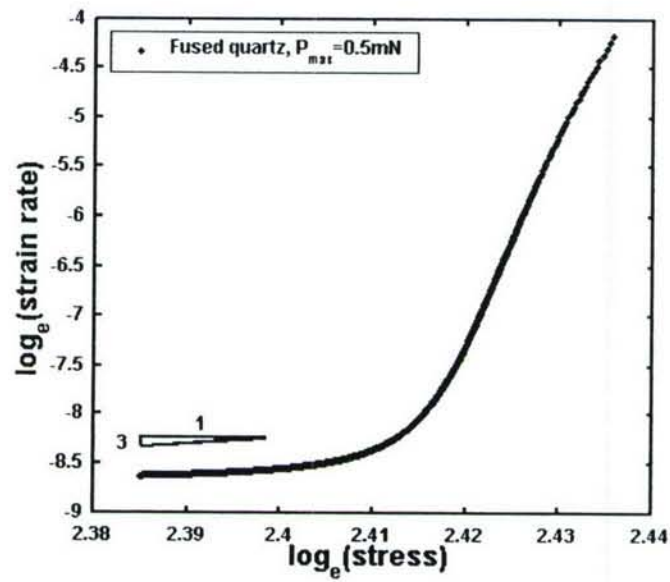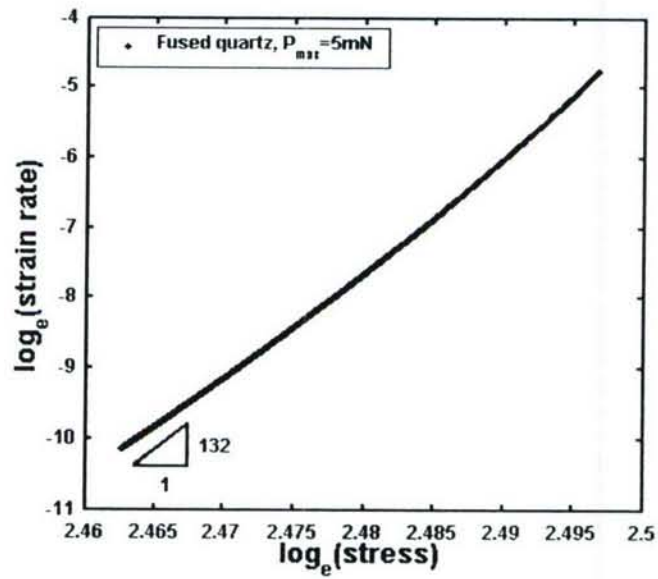
Fig.5.10. The $\log \dot{\varepsilon}_I - \log \bar{\sigma}$ relations of the fused quartz under (a) 500μN and (b) 5mN constant peak loads.

118
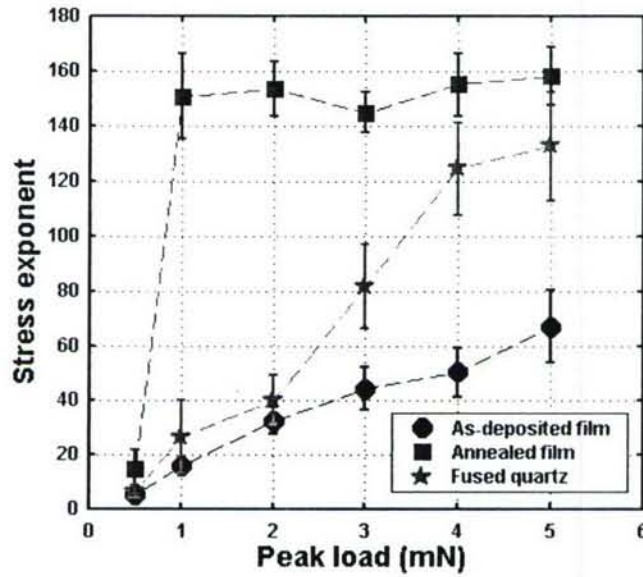
Fig.5.11. Steady-state stress exponent as a function of peak loads for different sample materials.
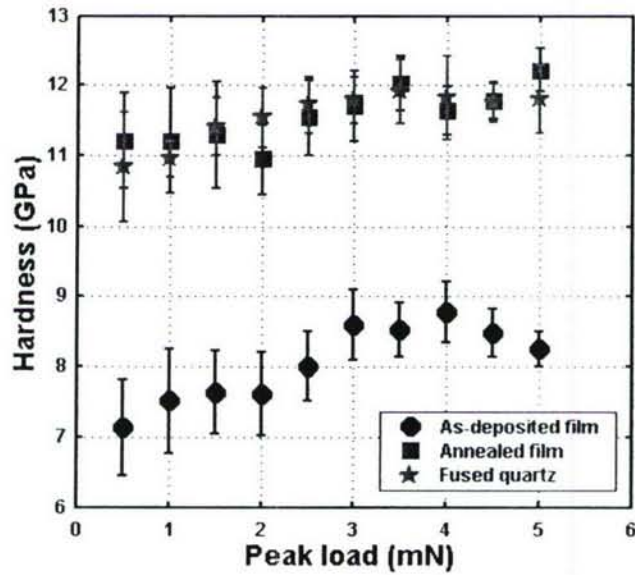
Fig.5.12. Hardness values of different sample materials under various peak loads.
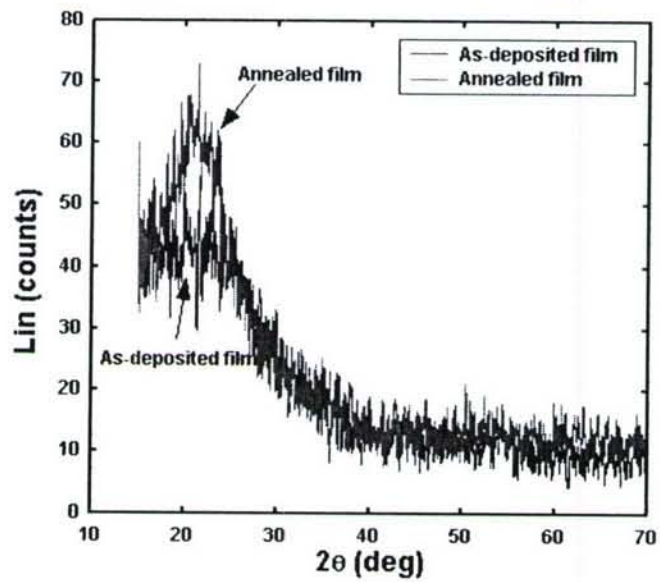
Fig.5.13. X-ray diffractograms for both the as-deposited and 800°C RTA annealed PECVD SiO_x thin film samples.

6. THERMALLY-INDUCED STRUCTURAL RELAXATION

Abstract: The structural relaxation of PECVD SiO_x films during thermal cycling and annealing has been studied using wafer curvature measurements. These measurements, which determine stress in the amorphous silicon oxide films, are sensitive to both plastic deformation and density changes. A quantitative case-study of such changes has been done based upon experimental results. A microstructure-based mechanism elucidates "seams" as a source of density change and "voids" as a source of plastic deformation, accompanied by viscous flow. This theory was then used to explain a series of experimental results that are related to thermal cycling as well as annealing of PECVD silicon oxide films including stress hysteresis generation and reduction, and coefficient of thermal expansion (CTE) changes. In particular, the thickness effect was examined; PECVD silicon oxide films with a thickness varying from 1 to 40 μm were studied as certain demanding applications in MicroMechanicalElectrical Systems (MEMS) require such thick films serving as heat/electrical insulation layers.

6.1. Introduction

As introduced in Sec.1, the deposition of thin films is one of the most important and technically challenging processes in the fabrication of semiconductor microelectronic devices and MicroElectroMechanical Systems (MEMS) (Madou 2002). Thin films, in general, have properties different from their bulk counterparts (Ohring 1992; Freund and Suresh 2004). Plasma enhanced chemical vapor deposition (PECVD) is a special chemical vapor deposition (CVD) process that is facilitated by RF plasma. It enables dielectric films such as oxides, nitrides, and oxynitrides to be deposited at relatively low temperatures (300~400°C) on devices that are unable to withstand high temperatures of a thermally activated reaction (Madou 2002). Because of its fast

deposition rate, normally ~1µm/min, it is also the only practical technique to deposit dielectric films with a thickness greater than a few microns.

PECVD silicon oxide (SiO_x) films have been widely used not only as dielectric layers but also as mechanical components in MEMS. A good example is its application in the so-called Power MEMS, an important class of MEMS devices designed to generate electrical and mechanical power (Nguyen 1999; Mehra et al 2000; Wong et al 2004). These devices (i.e., micro-scale high power-density heat engines and related components including, for example, micro combustors, micro heat exchangers, micro igniters, micro motor compressors, etc.) typically use PECVD SiO_x as electrical and thermal-mechanical insulation layers. To push electrical and mechanical powers to high performance levels, thick (typically in the range of 10-40 µm) PECVD SiO_x films are being used. However, the ability to utilize such SiO_x films with a thickness greater than a few microns is significantly limited by the residual stress generated during deposition and post-deposition thermal processing. It is therefore important to understand the thermal-mechanical properties of PECVD SiO_x films, especially thick films, which are less studied and more problematic.

Previous studies have shown that many amorphous materials, including PECVD SiO_x, exhibit irreversible property changes when heated to temperatures below what is required for recrystallization (Volkert 1993; Thurn and Cook 2002, 2004; Chen et al 2003). For PECVD SiO_x films, both stress hysteresis generation and reduction phenomena were demonstrated and explained (Thurn and Cook 2002, 2004; Chen et al 2003). This section is intended to provide a comprehensive investigation of the mechanical response and property changes of PECVD SiO_x films in three distinct temperature regions: below glass transition temperature, around glass transition temperature, and above glass transition temperature. In particular, the effect of thickness on stress hysteresis and the coefficient of thermal expansion (CTE) is examined. Films with a thickness of 1-40 µm are studied. Density and viscosity changes during thermal cycling and

high temperature annealing are also analyzed. These changes are direct evidence that the microstructure of PECVD SiO_x films undergoes irreversible changes during thermal processing. These changes also contribute to the better understanding of thermal-mechanical issues concerning the PECVD SiO_x films. Also, these results provide insight into the analysis of similar responses of other CVD materials (such as SiN_x), physical vapor deposited (PVD) materials (such as AlO_x), and low-k silsesquioxane-based materials (Thurn and Cook 2002).

6.2. Experimental Details

Silane-based PECVD SiO_x films were deposited using the conditions detailed in Sec.2.2.1. All PECVD SiO_x films were deposited on 525 μm thick <100> silicon wafers with the initial wafer bow in the range of 8 to 12 μm and thicknesses in the range of 1 to 40 μm. On each wafer, the film thickness has a non-uniformity of less than 1%. However, there is a less than 3% reduction in thickness across the wafer if a film is subjected to any further thermal cycling and/or annealing at temperatures higher than the deposition temperature, i.e., 400°C. In this study, in $situ$ wafer curvature measurements were performed between room temperature (RT) and 500°C using a commercial KLA-Tencor^{TM} FLX-2320 system with a ramp rate of 5°C/min. In this system, curvature was measured by directing a laser at a surface with a known spatial angle. The reflected beam stroke a position sensitive photodiode. The geometry of the film was recorded by scanning the surface. Measurement accuracy was less than 2.5% or 1 MPa, whichever was larger, for a typical (100) Si wafer with 1 μm thick film and 80 mm scanning length. The wafer was heated in a controlled atmosphere of Nitrogen or Argon, and temperature changes were controlled at up to 30°C/min in the range of room temperature to 500°C.

For higher peak cycling temperatures that are above 500°C, a Bruce Technology high temperature furnace was used in this study. Since this furnace

does not have an *in situ* curvature measurement capability, curvature measurements could only be performed after a complete thermal cycle. A ramp rate between 0.5°C/min (near peak temperature) and 10°C/min (below deposition temperature) was used in this furnace. In addition, a 30-minute stabilization period was performed at the peak temperature to simulate the annealing period during fabrication and to examine the possibility of stress relaxation. Observations of cracks and curvature were made after each cycle.

The measured curvatures were subsequently converted to film stress using the following Stoney's equation (Stoney 1909):

$$\sigma_f = \frac{E_s t_s^3}{6(1-v_s)Rt_f^2(1+t_s/t_f)}$$
(Eq. 6.1)

where *1/R* is the curvature, t_s and t_f are the thickness of the substrate and the film, respectively. E_s and v_s are Young's modulus and Poisson's ratio of substrate. Since usually $t_s \gg t_f$, this equation can be simplified as:

$$\sigma_f = \frac{E_s t_s^2}{6(1-v_s)Rt_f}$$
(Eq. 6.2)

Stoney equation Eq.(6.1) was derived from linear elasticity theory, and was installed in the testing system for data conversion. However, it should be emphasized that this equation does not account for the effect of geometrical nonlinear deformation and offset of the neutral plane. Although the Stoney equation works well when $t_s \gg t_f$ and deformation of the wafer is small, significant errors can occur either if the rigidity of the film is not much less than that of the substrate or if the wafer undergoes large deformation. If the ratio of t_f/t_s increases, the wafer more easily undergoes large deformation. As a result, stress is usually underestimated for thick films. For example, when the ratio of film thickness and substrate thickness is around 0.02 (in our case, film thickness is around 10 μm; substrate thickness is 525 μm), the range of error of Eq.(6.2) is around 5% (Chen and Ou 2002).

There have been many sections on improving the accuracy of Stoney's equation in specific applications (Chen and Ou 2002; Tsui and Clyne 1997; Weinberg 1999; Salamon and Masters 1995). In this section, we modified our experimental data by nonlinear finite element analyses using ABAQUS and a semi-analytical formulation developed by Chen et al (Chen and Ou 2002). This formulation is based on the energy method and simultaneously considers effects of geometrical nonlinearity and mid-plane offset. With an appropriately assumed deformation shape, analytical solutions obtained by this method have a good agreement with highly meshed finite element simulation results (Chen and Ou 2002).

6.3. Experimental Results.

6.3.1. Stress hysteresis generation and reduction

Thurn and Cook (2002, 2004) previously demonstrated stress hysteresis phenomena for PECVD SiO_x films with a constant thickness of around 1 µm and with varying peak cycling temperature of 100~400°C. In addition to previous results, we studied the influence of film thickness on the hysteresis, and increased the peak cycling temperature to 500°C. Six PECVD SiO_x films with different thicknesses of 1, 3, 6, 10, 20, and 40 µm were deposited under conditions described in Sec. 6.2, and for each of them, multiple thermal cycling experiments with peak temperatures up to 500°C were preformed. These experimental results were then summarized and compared to study the influence of thickness on stress hysteresis.

Representative thermal cycling results of film stress~temperature relationship, for 10 µm and 40 µm films respectively, are shown in Fig.6.1. Here, we define stress hysteresis as the difference between ending stress (σ_e) in the film and the as-deposited stress, or starting stress (σ_s) in the film, i.e., Stress Hysteresis = σ_e- σ_s. Starting and ending temperature of the thermal cycling are

the same here, and both are around room temperature. Fig.6.2 (a) shows as-deposited film stress as a function of film thickness before and after 500°C thermal cycling. The corresponding stress hysteresis of SiO_x films is shown in Fig.6.2 (b). Large, positive (tensile) stress hysteresis was observed during the first thermal cycling for all films with the thicknesses varied from 1 to 40 μm. However, the magnitude of this hysteresis was found to first increase (between 1~3 μm) and then decrease (between 3~40 μm) with increasing film thickness. The stress hysteresis, not surprisingly, is closely related to its as-deposited stress σ_s. Additionally, as Fig.6.1 shows, during subsequent thermal cycling, this hysteresis was reduced to virtually zero, although it took thicker films more cycles to eliminate the hysteresis. For comparative purpose, Table 6.1 tabulates the values of σ_s, σ_e, and stress hysteresis σ_e- σ_s of the first three cycling of as-deposited 10 μm and 40 μm PECVD SiO_x films. Note that for the 10 μm film, the additional hysteresis in both the second and third cycling is negative (i.e., more compressive), while for the 40 μm film the additional hysteresis in the second and third cycling is positive (i.e., tensile).

After the first thermal cycling, the stress-temperature relation became almost linear and reversible, indicating an elastic response. It is believed that this hysteresis was initially generated by intrinsic (or growth) stress during PECVD deposition. During the subsequent thermal cycling, structural relaxation took place, and caused irreversible microstructure changes that changed the thermal mechanical properties of the films. In particular, it can be inferred that local bonding, especially highly strained bonds, underwent significant changes due to heating/cooling in the thermal cycling. There seemed to be two stress controlling mechanisms here, as the stress hysteresis was positive in some cases and negative in others. This will be discussed in more detail later in the section.

6.3.2. Coefficient of Thermal Expansion (CTE)

126

The reversible stress change measured during thermal cycling is due to the difference between the thermal expansion coefficients (CTE) of the PECVD SiO_x film (α_f) and crystalline silicon substrate (α_s). CTE of the film, α_f can be calculated from the slope of "Film Stress vs. Temperature" curve based on following equation (Volkert 1993; Thurn and Cook 2002):

$$\frac{d\sigma_f}{dT} = \frac{E_f}{(1-v_f)}(\alpha_s - \alpha_f),\qquad\qquad \text{(Eq. 6.3)}$$

where $Y_f = E_f/(1-v_f)$ is the biaxial stress state modulus of the PECVD SiO_x film. Eq.(6.3) is simply the derivative form of the expression of thermal stress in homogeneous bilayer structures (Madou 2002; Ohring 1992) In order for this equation to be applicable, both α_f and α_s are assumed to be uniform throughout the film and substrate, respectively.

It was previously reported (Thurn and Cook 2002, 2004) that, for 1.08 µm thick PECVD SiO_x film, its CTE decreased from what was immeasurably different from that of Si (3.0 ppm $°C^{-1}$) to 1.5 ppm $°C^{-1}$ as the peak cycling temperature increased from 100°C to 400°C. Nanoindentation tests indicated that when peak thermal cycling temperature increased from 100°C to 400°C, Young's modulus of PECVD SiO_x film (76.4±2.1 GPa) after thermal cycling varied within less than 3% (Thurn and Cook 2002). Assuming the same Young's modulus (76.4 GPa) and Possion's ratio (0.17), we found that the CTE of 1 µm thick PECVD SiO_x film decreased to 0.23 $ppm°C^{-1}$ under 500°C thermal cycling, less than that of bulk SiO_2 (0.5 ppm $°C^{-1}$). Fig.6.3 gives a comprehensive result of CTE of the PECVD SiO_x films with 1 to 40 µm in thickness during the first 500°C cycling ramp down. CTE was calculated from the linear part during ramp down. As can be seen, the CTE first decreased slightly with thickness when the film was less than 3 µm then increased significantly from 0.5 ppm $°C^{-1}$ to 2.0 ppm $°C^{-1}$ when film thickness was 3 µm or above. This behavior indicates, again, a thickness-dependent change in its microstructure. In addition, we found that for thicker films during subsequent thermal cycling, the CTE of the film decreased noticeably for films thicker than a

few microns. For example, for a 10 µm thick PECVD SiO_x film, its CTE decreased from 0.57 ppm $°C^{-1}$ to 0.33 ppm $°C^{-1}$ to 0.24 ppm $°C^{-1}$ from the 1st to the 2nd and to the 3rd cycling, respectively. For a 40 µm thick PECVD SiO_x film, the CTE decreased from 2.02 ppm $°C^{-1}$ to 1.163 ppm $°C^{-1}$ to 0.913 ppm $°C^{-1}$ from the 1st to the 2nd and to the 3rd cycling, respectively.

Since the CTE of the film is closely related to the microstructure of the material, the CTE changes in the films provide direct evidence that microstructural changes took place in the PECVD SiO_x films during thermal cycling. We will discuss more about it later in the section.

6.3.3. Density and viscosity changes

As mentioned before in Sec. 6.3.1, the large stress hysteresis observed during thermal cycling of PECVD SiO_x films is due to the structural relaxation. There are two possible contributions that cause the stress to change during relaxation: irreversible changes in the density of PECVD SiO_x films and plastic deformation due to the stress in the films. Both density changes and plastic deformation will result in microstructure changes in the films, which account also for CTE changes of the films in Sec. 6.3.2.

Plastic deformation during thermal cycling is stress-dependent and can only reduce the magnitude of stress. For PECVD SiO_x films with thickness of 10 µm or less, during the 2nd thermal cycling, an additional small, yet positive, hysteresis was observed. Since this hysteresis is an increase to the magnitude of stress, this indicates a change in film density. In order to obtain quantitative information about such density changes during thermal cycling, the contribution from plastic deformation and its dependence on stress must be determined. By definition, thermal strain in the film $\varepsilon = \sigma_f / Y_f$ and thermal cycling heating/cooling rate $\phi = |\Delta T / \Delta t|$, where $Y_f = E_f / (1 - v_f)$ the biaxial modulus of the film, T is the cycling temperature, and t is the time. The strain rate for a given film and

temperature can therefore be obtained by taking the derivative of the stress-temperature curves

$$\frac{d\varepsilon}{dt} = \frac{\phi}{Y_f} \frac{d\sigma_f}{dT} \text{ (ramp up), and } \frac{d\varepsilon}{dt} = -\frac{\phi}{Y_f} \frac{d\sigma_f}{dT} \text{(ramp down)} \qquad \text{(Eq. 6.4)}$$

Strain rate can be also expressed as (Volkert 1993; Lubliner 1990):

$$\frac{d\varepsilon}{dt} = -\frac{1}{3} \frac{d(\Delta\rho/\rho_0)}{dt} - \frac{\sigma_f}{6\eta} \qquad \text{(Eq. 6.5)}$$

where the first term on the right-hand side is the temporal stress-independent (but time dependent) elastic term, accounting for density changes $\Delta\rho/\rho_0$; the negative sign means that when density decreases (volume expansion), strain rate increases (stress tends toward more tensile). The second term is proportional to the stress, accounting for viscous flow with effective viscosity η; the negative sign means that the viscous flow will always reduce the magnitude of the stress. Combining Eq.(6.4) and Eq.(6.5) yields:

$$\frac{d\sigma_f}{dT} = -\frac{Y_f}{\phi}(\frac{1}{3} \frac{d(\Delta\rho/\rho_0)}{dt} + \frac{\sigma_f}{6\eta}) \text{ (ramp up)} \qquad \text{(Eq. 6.6)}$$

From Eq.(6.5) and Eq.(6.6) we can clearly see that stress, especially non-thermal stress, in the films is sensitive to both density changes and plastic deformation, which is accompanied by viscous flows. To evaluate which factor is more dominant, we need to study them quantitatively. In our experiments, we case-studied the viscous flow effect of an as-deposited 10 μm PECVD SiO_x film. First, we measured its film stress relaxation at constant 500°C annealing, as illustrated in Fig.6.4. To the 1st order approximation, assuming a constant density change rate at 500°C, we can have an equation for relaxation by integrating over both sides of Eq.(6.6)

$$\sigma_f(t) = \sigma_0 \exp(-\frac{Y_f}{6\eta}t) \qquad \text{(Eq. 6.7)}$$

where σ_0 is the starting stress. The time constant for stress relaxation, t, is equal to $6\eta/Y_f$. The fitting of Fig.6.4 gives us:

$$\sigma_f(t) = 46.5 + 17.5\exp(-t/1200) + 9\exp(-t/6000) \text{ (MPa)} \qquad \text{(Eq. 6.8)}$$

This actually means that multiple viscoplastic flows took place, and the first and second order waves with most significant amplitudes have a relaxation time constant t of 1200 seconds (20 minutes) and 6000 seconds (1 hour 40 minutes), respectively. Equivalently, they have a viscosity of 1.8×10^{13} Ns/m^2 and 9.2×10^{13} Ns/m^2, respectively. For PECVD SiO$_x$, viscosity near glass transition temperature is around 10^{12} Ns/m^2, corresponding to a relaxation time of around 1 minute. So, from the viscosity and stress relaxation time constant we can tell that at 500°C, the 10 µm PECVD SiO$_x$ film is still not near glass transition temperature, and plastic flow should not play a significant role in the stress relaxation. We know that at lower temperatures, the viscosity of the material is higher. Therefore the major contribution that causes the stress to change during relaxation during 500°C thermal cycling is from density changes. Now we can obtain some quantitative information about the density changes.

The film stress and temperature relation during heating period of the first cycling of 10 µm PECVD silicon oxide can be found in Fig.6.1 (a). The slope of that $\sigma_f \sim T$ curve, $d\sigma_f/dT$, rises sharply after 400°C but falls close to 500°C, shown in Fig.6.5. We can also draw the same $d\sigma_f/dT$ as a function of σ_f as shown in Fig.6.6. We already know from Eq.(6.6) that, no matter whether film stress is compressive (-) or tensile (+), plastic flow will cause a decrease in the slope of $d\sigma_f/dT \sim \sigma_f$. An increase in its slope indicates a decrease in density, i.e., $d(\Delta\rho/\rho_0)/dt$ (at T) < 0. Therefore it is clear from Fig.6.5 and Fig.6.6 that during heating to 500°C, both plastic flow and density changes are happening. However, the greater reduction in stress, and later the positive hysteresis generation, is mainly caused by density changes in the films. This is consistent with the fact that viscosity is high for 10 µm PECVD SiO$_x$ film below 500°C. As temperature gets higher, close to 500°C, plastic flow became more dominant. First, it annihilated the density-changes effect, reflected by a plateau in the curve,

and then caused a change in sign of the slope for both $d\sigma_f / dT \sim T$ and

$d\sigma_f / dT \sim \sigma_f$ curves. When $\sigma_f \sim 0$, $\dfrac{d(\Delta\rho/\rho_0)}{dt} = -\dfrac{3\phi}{Y_f}\dfrac{d\sigma_f}{dT} - \dfrac{\sigma_f}{2\eta} \approx -\dfrac{3\phi}{Y_f}\dfrac{d\sigma_f}{dT}$, or

$$\frac{d(\Delta\rho/\rho_0)}{dT} = -\frac{3}{Y_f}\frac{d\sigma_f}{dT} \qquad\qquad\qquad \text{(Eq. 6.9)}$$

From Fig.6.6, $d\sigma_f / dT \approx 1.7$ (MPa/°C) when $\sigma_f \sim 0$, therefore, it corresponds to

$d(\Delta\rho/\rho_0)/dT \approx -5.5\times10^{-5}$ (/°C). Considering that most of the densification happened between a temperature range of around 500°C, we can estimate that the magnitude of density change during the 1st cycling of 10 μm thick PECVD SiO$_x$ film is around -0.3%. In other words, at the end of the temperature ramp up of the first thermal cycling, or 500°C, the volume of the SiO$_x$ film expanded approximately 0.3% as compared to room temperature. Density change and viscous flow account for non-thermal stress changes in the films, not only for PECVD SiO$_x$ films, but also for any other films that have shown similar mechanical responses. We will later discuss the relation between the microstructure of the films and the specific density or viscosity changes, and apply this insight for understanding other experimental results, such as stress hysteresis, CTE changes, annealing effects, and their dependence on film thickness.

6.3.4. Effect of thermal annealing

High temperature annealing has been commonly adopted to improve the electrical performance of PECVD oxide films. However, in this study, our emphasis is on the structural relaxation phenomena instead of the electrical property changes during annealing. In this study, specimens were put in furnaces with various peak annealing temperatures for 30 minutes or longer to be totally relaxed. Film curvature and stress were then measured after they cooled down to room temperature. Fig.6.7 shows that for a 40 μm thick PECVD SiO$_x$ film, stress hysteresis of the 1st cycle was reduced significantly with 30 minutes

annealing at 500°C. During the 2nd cycling, additional hysteresis was also greatly reduced, and it had a different sign with the specimen without 500°C 30-minute annealing. This is mainly because, during the annealing, plastic flow relieved part of the total tensile stress, thus later the stress hysteresis was reduced in magnitude. Further results, reflected in Fig.6.8, show that during subsequent cycling at higher peak temperatures of up to 1100°C, the films became more compressive. For the same peak annealing temperature, however, the film that was previous annealed at 500°C experienced less positive hysteresis, although this difference was diminishing with increasing peak annealing temperature. This is also because, during 500°C annealing, plastic flow reduced the magnitude of the stress. For un-annealed film, the hysteresis peaked at around 700°C and then became more and more compressive. This reflected an increasing volume change rate in the film and showed the glass transition temperature for un-annealed film is around 700°C. After this temperature, the volume/density change rate became steady, and plastic flow dominated the hysteresis generation. Results of annealing for as-deposited films with various thicknesses are shown in Fig.6.9. It is clear that significant film hysteresis occurred just after 400°C, the deposition temperature. This reduction, as discussed before, is mainly caused by the expansion of volume. From 600 to 700°C, increased stress-dependent plastic flow almost canceled the volume expansion effect, and we observed a virtual stop in the increase of hysteresis. As the peak annealing temperature rose above 700°C, the densification process became dominant, and the volume expansion rate reduced. As a result, the magnitude of hysteresis quickly reduced and as the temperature got closer to 1000°C, hysteresis was reduced so much that its original sign was changed from positive to negative. 700°C and 1100°C, therefore, seem to be two important boundary temperatures for as-deposited PECVD SiO_x films. They set the thermal mechanical behavior of such films into three distinct regions. We will discuss later how to interpret this result in terms of material microstructural changes.

6.4. Discussion

Nearly all films have residual stresses. The common causes include: CTE mismatch, non-uniform plastic deformation, lattice mismatch, impurities, and growth processes. Specifically, the PECVD process is a fast deposition process, with a deposition rate of 1 μm/min or higher, but the deposition temperature is relatively low, which means mobility of the atoms is low. Additionally, there is plasma bombardment and product gas incorporation. As a result, compared with other growth methods, such as LPCVD (Low Temperature Chemical Vapor Deposition) or Thermal Growth, a greater number of atoms are not in positions where their potential energy is minimized. This means a lot of bonds are either distorted or dangling, forming defects and causing intrinsic, or growth stress in the films.

The above-mentioned defects fall into two types:

1) Seams. In this project, seams refer to bonds that are compressed, or shorter than their normal length. Hydrogen incorporation and the forming of Si-OH···HO-Si bonds may contribute to the generation of seams. Another possibility is that some of the Si-O-Si bonds are also compressed. Our previous Second Ion Mass Spectroscopy (SIMS) analysis, plotted in Fig.6.10, showed that hydrogen content in the as-deposited films is significant for our deposition parameters (Chen et al 2003). The concentration of hydrogen atoms is higher (~6.7%) near the free surface than the interior (~2%), about 500 nm from free surface. During thermal cycling to higher temperatures, weak Si-OH···HO-Si bonds will be broken and Si-O-Si bonds will be re-formed (Thurn and Cook 2002). The SIMS result showed that for thicker films, the average seams density would be less.

Seams are the source for generation of compressive intrinsic stress. For bonds that are compressed, during heating to higher temperatures than the deposition temperature, significant reduction in the compression is expected. This is simply because the bonds are now less distorted as the bond lengths are increased. Macroscopically, this process is accompanied by volume expansion, or an increasing volume rate $d(\Delta V/V_0)/dt$, or equivalently a decreasing density rate $d(\Delta \rho/\rho_0)/dt$. In other words, seams reduction is accompanied by the *thermal softening* process. According to the first term of Eq.(6.5), this will contribute to a positive increase in strain rate $d\varepsilon/dt$. However, as this volume expansion requires thermal energy, and is non-equilibrium in nature, during cooling there is no reverse of the expansion rate. So, it will contribute to the hysteresis generation.

2) Voids. Here voids refer to bonds that are dangling or stretched, i.e., bonds that are longer than their normal length; note that extra spacing caused by stretched bonds is also termed "voids" here. Voids are the source of generation of tensile stress. Amorphous SiO_x can be depicted as a random three-dimensional network consisting of tetrahedra that are joined at the corners but share no edges or faces. In crystalline quartz the tetrahedra cluster in an ordered six-sided ring pattern (Ohring 1992). For PECVD SiO_x, during heating to higher temperatures, the loosely ordered atoms will be re-arranged to a relatively more orderly structure, and the density of the voids will be reduced. The result is that the microstructure of the material will be an admixture of two structural extremes (totally amorphous and crystalline) possessing small, yet non-zero, short-range order. That is to say, the effective "grain size", which is zero for totally amorphous materials and infinity for crystalline materials, will increase during heating of the PECVD SiO_x films when there are an excessively large number of voids in the films. We know that the CTE tends to decrease when grain size increases (Eastman and Fitzsimmons 1995). Therefore, the decrease of CTE in the film indicates the reduction of the voids. From a plasticity point of

view, the reduction of voids happens in the form of the voids' movement, or diffusion under shear stress, which is the cause for plastic strain changes (Lubliner 1990). In other words, the reduction of the voids will cause an increase in plastic flow. It is apparent that for thinner films, voids can more easily diffuse to the free surface and be reduced by the coalescence during film growth (Muller 1985). So, for very thin films, the density of voids is lower. This leads to a less disordered structure for very thin films, which is the reason why, in Fig.6.3, the CTE of the films was generally lower when the thickness is below 3 μm. For amorphous material such as PECVD SiO_x films, under a given stress, the resolved shear stress varies from effective "grains"--short-range order atom groups-- to "grains". This means that we should expect no single viscosity for the plastic flow, rather the plastic flow is composed of multiple numbers of waves of different magnitudes and viscosities. In Sec. 6.3.3, we characterized such a plastic flow for a 10 μm thick PECVD SiO_x film annealed at 500°C.

Due to its amorphous nature, direct determination of the microstructure of stressed PECVD SiO_x films is a challenging job. Field Emission Scanning Probe Microscopy (FESEM), for example, was found to be inadequate for the task. Fig.6.11 (a) shows the FESEM image of the freshly cleaved side-surface an as-deposited 5 μm thick PECVD SiO_x film. It can be seen that near the free (top) surface, the surface is rough, indicating a poor quality of the film. Possibly, this could be a confirmation that the density of the "voids" is higher near the free surface, as discussed earlier. Further away (from the free surface), however, the topography of the side-surface is smoother, possibly indicating that the "voids" density is decreased. The FESEM image of the same film after annealing at 800 °C (for 10 min in a nitrogen environment) is shown in Fig.6.11 (b). The side-surface becomes so smooth that regardless of the probe or magnification, no clear topography profile can be imaged. This could also indirectly confirm that the film quality is enhanced and, as a result, the microstructure of the thin film

has become more orderly. This claim can also be independently verified by the XRD experiment in Sec.5.

To further enhance the previous discussions on property-structure relationships, other microstructure characterization techniques such as TEM (Transmission Electron Microscopy) (Zhu et al 1995; Min et al 1996; Gourbilleau et al 2001; Werwa et al 1994; Inokuma et al 1998; Iacona et al 2000) would be required in the future work. In particular, a special TEM technique named Energy Filtered Transmission Electron Microscopy (EFTEM) appears to be most promising (Iacona et al 2004). Recently, it was reported that silicon nanoclusters embedded in SiO_2 was produced by thermal annealing of PECVD SiO_x films, and EFTEM was successfully applied to investigate the structural properties of this system (Iacona et al 2004). This presence of a relevant contribution of amorphous nanostructures, not detectable by conventional dark field TEM, is also evidence that effective "grain size" increases during thermal annealing of PECVD SiO_x films.

In summary of above, the stress in the PECVD SiO_x films is controlled by the competition of two factors: "seams" and "voids". Equivalently, it is a competition between the thermal softening (i.e. seams reduction) and densification (i.e. voids reduction) processes. The balancing of the two will decide the strain change rate. For the 1st 500°C cycling, the structural relaxation was dominated by seams reduction, and consequently reduction of compressive stress in the films, which caused the tensile stress hysteresis. Note that, for films with a thickness less than 3 μm, the magnitude of the hysteresis was much reduced by the viscous flow, as shown in Fig. 6.2(b).

After the first cycling, seams were significantly reduced, and as a result, during subsequent cycling at the same peak temperature, the magnitude of stress hysteresis was reduced. When film thickness exceeded a certain threshold, voids reduction, or increased viscous flow became more significant in hysteresis generation. This is why we saw a negative hysteresis for the second

thermal cycling of 40 μm PECVD SiO_x film in Fig.6.1 and Table 6.1. The result of this added viscous flow effect in microstructure change was a more ordered SiO_x network. Therefore, in subsequent thermal cycling, there was a reduction in the film CTE.

Our thermal cycling experiments indicated that during thermal processing up to 500°C, stress in the PECVD SiO_x films will be mainly controlled by the seams, as viscosity of the SiO_x is high at this temperature. During heating to higher temperature, however, the viscosity of the film will be significantly lowered, due to the increased mobility of the voids. On the other hand, with increasing temperature, the bonds in the seams will become less and less distorted. So, the net result, shown in Fig.6.9, is that we will first see a stop in the increase of hysteresis generation, and then the hysteresis will become more and more negative, as is characteristic of result of viscous flow.

We end the discussion in section by noting that the above structural relaxation mechanism, based on "seams" and "voids", is inherently consistent with the shear transformation zone (STZ) and "free volume" based amorphous plasticity theories, referred to in Sec.4 and 5. Both "seams" and "voids" are microstructural defects that are the physical sources of the STZs, and their interaction and proliferation at high temperature (near or above T_g) and low stress is responsible for the Newtonian-viscous like flow behavior in the PECVD SiO_x.

6.5. Conclusions

Structural relaxation of silane-based PECVD SiO_x films during thermal cycling and annealing has been studied using wafer curvature measurements. Two factors, density change and plastic deformation, were identified as controlling mechanisms of stress changes in the films. A quantitative case-study of both density change and viscous flow has been done based upon

experimental results. It was found that for 10 μm thick PECVD SiO_x film under 500°C thermal cycling, the density decreased about 0.3% at peak temperature. Plastic flows with different viscosities and amplitudes were observed during annealing at 500°C. The viscosities of the waves with two most significant amplitudes were of 1.8×10^{13} Ns/m^2 and 9.2×10^{13} Ns/m^2, respectively. A microstructure-based mechanism relates defects during PECVD deposition to both density change and viscous flow. This mechanism elucidates "seams" as a source of density change and "voids" as a source of plastic deformation, accompanied by viscous flow. This mechanism was then applied to explain other experimental results of thermal cycling as well as the annealing of PECVD SiO_x films, including stress hysteresis generation and reduction, and the coefficient of thermal expansion (CTE) changes.

Table 6.1. Stress hysteresis of 10 μm and 40 μm as-deposited PECVD SiO_x films subjected to three 500°C thermal cycling's.

	Film Thickness	Starting Stress σ_s (MPa)	Ending Stress σ_e (MPa)	Hysteresis σ_e- σ_s (MPa)
1st 500°C	10μm	-129.6	-42.0	87.6
Thermal Cycling	40μm	-64.1	-20.1	44.0
2nd 500°C	10μm	-41	-30.7	10.3
Thermal Cycling	40μm	-19.5	-39.8	-20.3
3rd 500°C	10μm	-30.8	-25.3	5.5
Thermal Cycling	40μm	-39.7	-41.0	-1.3

Fig.6.1. 500°C 3-cycle thermal cycling curves showing film stress as a function of temperature: (a) 10 µm thick, as-deposited PECVD SiO$_x$ film, (b) 40 µm thick, as-deposited PECVD SiOx films.
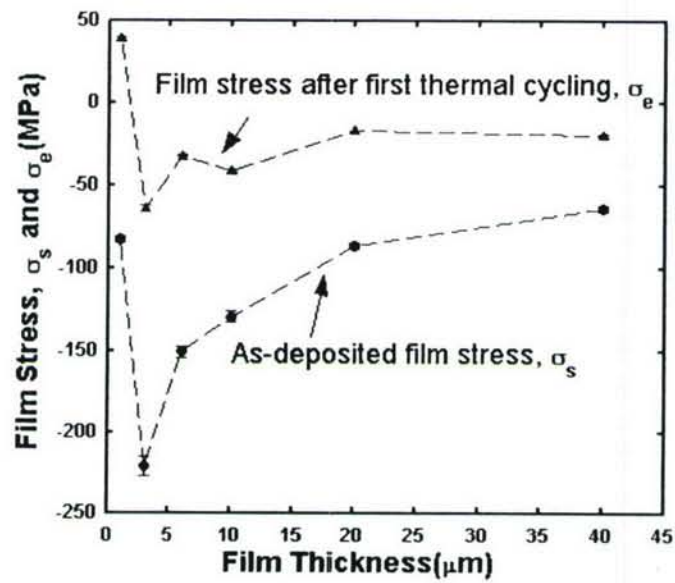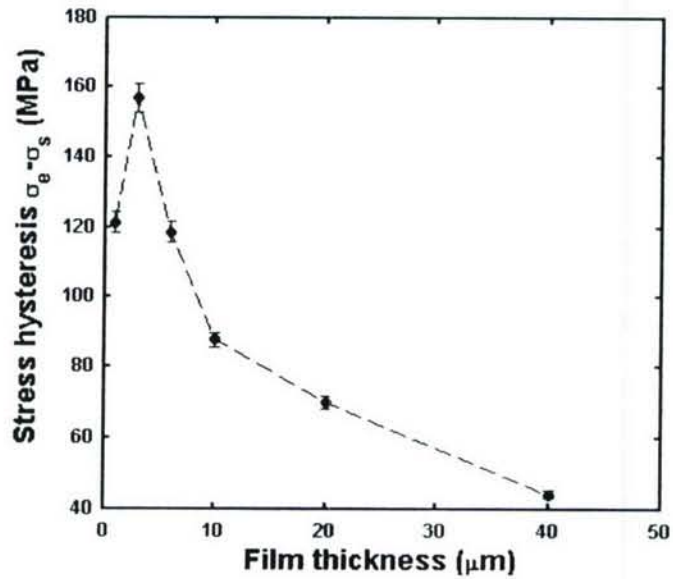
Fig.6.2. (a) As-deposited PECVD SiO$_x$ film stress as a function of film thickness before and after 1st 500°C thermal cycling, (b) The corresponding stress hysteresis (σ_e- σ_s) of as-deposited PECVD SiO$_x$ films in 1st 500°C thermal cycling.
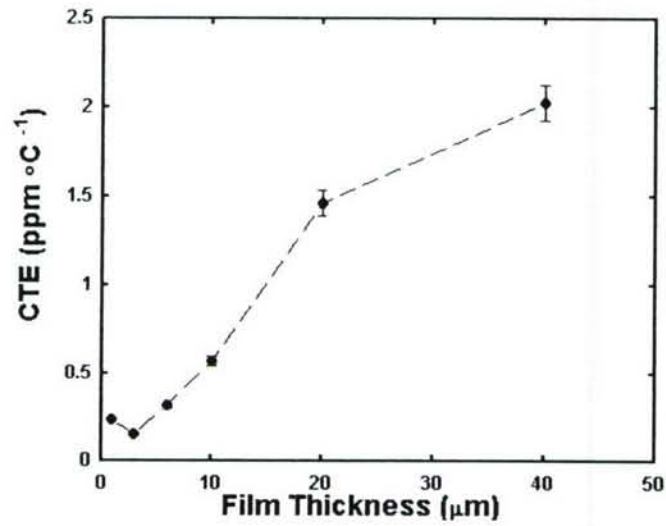
Fig.6.3. PECVD SiO$_x$ film CTE of 1st 500°C thermal cycling as a function of film thickness.
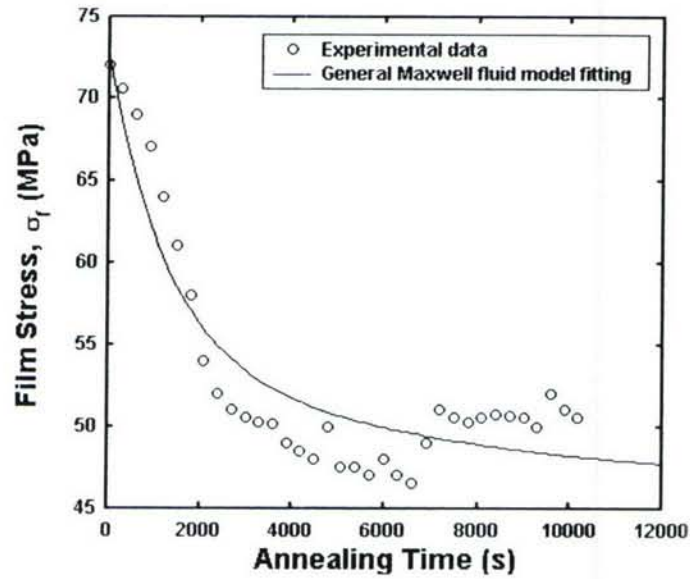
Fig.6.4. The stress relaxation of PECVD SiO$_x$ films annealed at 500°C for three hours.
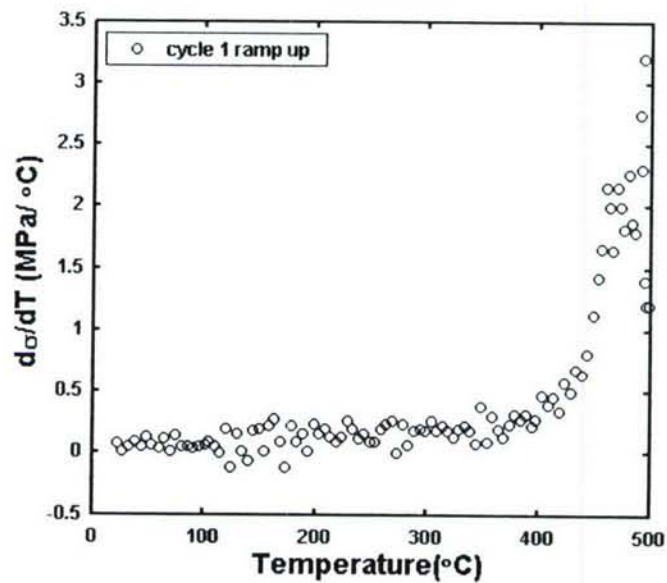
Fig.6.5. Slope of stress-temperature curve as a function of temperature for 10 μm as-deposited PECVD SiO$_x$ film after 1st thermal cycling, ramp up.
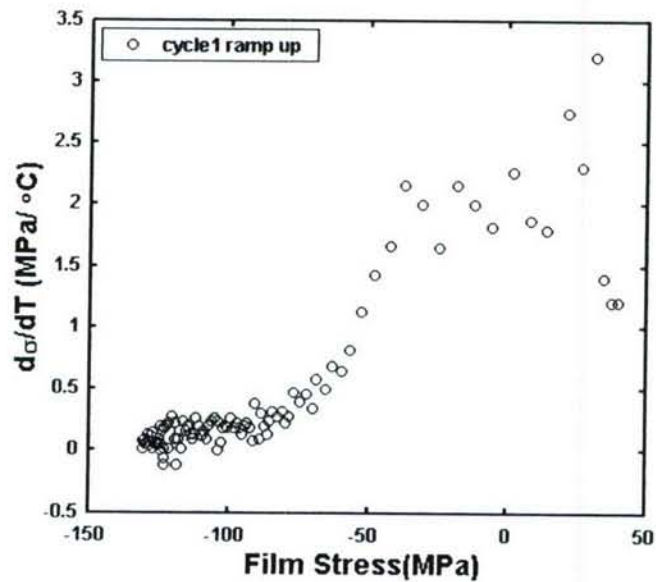
Fig.6.6. Slope of stress-temperature curve as a function of film stress for 10 μm as-deposited PECVD SiO$_x$ film under 1st 500°C thermal cycling, ramp up.
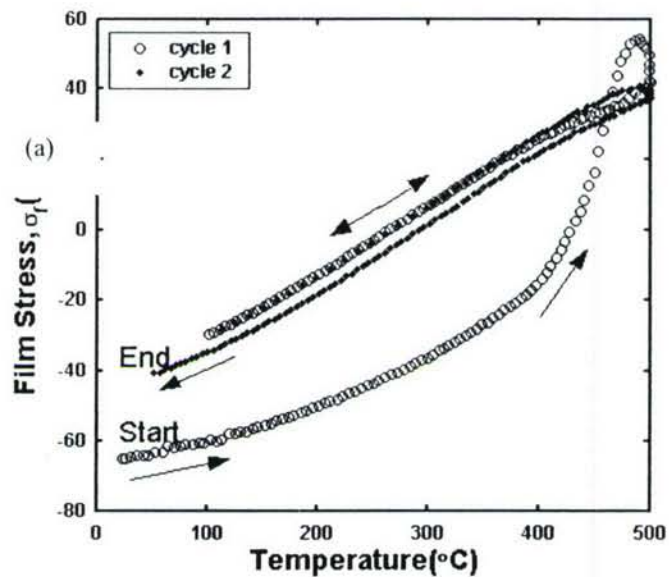
Fig.6.7. Thermal cycling of as-deposited 40 µm PECVD SiO$_x$ film with 30 min annealing at peak temperature, i.e., 500°C.
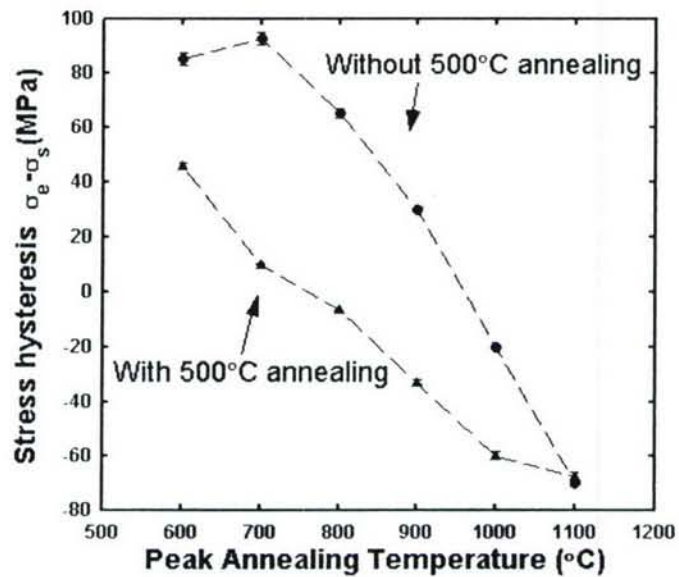
Fig.6.8. Stress hysteresis of 10 µm as-deposited PECVD SiO$_x$ film under different peak annealing temperature varied from 600 to 1100°C.
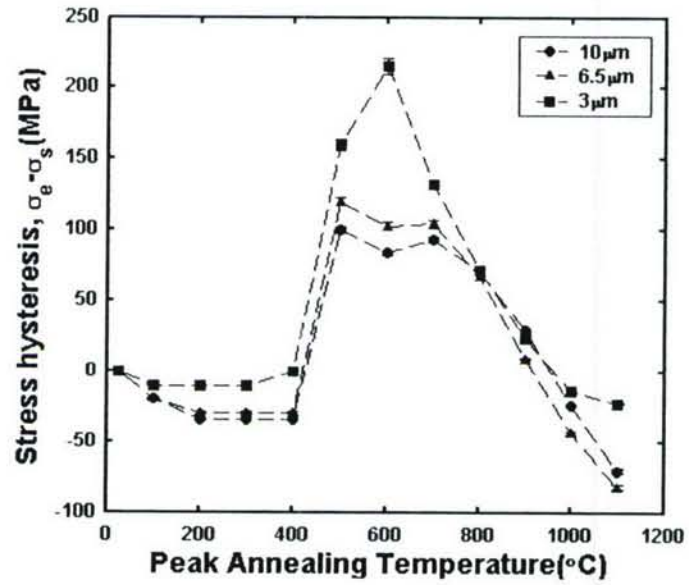
Fig.6.9. Stress hysteresis of as-deposited PECVD SiO$_x$ films with various thicknesses.
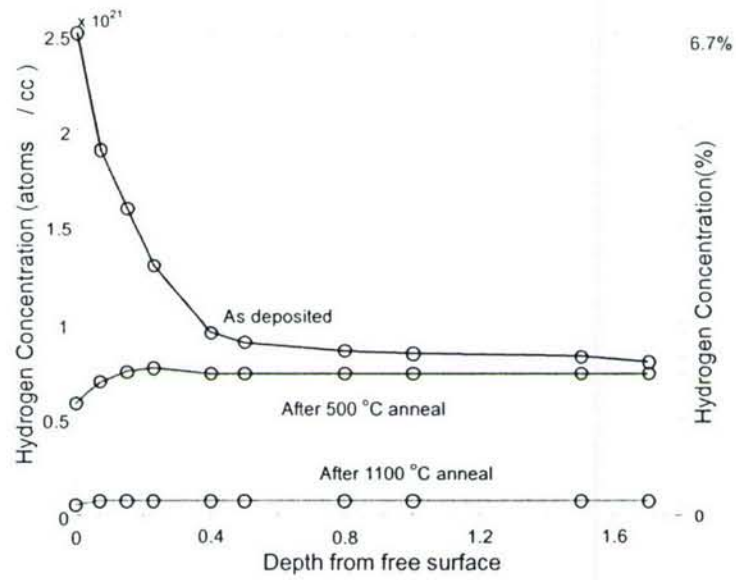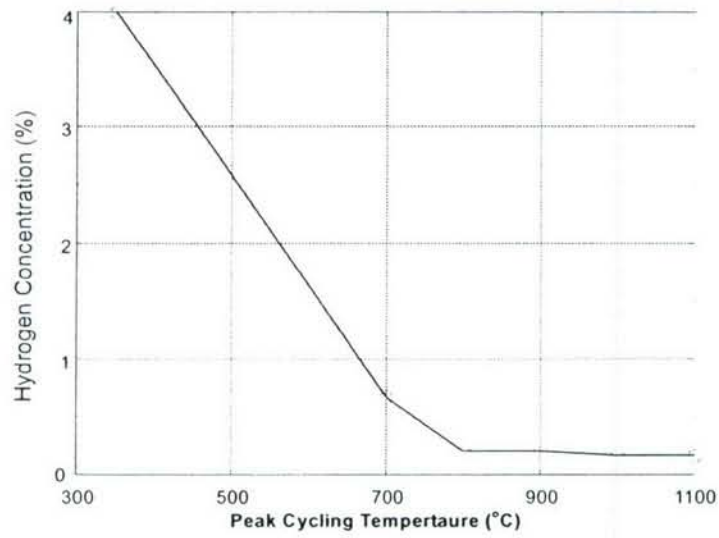
Fig.6.10. SIMS hydrogen concentration analysis result for a 40 μm thick PECVD SiOx film: (a) as-deposited, after 500 and 1100 °C annealing; (b) after annealing at various peak temperatures.
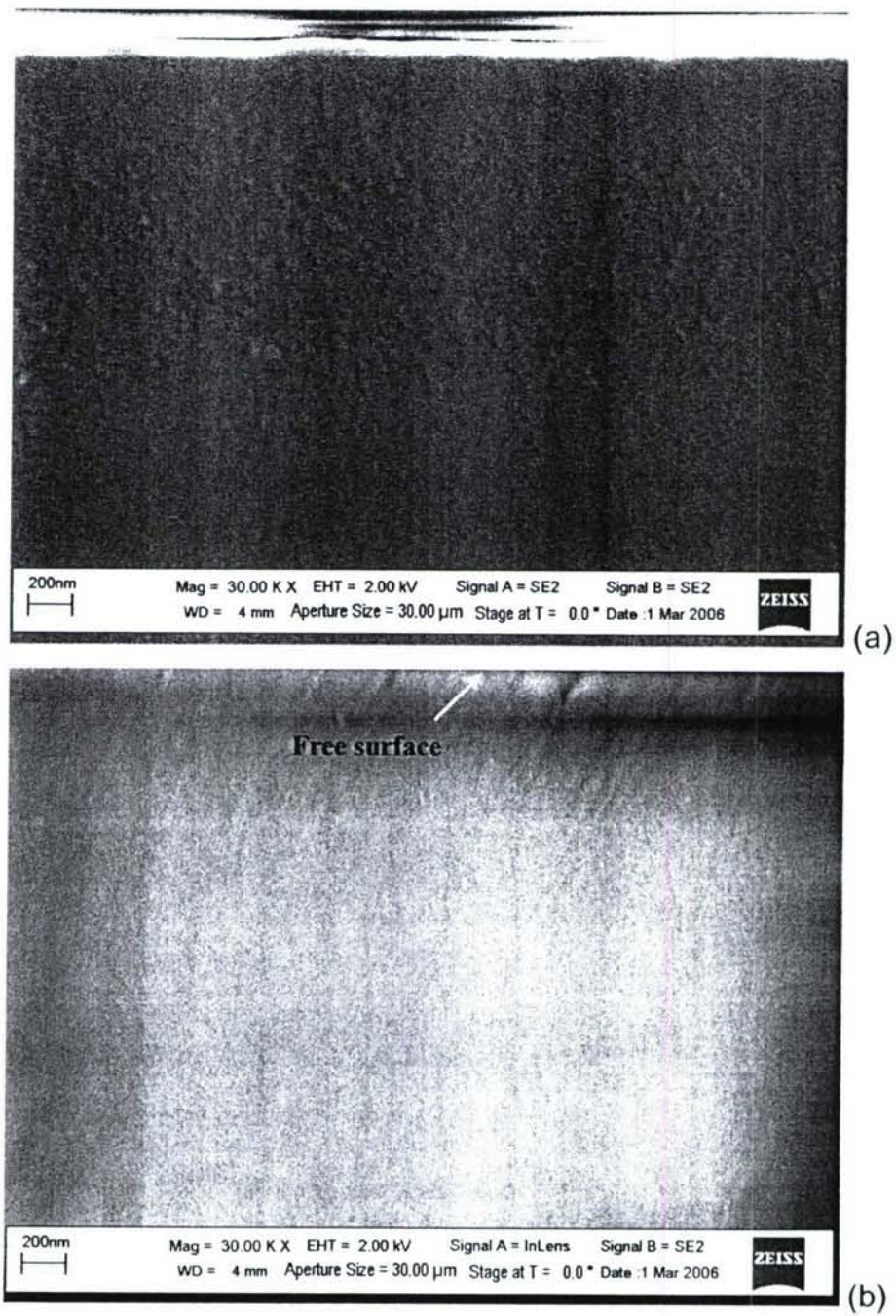
Fig.6.11. FESEM image of the freshly cleaved side-surface of an (a) as-deposited and (b) annealed (800 °C, 10 min in N_2) 5 μm thick PECVD SiO_x film.

7. CONCLUSIONS AND RECOMMENDATIONS FOR FUTURE WORK

7.1. Summary

In this project, PECVD SiO_x is chosen as an example for the *systematic* study of mechanical behaviors and underlying causal mechanisms of the amorphous thin films for MEMS applications. Mechanical responses of the PECVD SiO_x thin films are probed at 1) *different size scales* (from wafer level down to micro/nano-scale, and different length-scale within each realm); 2) *different temperatures* (from room temperature up to 1100 °C); and 3) *with a combination of different experimental techniques* (such as substrate curvature measurements, nanoindentation tests, and a novel "microbridge testing" technique, etc.). These experiments, introduced in Sec.2 and discussed in detail in Sec.3-6, reveal various interesting and distinctive characteristics of the mechanical behaviors of the PECVD SiO_x thin films, and the *microstructural causal mechanisms* for each of them are analyzed in depth.

More specifically, six major topics are covered in these sections:
1)   Microscale residual stress and Young's modulus measurement, by means of "microbridge testing" (Sec.3).
2)   Complete micro/nano scale elastic-plastic properties characterization, by means of "nanoindentation stress-strain curves" (Sec.4).
3)   Time-dependent plasticity (creep) and length-scale effects, by means of "nanoindentation load relaxation" experiments (Sec.5).
4)   Room temperature plastic deformation mechanisms, including physical origin of transformation units, character of plastic flow, and cause of rate-sensitivity and size-effect (Sec.4, 5).

5)   Experimental investigation of structural relaxation phenomena at elevated temperatures, including intrinsic stress evolution, materials properties changes etc., by mean of *in-situ* and *ex-situ* wafer curvature measurements (Sec.6).

6)   Deformation mechanism at elevated temperatures, and its link to the microstructural changes in the material (Sec.6).

7.2. Contributions

Although motivated by the thin film applications in MEMS, this project primarily focuses on contributing to the fundamental scientific understanding of the mechanical behavior of the case-study material: PECVD SiO_x. A broad range of mechanical analysis is covered, including film stress and related material properties changes, elastic properties, plastic properties (both time-independent and time-dependent), deformation mechanisms (both at room temperature and elevated temperatures). To summarize, major contributions of this project entail the following three aspects:

1)   **The outcome of this project will provide a comprehensive characterization** of the mechanical responses of the PECVD SiO_x thin films under different thermal conditions, stress levels, size scales, and in both elastic and plastic regions. In addition, materials analysis techniques such as SEM, AFM, FTIR, XRD, and SIMS were employed to strengthen the discussions on the structure-properties relationship and the causal mechanisms of the mechanical responses of the PECVD SiO_x.

2)   **Both new experimental methodologies and theoretical models for data analysis are resulted,** such as the "microbridge testing method". "Conventional" experimental methods, such as the nanoindentation, were re-invented to measure "non-conventional" properties like the stress-strain curves

and the stress-exponents. The wafer-curvature measurements were exploited theoretically to yield more information about materials properties changes, such as density and viscosity. The experimental methods developed in this research can be also readily applied to a wide variety of thin film materials for various different applications.

3)   The physical causal mechanisms for the experimental results are elucidated, which is a significant contribution to the scientific understanding of this type of amorphous thin film materials. We have developed new theories (such as the "seams and voids" in Sec.6), or applied conventional theories (such as Shear Transformation Zone (STZ) theory in Sec.4, 5) to explain the distinctive experimental results. These theoretical interpretations will also provide valuable insights to the understanding of similar responses of other CVD materials (such as SiN_x and fluorosilicateglass) commonly used in the Microelectronics and MEMS industries, as well as physical vapor deposited (PVD) materials (such as AlO_x), spin-on glass materials and low-k silsesquioxane-based materials.

7.3. Recommendations for Future Work

Amorphous thin film materials have been gaining more importance both in applications and in experimental and theoretical investigations. The experiments and theories in this project have established a preliminary framework under which future researchers can continue to systematically study other thin film materials prepared by similar methods and/or have similar mechanical responses. To conclude the project, I'd like to recommend a few specific topics that promise to be particularly intriguing for the related future research:

1)   Broader applications of the microbridge testing method. In this project, the microbridge testing method was developed to mainly measure

149

micro/local scale residual stress and Young's modulus. Current nanoindentation system setup is limited to a maximum load of 10 mN and a vertical movement range of 5 μm. Due to such limits, in our experiments, we have so far found no evidence of *fracture* or *viscoelasticity* effects of the PECVD SiO_x microbridge samples. With the addition of a multi-range loading system to the nanoindenter, the microbridge may be used to measure the bending strength of the thin films, in which case it simply represents a three-point bending system. The larger stress might also render the viscoelasticity effects to be more significant. Another fascinating option is to add a dynamic loading system (NanoDMA[TM] from Hysitron Inc.) to the nanoindenter. The viscoelasticity of the material may be determined by the phase changes of the measured load/displacement vs. time curves.

2)   Fracture mechanism in the amorphous thin films. First, fracture toughness may be independently measured by employing the sharp Cube Corner tip and a multi-range loading system (Multi-range Nanoprobe[TM], from Hysitron Inc.), which has the capability of loading up to the Newtons. As the materials fracture, the radial fracture length can be measured by the SEM or AFM techniques. It is then possible to evaluate the fracture process from a theoretical modeling angle. For high temperature fracture mechanism, it is important to have the *in-situ* monitoring capability for the cracks development. This implies the integration of a heating system with temperature-resistant optics of some sort. Laser-based moiré interferometry might be a potential candidate, as it can be isolated from the heating source. As a start, the fracture mechanics developed over the years may be applied to interpret the experimental data. Quite possibly, the conventional theories need to be modified to fully explain the observed phenomena.

3) **Direct determination of the microstructure of amorphous thin films.** As mentioned a few times in the previous sections, direct determination of the amorphous microstructure is a challenging task. Nevertheless, the theoretical discussions on the structure-properties relationship would be strengthened with more information about the microstructure evolutions. For this purpose, a technique named Energy Filtered Transmission Electron Microscopy (EFTEM) appears to be most promising. Recently, it was reported that silicon nanoclusters embedded in SiO_2 was produced by thermal annealing of PECVD SiO_x films, and EFTEM was successfully applied to investigate the structural properties of this system.

4) **Development of a fully quantitative deformation mechanism in the amorphous thin films.** Due to the difficulty in directly determining its microstructure and the complex interplay among the deformation mechanisms, modeling the amorphous deformation mechanism at the atomic level is still at its infancy. We end this project by calling for more experimental and theoretical studies into the mechanical behaviors of a wide range of amorphous thin film materials. We expect that these studies may demonstrate many similarities of these materials, and thus a deeper understanding of the deformation mechanisms may be derived from generalizations. It is also likely that in certain cases, they may differ from each other in various ways, and yield quite material or microstructure-specific results. In these cases, the specific differences may be analyzed, and also give us valuable insights and better understanding of the underling causal mechanisms. Consequently, novel engineering approaches for device fabrication and process integration of MEMS/microelectronics may be inspired by the newly gained scientific insights from these new studies.

References

Argon AS (1979), "Plastic deformation in metallic glasses", *Acta Metallurgica* **27**, 47.

Argon AS and Shi LT (1983), "Development of viscoplastic deformation in metallic glasses", *Acta Metallurgica* **31**, 499.

Ayon AA, Zhang X, Turner K, Choi D, Miller B, Nagle SF, and Spearing SM (2003), "Characterization of silicon wafer bonding for power MEMS applications," *Sensors and Actuators A: Physical* **103**, 1.

Baker SP and Nix WD (1994), "Mechanical properties of compositionally modulated Au-Ni thin films- Nanoindentation and microcantilever deflection experiments", *Journal of Materials Research* **9**, 3131.

Baney RH, Itoh M, Sakakibara A, and Suzuki T (1995), "Silsesquioxanes", *Chemical Review* **95**, 1409.

Bei H, Lu ZP, and George EP (2004), "Theoretical strength and onset of plasticity in bulk metallic glasses investigated by nanoindentation with a spherical indenter", *Physical Review Letters* **93**, 125504.

Bhattacharya AK and Nix WD (1988), "Analysis of Elastic and Plastic Deformation Associated With Indentation Testing of Thin Films on Substrates", *International Journal of Solids and Structures* **24**, 1287.

Blaauw C (1983), "Stress in chemical-vapor-deposited SiO_2 and plasma-SiN_x films on GaAs and Si", September, *Journal of Applied Physics* **54**, 5064.

Bower AF, Fleck NA, Needleman A, and Ogbonna N (1993), "Indentation of a power law creeping solid", *Proceedings of the Royal Society of London A* **441**, 97.

Brotzen FR (1994), "Mechanical testing of thin films", *International Materials Reviews* **39**, 24-45.

Cao Z, Zhang TY, and Zhang X (2005), "Microbridge testing of plasma enhanced chemical vapor deposited silicon oxide films on silicon wafers", *Journal of Applied Physics* **97**, 104909 and the references therein.

Cao Z and Zhang X (2004), "Density change and viscous flow during structural relaxation of plasma-enhanced chemical vapor deposited silicon oxide films", *Journal of Applied Physics* **96**, 4273, and the references therein.

Chang SC, and Hicks DB (1990), "The formation of microbridges on (100)-oriented silicon", *Journal of Micromechanics and Microengineering* **1**, 25.

Chen KS, Zhang X, and Lin SY (2003), "Intrinsic stress generation and relaxation of plasma-enhanced chemical vapor deposited oxide during deposition and subsequent thermal cycling," *Thin Solid Films* **434**, 190.

Chen KS and Ou KS (2002), "Modification of curvature based thin-film residual stress measurement for MEMS", *Journal of Micromechanics and Microengineering* **12**, 917.

Comedi D, Zalloum O H Y, Irving E A, Wojcik J, Roschuk T, Flynn M J, and Mascher P (2006), "X-ray-diffraction study of crystalline Si nanocluster formation in annealed silicon-rich silicon oxides", *Journal of Applied Physics* **99**, 023518.

Cook RF and Liniger EG (1999), "Stress-corrosion cracking of low-dielectric-constant spin-on-glass thin films", *Journal of the Electrochemical Society* **146**, 4439.

Courtney TH (2000), *Mechanical Behavior of Materials*, 2nd ed. (McGraw Hill, Boston).

De Boer MP and Gerberich WW (1996), "Microwedge indentation of thin film fine line- II. Experiment", *Acta Materialia* **44**, 3177.

Del Prado A, San Andrés E, Mártil I, González-Díaz G, Bravo D, López FJ, Fernández M, and Martínez FL (2003), "Microstructural modifications induced by rapid thermal annealing in plasma deposited SiO_xN_yHz films" *Journal of Applied Physics* **94**, 1019.

Domínguez C, Rodríguez J A, Riera M, Llobera A, and Díaz B (2003), "Effect of hydrogen-related impurities on the thermal behavior of mechanical stress in

silicon oxides suitable for integrated optics", *Journal of Applied Physics* **93**, 5125.

Drucker D C (1952) "A more fundamental approach to plastic stress-strain relations", *Proceedings of 1st US National Congress of Applied Mechanics (Chicago, 1951), p.487* (A.S.M.E., New York).

Eastman JA and Fitzsimmons MR (1995), "On the two-state microstructure of nanocrystalline chromium", *Journal of Applied Physics* **77**, 522.

Elmustafa AA and Stone DS (2003), "Nanoindentation and the indentation size effect: Kinetics of deformation and strain gradient plasticity", *Journal of Mechanics and Physics of Solids* **51**, 357.

Epstein AH and Senturia SD, "Macro power from micro machinery", *Science* **276**, 1211 (1997).

Espinosa HD, Prorok BC, and Fischer M (2003), "A methodology for determining mechanical properties of freestanding thin films and MEMS materials", *Journal of Mechanics and Physics of Solids* **51**, 47.

Falk ML, Langer JS, and Pechenik L (2004), "Thermal effects in the shear-transformation-zone theory of amorphous plasticity: Comparisons to metallic glass data", *Physical Review E* **70**, 011507.

Falk ML and Langer JS (1998), "Dynamics of viscoplastic deformation in amorphous solids", *Physical Review E* **57**, 7192.

Fang W, Lee CH, and Hu HH, "On the buckling behavior of micromachined beams", *Journal of Micromechanics and Microengineering* **9**, 236 (1999).

Fang W (1998), "Design of bulk micromachined suspensions", *Journal of Micromechanics and Microengineering* **8**, 263.

Fang W and Wickert JA (1996), "Determining mean and gradient residual stresses in thin films using micromachined cantilevers", *Journal of Micromechanics and Microengineering* **6**, 301.

Fleck NA and Hutchison JW (2001), "A reformulation of strain gradient plasticity", *Journal of Mechanics and Physics of Solids* **49**, 2245.

Frechette LG, Jacobson SA, Breuer KS, Ehrich FF, Ghodssi R, Khanna R, Wong CW, Zhang X, Schmidt MA, and Epstein AH (2005), "High-speed microfabricated silicon turbomachinery and fluid film bearings," *IEEE/ASME Journal of Microelectromechanical Systems* **14**, 141.

Frechette LG, Jacobson SA, Breuer KS, Ehrich FF, Ghodssi R, Khanna R, Wong CW, Zhang X, Schmidt MA, and Epstein AH (2000a), "Demonstration of a microfabricated high-speed turbine supported on gas bearings," *Technical Digest of IEEE Solid-State Sensor and Actuator Workshop (Hilton Head '00)*, Hilton Head Island, SC, USA, June 4-9, 2000, pp. 43-47.

Frechette LG (2000b), Development of a silicon microfabricated motor driven compressor, Ph.D. Thesis, Department of Aeronautics and Astronautics, MIT.

Freund LB and Suresh S (2004), *Thin Film Materials: Stress, Defect Formation and Surface Evolution.* (Cambridge University Press, New York).

Gad-el-Hak M (2002), *The MEMS Handbook.* (CRC Press, Boca Raton)

Gardner RA, Peterson PJ, and Kennedy TN (1977), "Stability of RF-sputtered aluminum oxide", *Journal of Vacuum Science and Technology* **14**, 1139.

Gaskell G H and Wallis D J (1996),"Medium range order in silica, the canonical network glass", *Physical Review Letters* **76**, 66.

Gourbilleau F, Portier X, Ternon C, Voivenel P, Madelon R, and Rizk R (2001), "Si-rich/SiO_2 nanostructured multilayers by reactive magnetron sputtering", *Applied Physics Letters* **78**, 3058.

Habermehl S (1998), "Stress relaxation in Si-rich silicon nitride thin films", *Journal of Applied Physics* **83**, 4672.

Hernandez CM, Murray TW, and Krishnaswamy S (2002), "Photoacoustic characterization of the mechanical properties of thin films", *Applied Physics Letters* **80**, 691-693.

Hill R (1992), "Similarity analysis of creep indentation tests", *Proceedings of the Royal Society of London A* **436**, 617.

155

Hollahan JR, Electrochem J (1979), "Deposition of plasma silicon oxide thin films in a production planar reactor" *Journal of the Electrochemical Society* **126**, 930.

Hommel M and Kraft O (2001), "Deformation behavior of thin copper films on deformable substrates", *Acta Materialia* **49**, 3935.

Huang H and Spaepen F (2000), "Tensile testing of free-standing Cu, Ag and Al thin films and Ag/Cu multilayers", *Acta Materialia* **48**, 3261.

Iacona F, Bongiorno C, Spinella C, Boninelli S, and Priolo F (2004), "Formation and evolution of luminescent Si nanoclusters produced by thermal annealing of SiOx films", *Journal of Applied Physics* **95**, 3723.

Iacona F, Franzò G, and Spinella C (2000), "Correlation between luminescence and structural properties of Si nanocrystals", *Journal of Applied Physics* **87**, 1295.

Inokuma T, Wakayama Y, Muramoto T, Aoki R, Kurata Y, and Hasegawa S (1998), "Optical properties of Si clusters and Si nanocrystallites in high-temperature annealed SiOx films" *Journal of Applied Physics* **83**, 2228.

Johnson K L (1970) "The correlation of indentation experiments", *Journal of Mechanics and Physics of Solids* **18** 115

Kim JJ, Choi Y, Suresh S, and Argon AS (2002), "Nanocrystallization during nanoindentation of a bulk amorphous metal alloy at room temperature", *Science* **295**, 654.

Kucheyev SO, Bradby JE, and. Williams JS (2000), "Nanoindentation of epitaxial GaN films", *Applied Physics Letters* **77**, 3373-3375.

Langer JS (2001), "Microstructural shear localization in plastic deformation of amorphous solids", *Physical Review E* **64**, 011504.

Li H and Ngan AHW (2004), "Size effects of nanoindentation creep", *Journal of Materials Research* **19**, 513.

Lu L, Sui ML, and Lu L (2000), "Superplastic extensibility of nanocrystalline copper at room temperature", *Science* **287**, 1463.

Lubguban J Jr., Kurata Y, Inokuma T, and Hasegawa S (2000), "Thermal stability and breakdown strength of carbon-doped SiO_2:F films prepared by plasma-enhanced chemical vapor deposition method", *Journal of Applied Physics* **87**, 3715.

Lubliner J (1990), *Plastic Theory* (Macmillan Publishing Company, New York).

Lucas BN and Oliver WC (1999), "Indentation power-law creep of high-purity indium", *Metallurgical and Materials Transactions A* **30A**, 601.

Madou M (2002), *Fundamentals of Microfabrication: The Science of Miniaturization*, 2nd ed. (CRC Press, Boca Raton).

Martínez E, Romero J, Lousa A and Esteve J (2003) "Nanoindentation stress-strain curves as a method for thin film complete mechanical characterization: application to CrN/Cr multiplayer coatings", *Applied Physics A* **77** 419

Matsuura T, Taguchi M, Kawata K, and Tsutsumi T (1997), "Deformation control of microbridges for flow sensors", *Sensors and Actuators A* **60**, 197.

Mearini GT, and Hoffman RW (1993), "Tensile properties of aluminum/alumina multi-layered thin films", *Journal of Electronic Materials* **22**, 623.

Mehra A, Zhang X, Ayon AA, Waitz IA, Schmidt MA, and Spadaccini CM (2000), "A six-wafer combustion system for a silicon micro gas turbin engine", *Journal of Microelectromechanical Systems* **9**, 516.

Merlos A, Acero MC, Bao MH, Bausells J, and Esteve J (1992), "A study of undercutting characteristics in TMAH-IPA system", *Journal of Micromechanics and Microengineering* **2**, 181.

Miki N, Teo CJ, Ho L, and Zhang X (2003), "Enhancement of rotordynamic performance of high-speed micro-rotors for power MEMS applications by precision deep reactive ion etching," *Sensors and Actuators A: Physical* **104**, 263.

Min KS, K. V. Shcheglov, C. M. Yang, H. A. Atwater, M. L. Brongersma, and A. Polman (1996), "Defect-related versus excitonic visible light emission from ion beam synthesized Si nanocrystals in SiO_2", *Applied Physics Letters* **69**, 2033.

Moldovan C, Kim BH, Raible S, and Moagar V (2000), "Manufacturing of surface micromachined structures for chemical sensors", *Thin Solid Films* **383**, 321.

Muller KH (1985), "Dependence of thin-film microstructures on deposition rate by means of a computer simulation", *Journal of Applied Physics* **58**, 2573.

Nagle SF (2000), "Analysis, design and fabrication of an electric induction micromotor for a micro gas turbine generator", Ph.D. Thesis, Department of Electrical Engineering and Computer Science, MIT.

Najafi K and Suzuki K (1989), "Measurement of fracture stress, Young's modulus, and intrinsic stress of heavily boron-doped silicon microstructures", *Thin Solid Films* **181**,251.

Nix WD and Gao H (1998), "Indentation size effects in crystalline materials: A law for strain gradient plasticity", *Journal of Mechanics and Physics of Solids* **46**, 411.

Nguyen SV (1999), "High density plasma chemical vapor deposition of silicon based dielectric films for integrated circutis", *IBM Journal of Research and Development* **43**, 109.

Ohring M (1992), *The Material Science of Thin Films* (Academic Press, New York).

Oliver WC and Pharr GM (2004), "Measurement of hardness and elastic modulus by instrumented indentation: Advances in understanding and refinements to methodology", *Journal of Materials Research* **19**, 3 and the references therein.

Oliver WC and Pharr GM (1992), "An improved technique for determining hardness and elastic modulus using load and displacement sensing indentation experiments", *Journal of Materials Research* **7**, 1564 and the references therein.

Peirs J, Reynaerts D and Verplaetsen F (2004), "A microturbine for electric power generation", *Sensors and Actuators A: Physical* **113**, 86.

Poisl WH, Oliver WC, and Fabes BD (1995), "The relationship between indentation and uniaxial creep in amorphous selenium", *Journal of Materials Research* **10**, 2024.

Pharr G M (1998) "Measurement of mechanical properties by ultra-low load indentation", *Materials Science and Engineering A* **523** 151.

Salamon N and Masters C (1995), "Bifurcation in isotropic thin-film/substrate plates", *International Journal of Solids and Structures* **32**, 473.

Saksl K, Franz H, Jóvári P, Klementiev K, Welter E, Ehnes A, Saida J, Inoue A, Jiang JZ (2003), "Evidence of icosahedral short-range order in $Zr_{70}Cu_{30}$ and $Zr_{70}Cu_{29}Pd_1$ metallic glasses", *Applied Physics Letters* **83**,3924.

San Andrés E, del Prado A, Martínez FL, Mártil I, Bravo D and López FJ (2000), "Rapid thermal annealing effects on the structural properties and density of defects in SiO_2 and SiN_x:H films deposited by electron cyclotron resonance", *Journal of Applied Physics* **87**, 1187.

Schwaiger R and Kraft O (2003), "Size effects in the fatigue behavior of thin Ag films", *Acta Materialia* **51**, 195.

Schweitz JA (1992), "Mechanical Characterization of Thin Films by Micromechanical Techniques," *MRS Bulletin* **17**, 34.

Schiøtz J, Di Tolla FD, and Jacobsen KW (1998), "Softening of nanocrystalline metals at very small grain sizes", *Nature* **391**, 561.

Schuh CA and Nieh TG (2003), "A nanoindentation study of serrated flow in bulk metallic glasses", *Acta Materialia* **51**, 87.

Schuh CA and Nieh TG (2004), "A survey of instrumented indentation studies on metallic glasses", *Journal of Material Research* **19**, 46, and the references therein.

Schwaiger R, Moser B, Dao M, Chollacoop N, and Suresh S (2003), "Some critical experiments on the strain-rate sensitivity of nanocrystalline nickel", *Acta Materialia* **51**, 5159.

Sharpe WN Jr., Yuan B, and Edwards RL (1997), "A new technique for measuring the mechanical properties of thin films", *Journal of Microelectromechanical Systems* **6**, 193.

Shi Y and Falk ML (2005), "Structural transformation and localization during simulated nanoindentation of a nanocrystalline metal film", *Applied Physics Letters* **86**, 011914.

Shull AL and Spaepen F (1996), "Measurements of stress during vapor deposition of copper and silver thin films and multilayers", *Journal of Applied Physics* **80**, 6243-6256.

Spadaccini CM, Mehra A, Lee J, Zhang X, Lukachko S, and Waitz IA (2003), "High power density silicon combustion systems for micro gas turbine engines," *ASME Journal of Engineering for Gas Turbines and Power* **125**, 709.

Spadaccini CM, Zhang X, Cadou CP, Miki N, and Waitz IA (2002), "Development of a catalytic silicon micro-combustor for hydrocarbon fueled power MEMS," *Proceeding of the 15th IEEE International Conference on Micro Electro Mechanical Systems (MEMS '02)*, Las Vegas, NV, USA, January 20-24, 2002, pp. 228-231.

Spaepen F (1977), "A microscopic mechanism for steady state in homogeneous flow in metallic glasses", *Acta Metallurgica* **25**, 407.

Stadtmüeller M, Electrochem J (1992), "Mechanical stress of CVD-dielectrics", *Journal of the Electrochemical Society* **139**, 3669.

Stoney GG (1909), "The tension of thin metallic films deposited by electrolysis", *Proceedings of the Royal Society of London A* **82** 172.

Storåkers B and Larsson PL (1994), "On Brinell and Boussinesq indentation creeping solids", *Journal of Mechanics and Physics of Solids* **42**, 307.

Su YJ, Qian CF, Zhao MH, and Zhang TY (2000), "Microbridge testing of silicon oxide/silicon nitride bilayer films deposited on silicon wafers", *Acta Materialia* **48**, 4901.

Tabor D (1951), *The Hardness of Metals*, (Clarendon Press, Oxford).

Taylor JA (1991), "The mechanical properties and microstructure of plasma enhanced chemical vapor deposited silicon nitride thin films", *Journal of Vacuum Science and Technology A.* **9**, 2464.

Thurn J, Cook RF, Kamarajugadda M, Bozeman S P, and Stearns L C (2004), "Stress hysteresis and mechanical properties of plasma-enhanced chemical vapor deposited dielectric films", *Journal of Applied Physics* **95**, 967.

Thurn J and Cook RF (2002), "Stress hysteresis during thermal cycling of plasma-enhanced chemical vapor deposited silicon oxide films", *Journal of Applied Physics* **91,** 1988, and the references therein.

Timoshenko S and Gere J (1961), *Theory of Elastic Stability*, 2nd ed (McGraw-Hill, New York).

Timoshenko S and Woinowsky-Krieger S (1959), *Theory of Plates and Shells*, 2nd ed. (McGraw-Hill, New York).

Tsui YG and Clyne TW (1997), "An analytical model for predicting residual stresses in progressively deposited coatings Part 1: Planer geometry", *Thin Solid Films*, **386**, 23.

Turnbull D and Cohen M (1970), "On the free-volume model of the liquid-glass transition", *Journal of Chemical Physics* **52**, 3038.

Tymiak NI, Kramer DE, Bahr DF, Wyrobek TJ, and Gerberich WW (2001), "Plastic strain and strain gradients at very small indentation depths", *Acta Materialia* **49,** 1021.

Vinci RP and Vlassak JJ (1996), "Mechanical behavior of thin films", *Annual Review of Materials Science* **26**, 431.

Vlassak JJ, and Nix WD (1992), "A new voltage test technique for the determination of Young's modulus and Poisson ratio of thin films", *Journal of Materials Research* **7**, 3242.

Volkert CA (1993), "Density change and viscous flow during structural relaxation of amorphous silicon", *Journal of Applied Physics* **74**, 7107, and the references therein.

Weihs TP, Hong S, Bravman JC, and Nix WD (1988), "Mechanical deflection of cantilever microbeams: A new technique for testing the mechanical properties of thin films", *Journal of Materials Research* **3**, 931.

Weinberg MS (1999), "Working equations for piezoelectric actuators and sensors", *Journal of Microelectromechanical Systems* **8**, 529.

Werwa E, Seraphin AA, Chiu LA, Zhou C, and Kolenbrander KD (1994), "Synthesis and processing of silicon nanocrystallites using a pulsed laser ablation supersonic expansion method" *Applied Physics Letters* **64**, 1821.

Windischmann H (1991), "Intrinsic stress and mechanical properties of hydrogenated silicon carbide produced by plasma enhanced chemical vapor deposition", *Journal of Vacuum Science and Technology* A **9** 2459.

Wong CW, Zhang X, Jacobson SA, and Epstein AH (2004), "A self-acting gas thrust bearing for high-speed microrotors," *IEEE/ASME Journal of Microelectromechanical Systems* **13**, 158.

Xiang Y, Chen X, and Vlassak JJ (2005), "The plane-strain bulge test for thin films", *Journal of Material Research* **20**, 2360.

Xu WH and Zhang TY (2003), "Mechanical characterization of trilayer thin films by the microbridge testing method", *Applied Physics Letters* **83**, 1731.

Xu WH, Lu DX, and Zhang TY (2001), "Determination of residual stresses in Pb (Zr 0.53 Ti 0.47) O_3 thin films with Raman spectroscopy", *Applied Physics Letters* **79**, 4112.

Zhang TY and Xu WH (2002), "Surface effects on nanoindentation", *Journal of Material Research*, **17**, 1715.

Zhang TY, Su YJ, Qian CF, Zhao MH, and Chen LQ (2000), "Microbridge testing of silicon nitride films deposited on silicon wafers", *Acta Materialia* **48**, 2843.

Zhang TY, Chen LQ and Fu R (1999), "Measurements of residual stresses in thin films deposited on silicon wafers by indentation facture", *Acta Materialia* **47**, 3869.

Zhang X, Mehra A, Ayon AA, and Waitz IA (2003a), "Igniters and temperature sensors for a micro-scale combustion system," *Sensors and Actuators A: Physical* **103**, 253.

Zhang X, Chen KS, and Spearing SM (2003b), "Thermal-Mechanical Behavior of Thick PECVD Oxide Films for Power MEMS Applications," *Sensors and Actuators A: Physical,* **103**, 263.

Zhang X, Chen KS, and Spearing SM (2002), "Residual stress and fracture of thick dielectric films for power MEMS applications," *Proceeding of the 15th IEEE International Conference on Micro Electro Mechanical Systems (MEMS '02),* Las Vegas, NV, USA, January 20-24, 2002, pp. 164-167.

Zhang X, Chen KS, Ghodssi R, Ayon AA, and Spearing SM (2001), "Residual stress and fracture in thick tetraethylorthosilicate (TEOS) and silane-based PECVD oxide films," *Sensors and Actuators A: Physical* **91**, 373.

Zheng DW, Xu YH, Tsai YP, Tu KN, Patterson P, Zhao B, Liu QZ (2000), and Brongo M, "Mechanical property measurement of thin polymeric-low dielectric-constant films using bulge testing method", *Applied Physics Letters* **76**, 2008-2010.

Zhou QY, Argon AS, and Cohen RE (2001), "Enhanced Case-II diffusion of diluents into glassy polymers undergoing plastic flow", *Polymer* **42**, 613.

Zhu JG, White CW, Budai JD, Withrow SP, and Chen Y (1995), "Growth of Ge, Si, and SiGe nanocrystals in SiO_2 matrices", *Journal of Applied Physics* **78**, 4386.

Ziebart V, Paul O, Munch U, Schwizer J, and Baltes H (1998), "Mechanical properties of thin films from the load deflection of long clamped plates", *Journal of Microelectromechanical Systems* **7**, 320.